Magnetorquer Design and Attitude Control for SHAPE

MSc Thesis

A.I. van Hengel

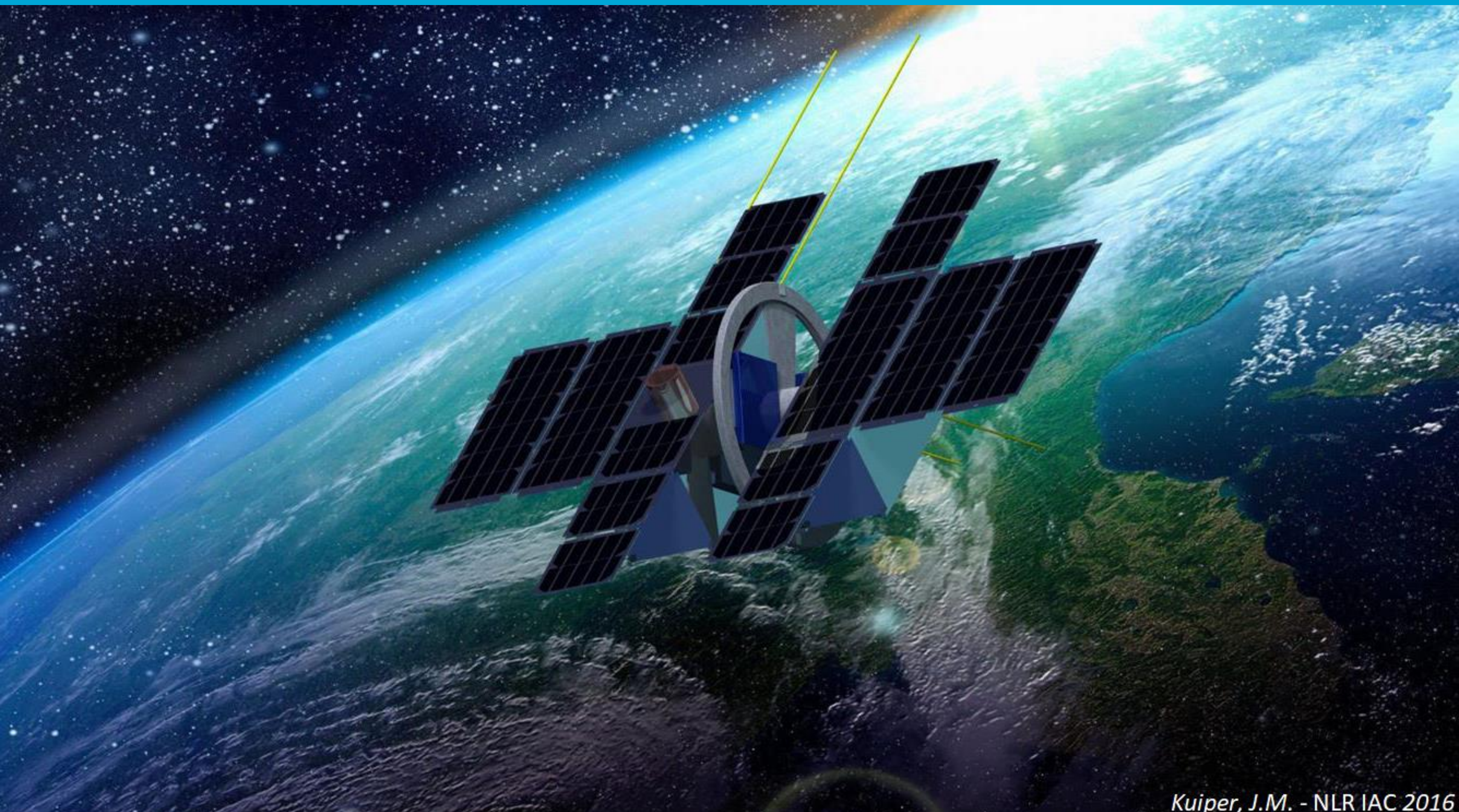
Kuiper, J.M. - NLR IAC 2016

TU Delft

Magnetorquer Design and Attitude Control for SHAPE

MSc Thesis

by

A.I. van Hengel

to obtain the degree of Master of Science
at the Delft University of Technology,
to be defended publicly on November 22, 2018 at 12:00.

Student number:	4015207	
Project duration:	February 1, 2017 – November 22, 2018	
Thesis committee:	Dr. A. Cervone,	TU Delft, chair
	Dr. ir. J.M. Kuiper,	TU Delft, supervisor
	Dr. ir. B.C. Root,	TU Delft, department Astrodynamics and Space Missions
	Dr. ir. B. Monna,	Hyperion, external

Preface

As child I was always fascinated by space, constantly looking up to the stars. At school, it was clear that I would end up doing something with science and technology. First the science behind medicine looked very interesting, but after visiting Aerospace Engineering my decision was made. I would become an engineer! Fascinated by the space part of the study, naturally I choose the Space Flight master. During the master I decided to explore all facets of space systems engineering, before settling upon spacecraft attitude control as my topic for my master thesis.
During the thesis work I had a lot of struggles, not because it was not interesting, but because I had to manage everything by myself. Making a global planning did not help, but in the end I found out that by making small work packages and creating short term planning goals, I made myself more productive and was able to come back to a good work flow.

I would like to thank Hans Kuiper for providing the topic on attitude control for his project SHAPE and for supervising me during my work. I would like to thank Bert Monna from Hyperion for his critical view and constructing comments. These two people did not make it easy for me, but in the end I am thankful for their criticism.
Furthermore, I would like to thank my parents for their endless support in many ways, and my friends who encouraged me to keep going, even when it seemed to go nowhere.

A.I. van Hengel
Delft, November 9, 2018

Contents

1

Introduction

For Earth Observation (EO) missions, a stable and well controllable platform is needed. In Very Low Earth Orbits (VLEO) this is more challenging since the disturbances are higher. The Stable and Highly Accurate Pointing Earth-imager (SHAPE) is an Earth observation mission in VLEO with a large momentum wheel to stabilize the spacecraft against the external disturbances (Kuiper and Dolkens, 2016). The wheel stabilizes two of the three axes of the spacecraft. For the other axis, a magnetorquer system is proposed which additionally has to provide the control of the spacecraft.

To design the magnetorquer control system some earlier set requirements have to be met. The most important ones are the pointing accuracy of at least 1°, stability of 5.5 mrad/s or better, and a dipole moment for each magnetorquer of 0.5 Am^2 (Kuiper and Dolkens, 2016; Ju, 2017). To meet these requirements, a magnetorquer will be designed and an attitude control loop will be developed, both optimized for SHAPE.

This thesis will start with a short introduction of SHAPE and the previously set requirements in chapter 2. The objective of this thesis will be presented here as well. In chapters 3 and 4 the magnetorquer will be modeled and designed. Then the orbital details will be discussed in chapter 5, followed by the attitude control loop in chapters 6 and 7. Finally, the conclusions and recommendations are in chapter 8.

2

Research Objective

The Stable and Highly Accurate Pointing Earth-imager (SHAPE) is an Earth observation mission in VLEO with a huge momentum wheel to stabilize the spacecraft against the external disturbances. The spacecraft consist of two 3-unit CubeSat modules (10 x 10 x 30 cm) on both sides of the momentum wheel as shown in figure 2.1. One of these modules contains the payload, a high spatial resolution camera, and the other module will contain all other subsystems, such as the magnetorquers for attitude control, the battery and the on-board computer. The spacecraft will fly at an altitude of 380-230 km during its lifetime of about 200 days and will have a noon-midnight Sun-synchronous orbit (SSO).

To keep the spacecraft orientation within the set limits an active control system is needed next to the momentum wheel, especially for the axis that is not stabilized by the wheel. A magnetorquer control system is proposed as active control system and some requirements were set for this system. A set of key attitude system requirements can be found in table 2.1 and a set of the magnetorquer requirements can be found in table 2.2, these were predefined by Kuiper and Dolkens (2016), and Ju (2017). The most important ones are the pointing accuracy of at least 1°, stability of 5.5 mrad/s or better, and dipole moment for each magnetorquer of at least 0.5 Am^2. With this, a research object is formulated as follows:

To come to a feasible magnetorquer control system for SHAPE, by designing a magnetorquer with a dipole moment of at least 0.5 Am^2 and an attitude control loop that achieves a pointing accuracy of at least 1° ***and attitude stability of 5.5 mrad/s or better.***

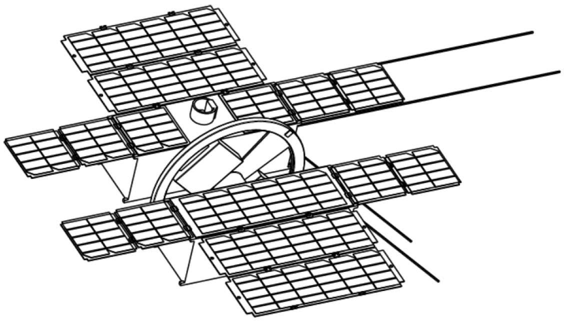

Figure 2.1: The SHAPE concept (Kuiper and Dolkens, 2016)

In this thesis a bottom-up approach will be used to come to a magnetorquer control system. First a magnetorquer will be designed, and then the control loop with only magnetorquer control next to the momentum wheel. The structure of the core of this thesis can be found in figure 2.2.

Table 2.1: Attitude system requirements (Kuiper and Dolkens, 2016; Ju, 2017)

Code	**Requirement**	**Rationale**
S.1	The system shall have a pointing accuracy better than 1.0°	Targeting, small overlapping coverage and technology demonstration
S.2	The system shall have an attitude stability better than 5.5 mrad/s (target), 3.8 mrad/s (desired)	Image quality requirement
S.3	The system shall operate between 380 to 230 km altitude	Minimal lifetime of 6 months and payload resolution
S.4	The system shall be in a noon/midnight SSO	Power requirement and payload requirement of wavelength of 450-650 nm
S.5	The system shall have a peak power of 11 W during non-mission operation modes	Allocated power budget
S.6	The system shall have a peak power of 6 W during mission operation modes	Allocated power budget
S.7	The system shall have no single point of failure	
S.8	The attitude control system shall not have a mass of more than 800 g	Allocated mass budget

Table 2.2: Magnetorquer requirements (Ju, 2017)

Code	**Requirement**	**Rationale**
M.1	The magnetorquers shall be able to provide a nominal dipole moment of at least 0.5 Am^2	Expected maximum torque in nominal mode
M.2	The magnetorquers shall have a resolution better than <TBD> mAm^2 on all axes	TBD to be resolved after in-depth nominal mode control analysis
M.3	The magnetorquers shall have a residual magnetic moment lower than 2 mAm^2	To be updated after in-depth nominal mode control analysis
M.4	The magnetorquers shall have a peak dipole moment of at least 0.85 Am^2 (1.7 times nominal value)	Expected maximum torque near end of life

Now that the research objective is formed, some research questions can be created. The main research question will be:

Is it feasible to design a magnetorquer control system for SHAPE?

The sub-questions can be divided into two categories: the magnetorquer, and the control algorithm.

Magnetorquer sub-questions:

- What is a magnetorquer?
- How to design a magnetorquer?
- What are the performances of the magnetorquer?
- Are the requirements for the magnetorquer met?

Attitude control algorithm sub-questions:

- What attitude control algorithms exist that use only magnetorquers?
- How to design a control algorithm?
- What are the performances of the control loop?
- Are the requirements met for the attitude control loop?

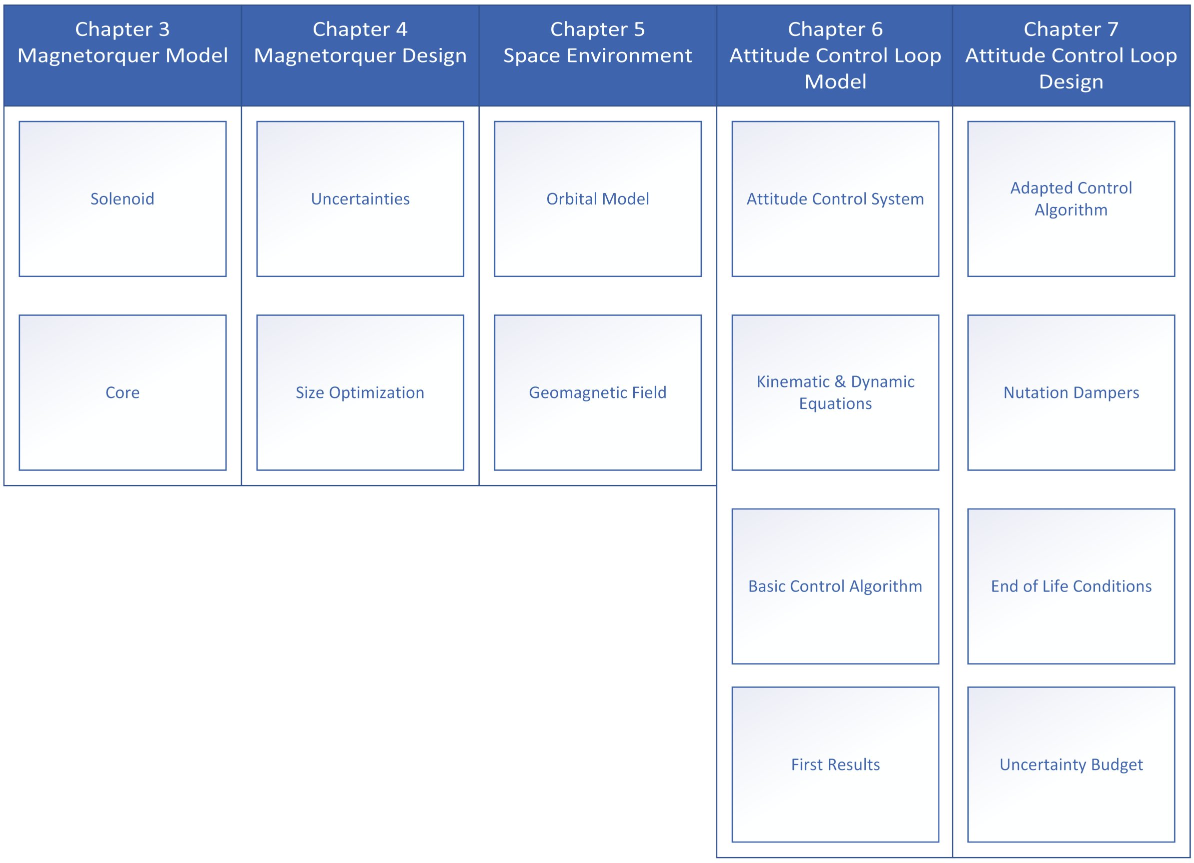

Figure 2.2: Thesis Breakdown

3

Magnetorquer Model

A magnetorquer is an actuator for the attitude control in spacecraft. It generates a magnetic dipole moment that interacts with the geomagnetic field to generate a torque to control the orientation of the spacecraft. The part of a magnetorquer that generates the magnetic dipole moment is a coil, where the amount of current regulates the strength of the dipole moment. The higher current, the higher the dipole moment. This coil is also called a solenoid, which will be used throughout the remainder of this report. To amplify the dipole moment a core can be implemented in the solenoid. This core is often a rod made from a ferromagnetic material, such as steel, nickel-iron alloys, or cobalt-iron alloys. Ferromagnetic materials are magnetized when in a magnetic field and will hold and amplify this field. Thus, when the external field is removed the rod will remain partially magnetized. This remaining magnetization is part of the hysteresis effect of these materials. A hysteresis curve can show what the remaining field is and what it takes to get it back to zero.

In this chapter, the different parts of the magnetorquer will be discussed separately. The chapter will start with listing the parameters that have to be taken into account when designing a magnetorquer, and their challenges in section 3.1. In section 3.2, the solenoid will be discussed and two models will be presented for which a trade-off will be done to find the most suitable model. Finally, the core will be discussed in section 3.3 where a model for the hysteresis curve is presented and verified for different materials. In figure 3.1 the structure for this chapter on the magnetorquer model is shown.

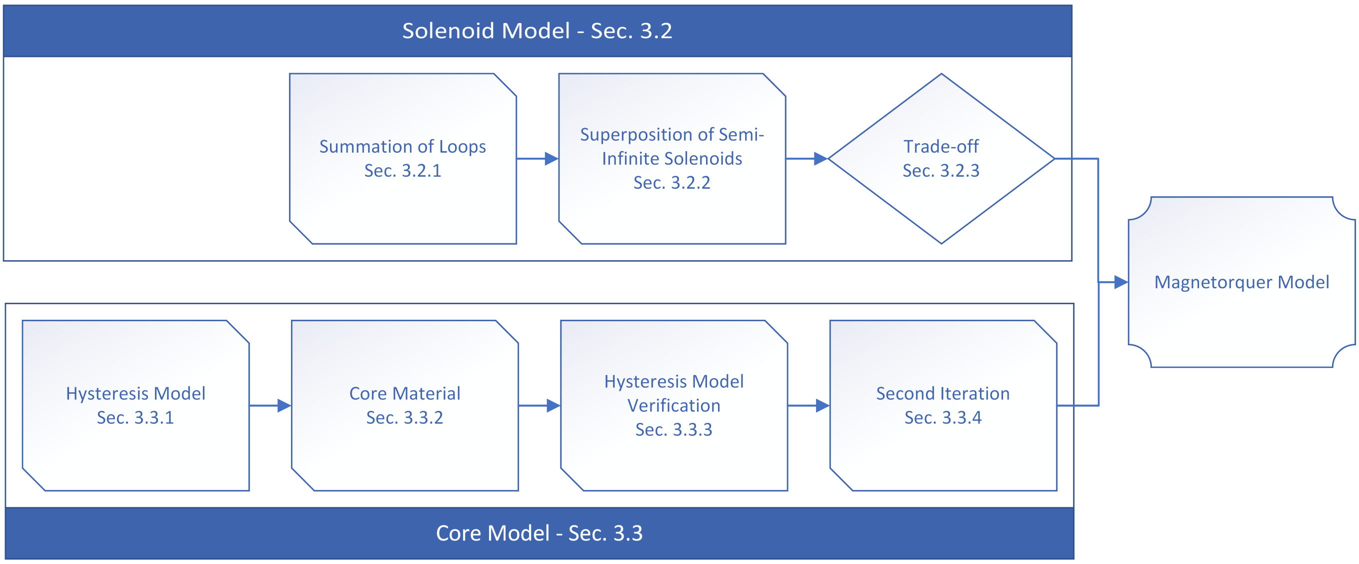

Figure 3.1: Diagram for magnetorquer design

3.1. Parameters and Challenges

First, the design parameters of the magnetorquers will be discussed. All these parameters will have their own uncertainties which should be taken into account when designing a magnetorquer. Next to the parameters of the magnetorquer itself, there are some external parameters which should be taken into account when designing a magnetorquer.

Parameters

The design parameters for the magnetorquers are as follows:

- Dimensions:
  - Diameter of the wire
  - Diameter of the coil
  - Length of coil
- Power loss due to coil resistance
- Maximum amount of current (that can be handled by the wire)
- Core material
- Mass
- Magnetic dipole moment

Next to these parameters there are some external parameters that should be taken into account, the following parameters were found:

- Geomagnetic field
- Temperature
- Orbit
- Position of the three magnetorquers relative to each other after mounting

Challenges

The fact that magnetorquers interact with the geomagnetic field causes certain challenges in the their usage. The system is non-linear, time-varying and the control torque is always perpendicular to the geomagnetic field vector, so it is not possible to provide three independent control torques at every time instant (Wisniewski and Blanke, 1996; Wang and Shtessel, 1998; Lovera and Astolfi, 2004; Silani and Lovera, 2005). For the implementation it is possible to use the assumption of periodicity of the geomagnetic field along the orbit, but this is only correct to a first order approximation and it can cause problems in designing a control loop (Wertz, 1978; Lovera and Astolfi, 2004; Silani and Lovera, 2005).

Shortly summarizing, the challenges are:

- Non-linearity
- Time-varying
- Control torque is always perpendicular to the geomagnetic field vector
- It is not possible to provide three independent control torques at every time instant
- Approximate periodicity of the geomagnetic field along the orbit

3.2. Solenoids

The solenoid, the coil that will be wrapped around the core and generates the magnetic field, is the base for the magnetorquer. Two models for the solenoid will be presented here. The first model is "Summation of elemental loops" and is discussed in section 3.2.1, the second model is "Superposition of Semi-Infinite Solenoids" and is discussed in section 3.2.2. These two models will be compared in section 3.2.3, where a trade-off will be done to find the best model for the final magnetorquer design.

3.2.1. Summation of Elemental Loops

The first method used to create the solenoid model is "Summation of elemental loops" (Montgomery, 1969). The axial and radial components of the magnetic field of an elemental loop can be calculated by equations (3.1) and (3.2), respectively.

$$H_z(z,r) = \frac{2I}{10a}\left[\frac{1}{\left[(1+r/a)^2+(z/a)^2\right]^{1/2}}\right]\left\{K(\phi)+\frac{1-(r/a)^2-(z/a)^2}{[1-(r/a)]^2+(z/a)^2}E(\phi)\right\} \tag{3.1}$$

$$H_r(z,r) = \frac{2I}{10a}\left(\frac{z}{r}\right)\left[\frac{1}{\left[(1+r/a)^2+(z/a)^2\right]^{1/2}}\right]\left\{-K(\phi)+\frac{1+(r/a)^2+(z/a)^2}{[1-(r/a)]^2+(z/a)^2}E(\phi)\right\} \tag{3.2}$$

$$k = \left[\frac{4(r/a)}{(1+r/a)^2+(z/a)^2}\right]^{1/2} = sin(\phi) \tag{3.3}$$

Where H is the magnetic field in Oersteds, I is loop current in Amperes, a is the radius of the loop in centimeters, r is the radial distance from the loop in centimeters, z is the axial distance from the loop in centimeters, $K(\phi)$ and $E(\phi)$ are the complete elliptic integrals of the first and second kinds, with ϕ as defined in equation (3.3). As can be seen, the units are not the standard units that are currently used. To convert this to more standard units the first terms in the equations of the magnetic field can be converted from $\frac{2I}{10a}$ to $\frac{I}{2\pi a}$, since Oersted is $\frac{1}{4\pi\cdot 10^{-3}}$ Ampere per meter and centimeter is 10^{-2} meter.

For $r = 0$, equations (3.1) and (3.2) are not valid, so an offset is given such that $r = 0$ becomes $r = 1\cdot 10^{-12}$. In this way, equations (3.1) and (3.2) can determine the value very close to $r = 0$, which then will be treated as the value at $r = 0$.

To be able to sum the elemental loops to a create a solenoid, the coordinates for each loop have to be translated to one central coordinate system with the origin at the center of the solenoid, since each loop will have its origin at the center of that loop itself. This will be done with equation (3.4).

$$z = Z - \left(\left(l/2 - d_{wire_{ins}}/2\right) - (j-1)\,d_{wire_{ins}}\right) \tag{3.4}$$

Where z is the axial distance in the coordinate system of each elemental loop itself, Z is the axial distance in the central coordinate system, l is the length of the solenoid, $d_{wire_{ins}}$ is the wire diameter including the insulation around the bare wire, j is the number of the wire going from 1 to N, where N is the total number of loops.

After calculating the magnetic field vector components for each loop in the central coordinate system, the vectors are summed together to find the total magnetic field in both the axial and radial direction.

3.2.2. Superposition of Semi-Infinite Solenoids

The second method to create the solenoid model is "Superposition of semi-infinite solenoids" (Brown and Flax, 1964). In this method the magnetic field components of a finite solenoid are calculated by superposition of four semi-infinite solenoids with zero inner radius (Brown and Flax, 1964). In figure 3.2 the four semi-infinite solenoids that form the finite solenoid are shown. The curved arrows indicate the direction of the current circulation. Also, note that each semi-infinite solenoid has its own coordinate system (Brown and Flax, 1964).

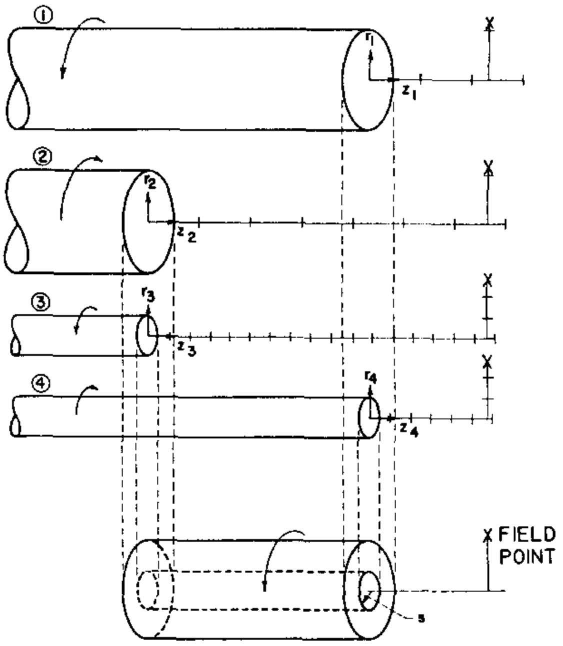

Figure 3.2: Four semi-infinite solenoids that create a finite solenoid (Brown and Flax, 1964)

The magnetic field components can be calculated by superposition of the magnetic field components of the four semi-infinite solenoids. This is done by equation (3.5), which can be used for both the axial and radial component.

$$H = H_1 - H_2 + H_3 - H_4 \tag{3.5}$$

Where the numbers refer to the numbers in figure 3.2. This equation is made non-dimensional by dividing by the current density J and the inner radius s, which becomes equation (3.6).

$$\frac{H}{Js} = \frac{H_1}{Js} - \frac{H_2}{Js} + \frac{H_3}{Js} - \frac{H_4}{Js} \tag{3.6}$$

The radii of the semi-infinite solenoids will be called b_1, b_2, b_3, b_4. Where $b_3 = b_4 = s$ and $b_1 = b_2 = \alpha s$. With this equation (3.6) becomes equation (3.7).

$$\frac{H}{Js} = \frac{\alpha H_1}{Jb_1} - \frac{\alpha H_2}{Jb_2} + \frac{H_3}{Jb_4} - \frac{H_4}{Jb_4} \tag{3.7}$$

Denoting the non-dimensional expressions like $\frac{H_1}{Jb_1}$ as h_1, etc. gives equation (3.8). Where h_1, etc. are the non-dimensional magnetic field components of the four semi-infinite solenoids.

$$\frac{H}{Js} = \alpha h_1 - \alpha h_2 + h_3 - h_4 \tag{3.8}$$

To make the radial and axial coordinates non-dimensional, they are expressed in terms of the radius of the semi-infinite solenoid as a unit of measurement. All the semi-infinite solenoids have their own coordinate systems with the origin at the center of the end face, which means a field point will have different coordinates with respect to each of the semi-infinite solenoids. This can be seen in figure 3.2 and equation (3.8) will become equation (3.9), where the field point coordinates are explicitly noted.

$$\frac{H}{Js} = \alpha h(r_1, z_1) - \alpha h(r_2, z_2) + h(r_3, z_3) - h(r_4, z_4) \tag{3.9}$$

Where the unit of measurement for r_1 and z_1 is $b1$, for r_3 and z_3 is b_3, etc. For the MATLAB model this is solved by equation (3.10).

$$\begin{aligned} r = \mathbf{R}./\mathbf{b} &= \begin{bmatrix} r_1 & r_2 & r_3 & r_4 \end{bmatrix} ./ \begin{bmatrix} \alpha s & \alpha s & s & s \end{bmatrix} \\ z = \mathbf{Z}./\mathbf{b} &= \begin{bmatrix} z_1 & l + z_2 & l + z_3 & z_4 \end{bmatrix} ./ \begin{bmatrix} \alpha s & \alpha s & s & s \end{bmatrix} \end{aligned} \tag{3.10}$$

The field components will be calculated by numerically integrating equations (3.11) and (3.12).

$$h_r(r,z) \equiv \frac{H_r}{Jb} = \frac{1}{2\pi}\int_0^{\pi} F\cos\theta d\theta + \frac{1}{2\pi}\int_0^{\pi} r\cos^2\theta \sinh^{-1}\left[\frac{1-r\cos\theta}{\left(z^2+r^2\sin^2\theta\right)^{\frac{1}{2}}}\right]d\theta \tag{3.11}$$

$$\begin{aligned} h_z(r,z) \equiv \frac{H_z}{Jb} = \frac{1}{2\pi}\left\{-z\int_0^{\pi} ln\left[\frac{2(1-r\cos\theta+F)}{|z|+\left(z^2+r^2\right)^{\frac{1}{2}}}\right]d\theta + zr^2\int_0^{\pi}\frac{\sin^2\theta}{\left(1+r^2-2r\cos\theta\right)F}d\theta\right\} \\ +\frac{1}{2\pi}\left\{\frac{rz}{|z|}\int_0^{\pi}\sin\theta\tan^{-1}\left[\frac{(1-r\cos\theta)|z|}{r\sin\theta F}\right]d\theta + \frac{\pi}{2}(1-r+|1-r|)\right\} \end{aligned} \tag{3.12}$$

Where $F = \left(z^2+r^2+1-2r\cos\theta\right)^{\frac{1}{2}}$.

The second integral in h_r is indeterminate for $z = 0$, so this point should be either avoided by an offset or integrated by parts analytically to avoid difficulties in the MATLAB model (Brown and Flax, 1964). In the MATLAB model an offset of $1 \cdot 10^{-7}$ is given if $z = 0$. For smaller values MATLAB cannot determine all the numerical integrals.

The field components have to be calculated for each field point and for each semi-infinite solenoid. This takes a substantial time, since it is performing five numerical integrations each time.

To find the dimensional magnetic field equation (3.13) is used for both the axial and radial components.

$$H = \frac{H}{Js}\cdot J \cdot s \tag{3.13}$$

"The semi-infinite solenoid is defined as an axially symmetric, uniform, azimuthal current density" (Brown and Flax, 1964). This means that it is defined as a current sheet, which has a different cross-sectional area as wounded wires. To account for this a correction factor is found in equation (3.14).

$$\begin{aligned} A_{wire} &= x \cdot A_{sheet} \\ N\cdot\pi\cdot\left(\frac{d_{wire}}{2}\right)^2 &= x\cdot d_{wire_{ins}}\cdot l, \\ l = d_{wire_{ins}}\cdot N\,,\ \ d_{wire_{ins}} &= 1.06\cdot d_{wire} \\ \Rightarrow N\cdot d_{wire}^2\cdot\frac{\pi}{4} &= x\cdot 1.06^2\cdot d_{wire}^2\cdot N \\ \Rightarrow x &= \frac{\pi}{4\cdot 1.06^2} \end{aligned} \tag{3.14}$$

Implementing this factor in the magnetic field equation gives equation (3.15).

$$H = \frac{H}{Js}\cdot J\cdot s\cdot x \tag{3.15}$$

3.2.3. Comparison and Trade-off

The models have a magnetic field as shown in figure 3.3, the magnetic field for "Summation of loops" is shown, but the other aforementioned model looks the same. The two models are compared to each other, in terms of magnetic field magnitude, and calculation time. The models are compared by subtracting the "Superposition of semi-infinite solenoids" from the "Summation of Loops", and by taking this as a percentage of the "Summation of Loops", as well.

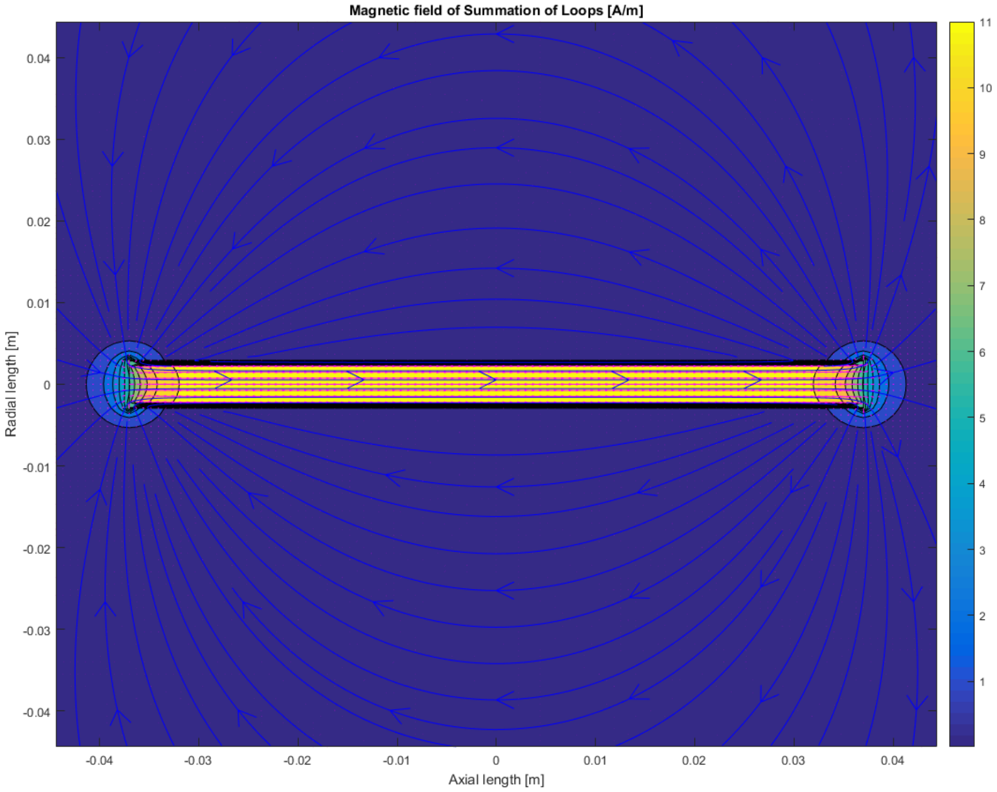

Figure 3.3: Magnetic field from a solenoid, calculated with the "Summation of loops' model.

In figure 3.4, the differences in value and percentage are shown. The models are within 1.0% from each other, the areas where higher percentages are visible around the edges of the solenoids. This is expected since those areas have computational singularities. For example, in the "Superposition of semi-infinite solenoids" an offset was given to the ends of the solenoid, because the equations are singular there. In the figures the wires are whited out, since the data there is large varying. This is caused by the modeling of the wires, "Summation of loops" sees single wires, where "Superposition of semi-infinite solenoids" sees a current sheet.

The main other difference between the models is the calculation time. The 'Superposition of semi-infinite solenoids' takes about 70 times longer than the "Summation of loops". The main issue in "Superposition of semi-infinite solenoids" is that it executes five integrals for each of the four semi-infinite solenoid per grid point. While in the other model only the elliptical integrals are recalculated per grid point.

One of the models will be used for the final magnetorquer model. Since the models only differ by 1.0% or less, which is acceptable for this application, the model with the shortest computation time will be used. This means the "Summation of loops" will be used in the final model.

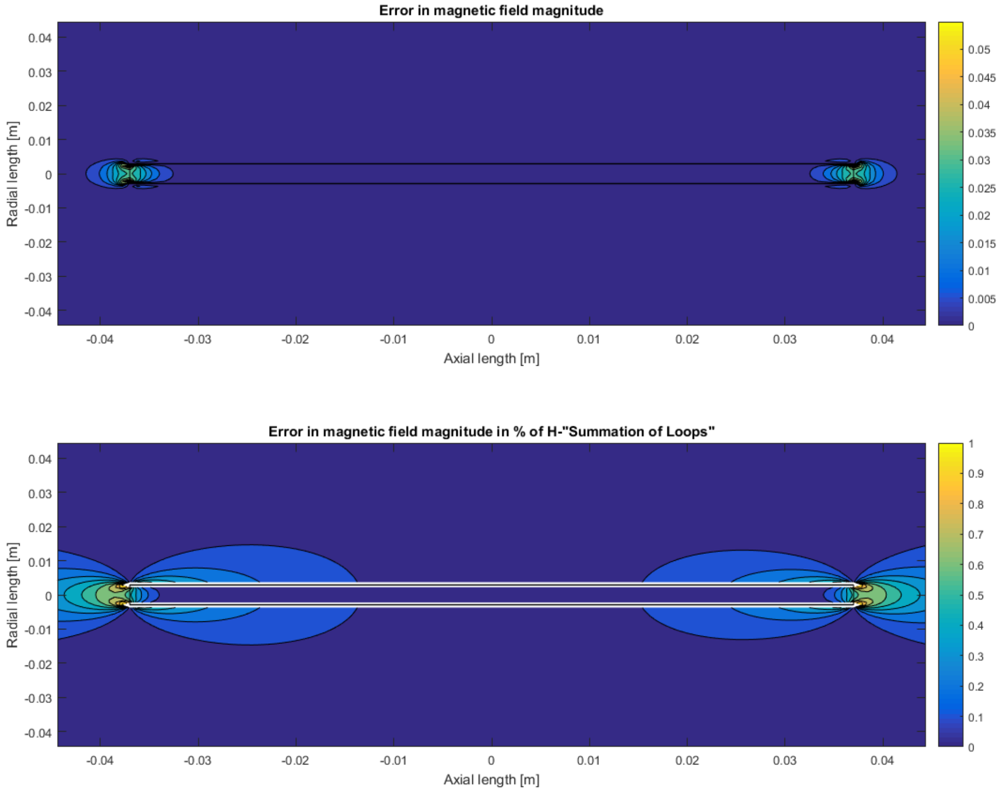

Figure 3.4: Comparison of the magnetic field magnitude, in the top figure the error in magnitude is shown, in the bottom figure in percentage.

3.3. Core Model

The core is an important part of the magnetorquer since it will increase the maximum magnetic induction significantly. But it also has some other side effects like hysteresis. A hysteresis model will be discussed here.

For the core there are some important material properties that will be used for creating the hysteresis model and will determine what materials are suitable. In figure 3.5 a hysteresis loop is shown with the important points. The points are as follows:

a) Saturation (H_s,B_s); This is the magnetic field strength where the maximum magnetic induction is reached.

b) Retentivity (B_r); This is the amount of magnetic induction that remains when the magnetic field strength is reduced to zero from saturation.

c) Coercivity (H_c); This is the magnetic field strength that is needed to reduce the magnetic induction to zero.

d) Saturation in the other direction.

e) Retentivity in the other direction.

f) Coercivity in the other direction.

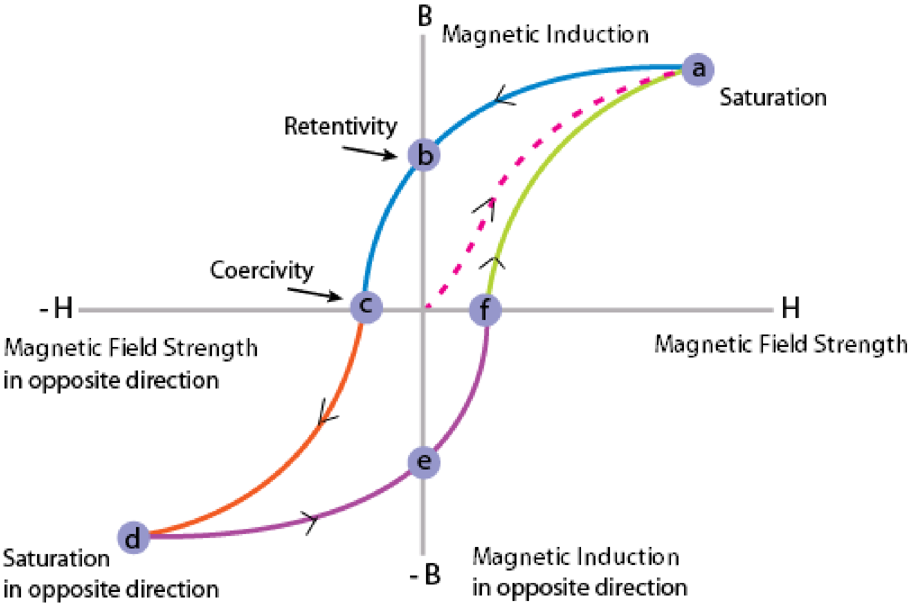

Figure 3.5: Hysteresis loop with important points, (ElectricalEngineering123, 2016)(edited)

3.3.1. Hysteresis Model

There are several models that present a method to simulate the hysteresis curve of a material. However, most of these methods make use of measurement data that needs to be measured for the material that is going to be used, and this data is also not readily available. Since no measurements can be performed, and a general model is desired, most of these methods are discarded. The method "Mathematical Model of Major Hysteresis Loop and Transient Magnetizations" (Milovanovic and Koprivica, 2015) will be used and implemented in this magnetorquer model. It used measurement data in the paper as well, but the method is explained in such a way that there is a way to work around the need of measurement data. First, the major hysteresis loop and the initial magnetization curve will be discussed, then the minor loops.

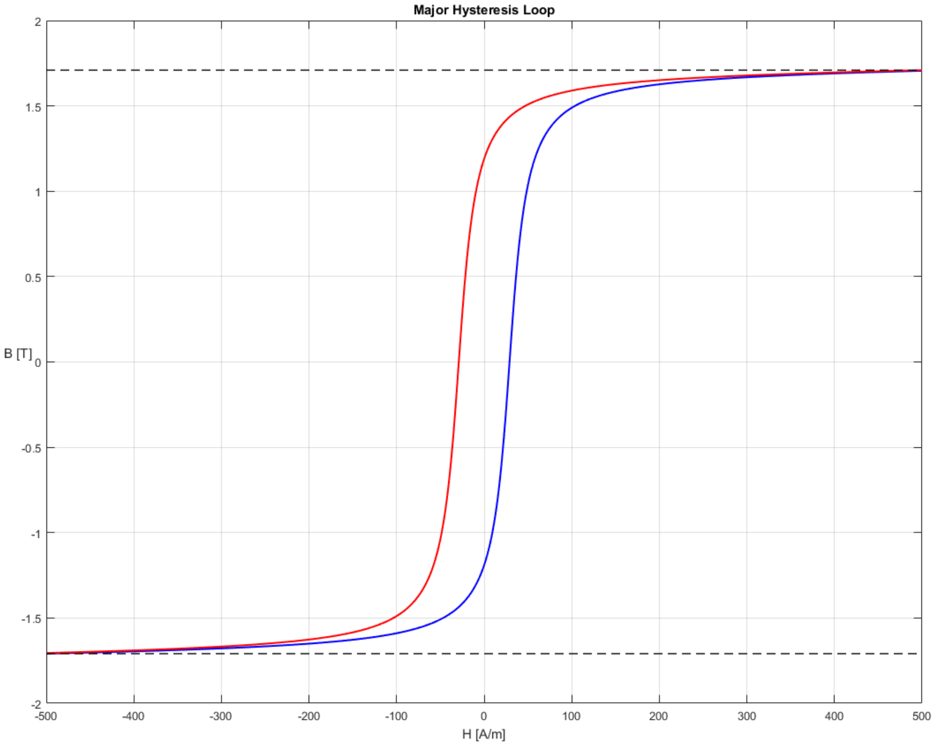

Figure 3.6: Major hysteresis loop. The red line is the descending trajectory, the blue line is the ascending trajectory, and the black dashed line is the saturation level

Major Hysteresis Loop

First the major hysteresis loop has to be modeled, this is done by an arctangent model that is represented in equation (3.16). Where the + sign is for the descending trajectory and the − sign for the ascending trajectory.

$$B = a \arctan\left[b\left(H \pm d\right)\right] + cH \tag{3.16}$$

The parameters a, b, c, and d are expressions using the key magnetic properties of the material, and are presented in equation (3.17). B_s is the magnetic induction at saturation, B_r is the remanent magnetic induction, H_c is the coercive magnetic field, and H_s is the saturation magnetic field.

$$a = \frac{2B_s}{\pi} \qquad b = \frac{\tan\left[\frac{\pi B_r}{2B_s}\right]}{H_c} \qquad c = \frac{B_s - \frac{2}{\pi} B_s \arctan\left[b\left(H_s + H_c\right)\right]}{H_s} \qquad d = H_c \tag{3.17}$$

In figure 3.6 the major hysteresis loop is shown with the values from the paper (Milovanovic and Koprivica, 2015); $B_s = 1.71\text{T}$, $B_r = 1.19\text{T}$, $H_c = 29\text{A/m}$, and $H_s = 500\text{A/m}$. In this graph, the blue line represents the descending trajectory and the red line represents the ascending trajectory, the black dashed lines represent the magnetic induction saturation values. This loop is now symmetrical, while a real loop is only partially symmetrical. The positive part of the descending curve and the negative part of the ascending curve will have different parameters, which can be determined by shifting the ascending curve of the *measured* major loop horizontally to the point $(H_c, 0)$. A new value for the remanence will be found, B_{rf}, the so called fictitious remanence, which has a lower value than the remanence B_r. The new pair of equations can be found in equation (3.18). Since the measured curve is not available, this part will be done differently and explained later.

$$\begin{aligned} B &= \pm a \arctan\left[b\left(\pm H + d\right)\right] + cH \\ B &= \pm a_1 \arctan\left[b_1\left(\pm H - d_1\right)\right] + c_1 H \end{aligned} \tag{3.18}$$

Initial Magnetization Curve

The next step is the initial magnetization curve. This is the line that will be followed when for the first time a magnetic field is applied and the core is not magnetized yet. In equation (3.19) the expression is given for the initial magnetization, which again uses an arctangent model, like the major loop. The parameters a_2, b_2, c_2, and k_{max} can be determined by equation (3.20), here the parameters a, b, and c come from equation (3.17) and k has a value between $0.3k_{max}$ and $0.7k_{max}$ (Milovanovic and Koprivica, 2015).

$$B_{init} = B + k\frac{d^2B}{dH^2} \qquad B = a_2 \arctan(b_2 H) + c_2 H \tag{3.19}$$

$$a_2 = a \qquad b_2 = \frac{b}{2} \qquad c_2 = 2c \qquad k_{max} = \frac{a_2 b_2 + c_2}{2a_2 b_2^3} \tag{3.20}$$

Correction on Major Hysteresis Loop and Initial Magnetization Curve

Above, it was mentioned that the hysteresis loop is not supposed to be symmetrical and that one part can be found by using a measured loop. Since this measured loop is not available, a different method is used to find the parameters of this part of the loop. This method will use an optimization on the major loop area. The parameters a_2, b_2, and c_2 will be optimization parameters, k_{max} will change such that the slope of the initial magnetization near zero will be representing the initial permeability:

$$k_{max} = \frac{a_2 b_2 + c_2 - f_k \cdot \mu_i}{2a_2 b_2^3} \tag{3.21}$$

where μ_i is the initial permeability, and f_k is an optimization factor to make it fit. A new value for the remanence will be used, B_{rf}, the fictitious remanence. The initial value will be the magnetic induction of the initial magnetization curve at H_c, and a optimization factor f will be used to find a fitting value. The optimization is outlined as follows:

$$\begin{aligned}
&\min_{a_2,b_2,c_2,f,fk} Area\left(a_2, b_2, c_2, f, fk\right)\\
\text{Subject to: } & B_a - B_d \le 0\\
& B_a - B_{init} \le 0\\
& B_{init} - B_d \le 0\\
& max(B_{init}/H)/(1.3\mu_{max}) - 1 \le 0\\
& (0.7\mu_{max})/max(B_{init}/H) - 1 \le 0\\
& (B_{init}/H)_{@0.002T}/(1.3\mu_i) - 1 \le 0\\
& (0.7\mu_i)/(B_{init}/H)_{@0.002T} - 1 \le 0\\
& 0.9a \le a_2 \le 1.1a\\
& 0.7\frac{b}{2} \le b_2 \le 1.1\frac{b}{2}\\
& 2c \le c_2 \le 6\cdot 2c\\
& 0.1 \le f \le 5\\
& 0.1 \le f_k \le 2
\end{aligned}$$

With initial conditions: $a_2 = a$, $b_2 = \frac{b}{2}$, $c_2 = 2c$, $f = 1.6$, $f_k = 0.9$.

The new major hysteresis loop with the initial magnetization curve are shown in figure 3.7. A flowchart of these calculations can be found in figure 3.8.

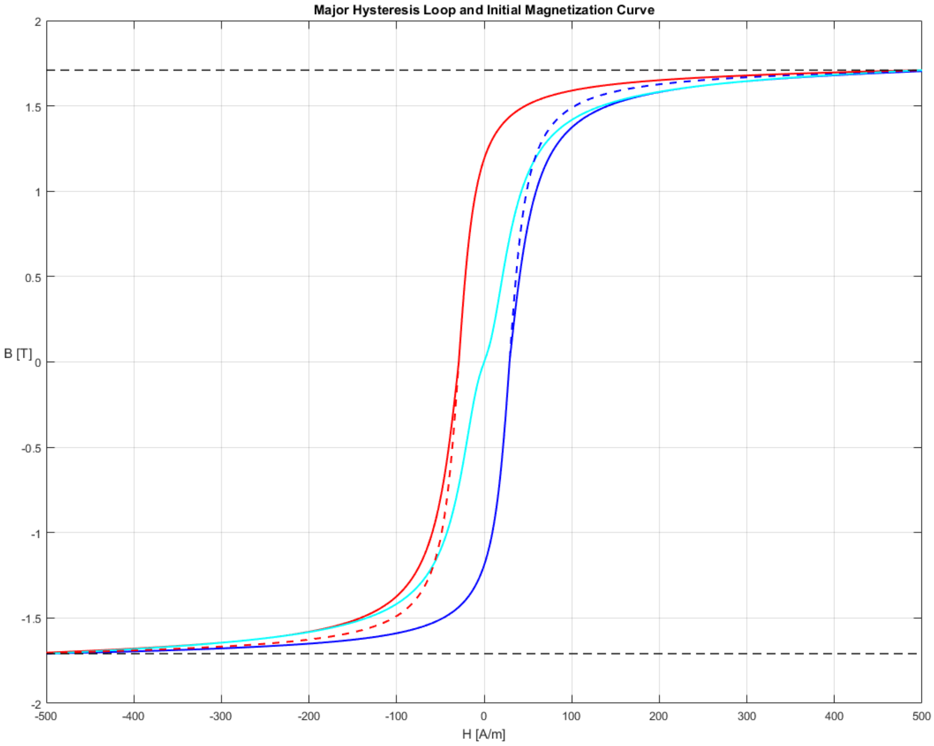

Figure 3.7: Major hysteresis loop and initial magnetization curve. The dashed lines are the symmetric major loop parts, as in figure 3.6, the solid lines are the new major loop lines. The cyan line is the initial magnetization curve.

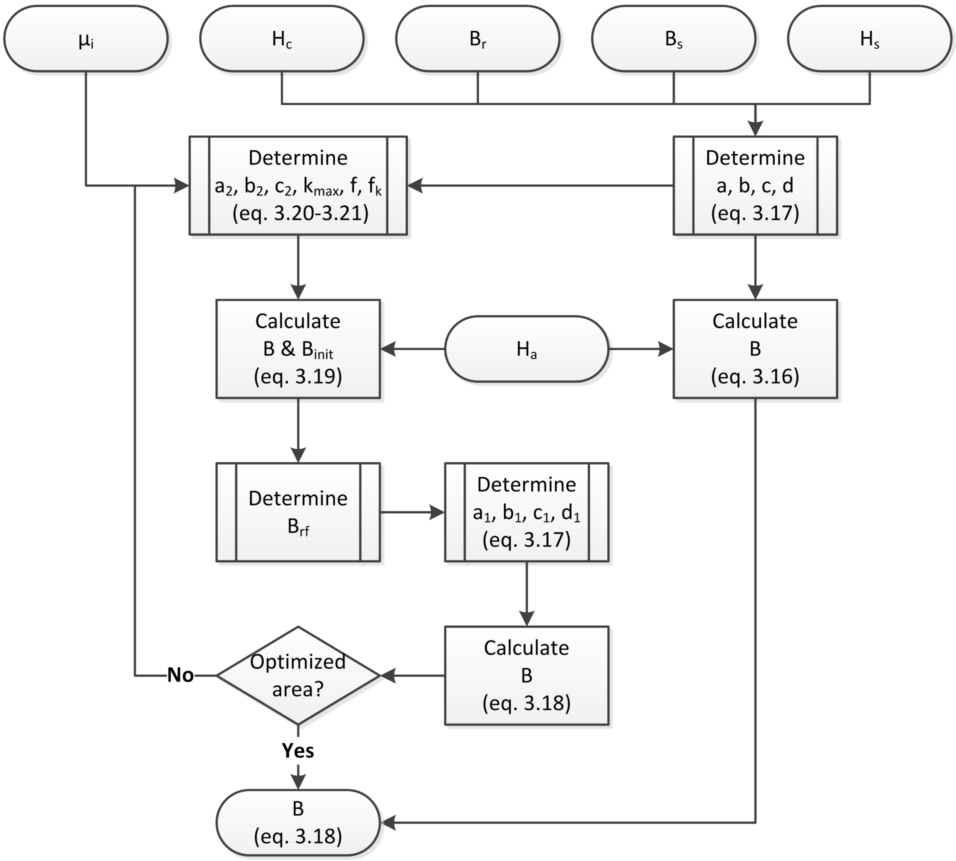

Figure 3.8: Flowchart about the calculations of the major hysteresis loop and initial magnetization curve

Minor Loops

The minor loops are constructed by shifting the major loop. The expressions used to model them can be found in equation (3.22). The expressions on the left side are for the ascending part of the loop, and on the right side the expressions are for the descending part can be found. Here $B_a(H)$ is the ascending part of the major loop as in equation (3.18), B_{reva} and B_{revd} are the values of the magnetic induction at the reversal magnetic field H_{rev}, $B_d(H)$ is the descending part of the major loop, and β is a parameter which can be determined by fitting to the measured results. Since these measured results are not available and some other criteria are given in the paper (Milovanovic and Koprivica, 2015), these other criteria will be used to determine β. To calculate β, the shift is to the initial magnetization curve at $P_1(-H_1, -B_1)$, where $H_1 = H_{rev}$ and $B_1 = B_{init}(H_1)$. Once shifted, a β has to be found that makes the curve pass through point $P_2(H_1, B_1)$. This will create the symmetrical minor loop, since point P_1 and P_2 are the tips of this minor loop. A series of minor loops are shown in figure 3.9 and a flowchart for the ascending part is shown in figure 3.10.

$$\begin{aligned} B_{Ma} &= B_a(H) - s_1 - s_2 & B_{Md} &= B_d(H) - s_1 + s_2 \\ s_1 &= s_{maxa}\left(\frac{B_a(H) - B_s}{B_{reva} - B_s}\right)^{(1+\beta B_d(H))} & s_1 &= s_{maxd}\left(\frac{B_d(H) + B_s}{B_{revd} + B_s}\right)^{(1-\beta B_a(H))} \\ s_{maxa} &= B_{reva} - B_{revd} & s_{maxd} &= B_{reva} - B_{revd} \\ s_2 &= |B_{revd} - B_{revi}| & s_2 &= |B_{reva} - B_{revi}| \end{aligned} \tag{3.22}$$

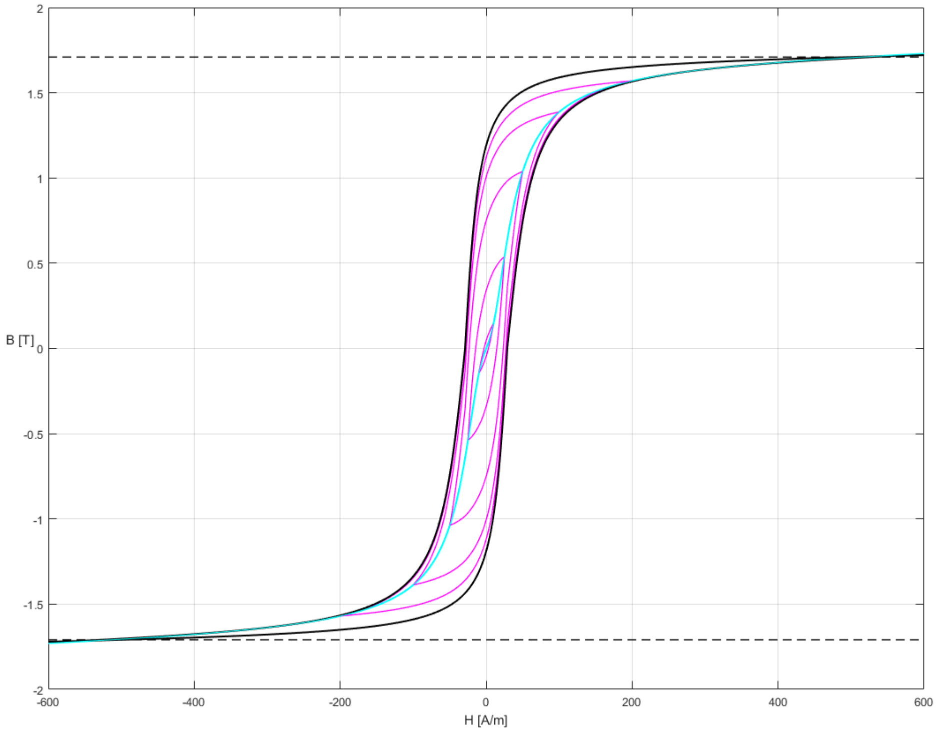

Figure 3.9: Major loop, and minor loops for $H_{rev} = -10, -25, -50, -100, -200$

The accuracy of the MATLAB simulation can be checked by comparing the loop area with the measured value from the paper (Milovanovic and Koprivica, 2015). The measured loop area is 247.418, in the MATLAB simulation a value of 238.361 is found. This is 3.7% less than the measured value. In the paper a value of -2.1% is reached, but here the parameters are modified to fit the measured curve. A value of -6.87% is found before modifying the parameters to fit the measured curve. This shows that the simulation produces acceptable results, without the use of any measured curves.

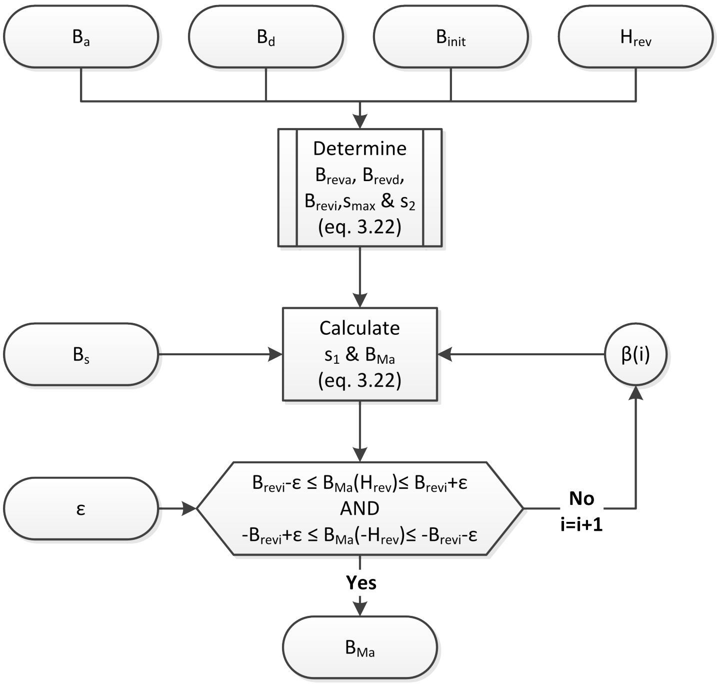

Figure 3.10: Flowchart about the calculation of the FORCs and minor loops

3.3.2. Core Materials

There are two main types of magnetic materials; hard magnetic and soft magnetic materials. Hard magnetic materials have a high retentivity and high hysteresis losses. Soft magnetic materials have lower retentivity and lower hysteresis losses. Soft magnetic materials are easily magnetized and demagnetized. Hard magnetic materials retain there magnetization and are not easily demagnetized.

Soft magnetic materials are the preferred core materials since they have a lower hysteresis loss. Criteria to take into account when looking for a suitable magnetic material, are;

- High initial permeability, μ_i
- High maximum permeability, μ_{max}
- High saturation value, B_{sat}
- Low coercivity, H_c
- Low retentivity, B_r
- High resistivity
- Low density

Common materials for small magnetorquers are iron and permalloy (a nickel-iron alloy). However, there are more magnetic materials to choose from. In table 3.1 different materials are shown with their magnetic properties. Most of the data in this table comes from McLyman (2004).

Table 3.1: Magnetic material properties

Property Material	μ_i	μ_{max}	B_{sat} Tesla	H_c A/m	B_r Tesla	H_{sat} A/m	Resistivity Ohm-m	Density kg/m^2
4% Silicon-Iron	1500	17647	1.60	41.38	1.51	127.32	47e-3	7670
45 Permalloy +	4000	12732	0.54	9.00	0.28	100.00	45e-3	8170
Hipernik	4500	62500	1.47	11.74	1.41	43.77	50e-4	8250
78 Permalloy	8000	48000	0.84	3.98	0.66	79.58	16e-3	8600
4-79 Mo-Permolloy	20000	117500	0.77	2.39	0.62	13.53	55e-3	8720
Supermalloy	100000	222222	0.73	0.64	0.24	12.73	60e-3	8770

3.3.3. Core Model Verification

Verification of the core model, mainly the hysteresis curve, is an important step. If the model does not represent a real curve, it is useless. Some reference curves can be found in books and papers (McLyman, 2004; *Permalloy materials (YFN-45)*, 2007). These reference curves will be compared to the outcome of the model. The materials from table 3.1 will be used for the verification. These materials are chosen as possible good core materials, so this is not a general verification, but a case specific one.

In figure 3.11 the hysteresis curves from the model and the reference curves will be compared. The magenta curve is from the model, the cyan curve is the initial magnetization curve, and the blue curve is the reference curve.

As can be seen from the figures, not all materials have good results. The three materials that do show good results are: 45 Permalloy, 78 Permalloy, and 4-79 Mo-Permalloy. These three materials will be used in the next chapter to optimize the magnetorquer for each material, and to choose one of these as recommended magnetorquer. This result also cause to do a second iteration on the hysteresis model, which will be discussed in section 3.3.4. The results from this second iteration will then be used for another magnetorquer size optimization to see if the same material is still recommended, or that an other material is better.

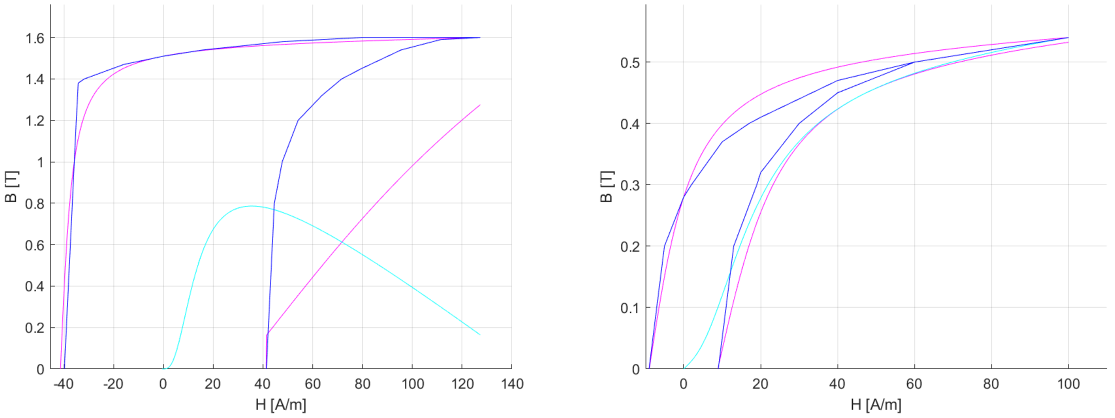

(a) Hysteresis curve verification for Silicon Iron

(b) Hysteresis curve verification for 45 Permalloy

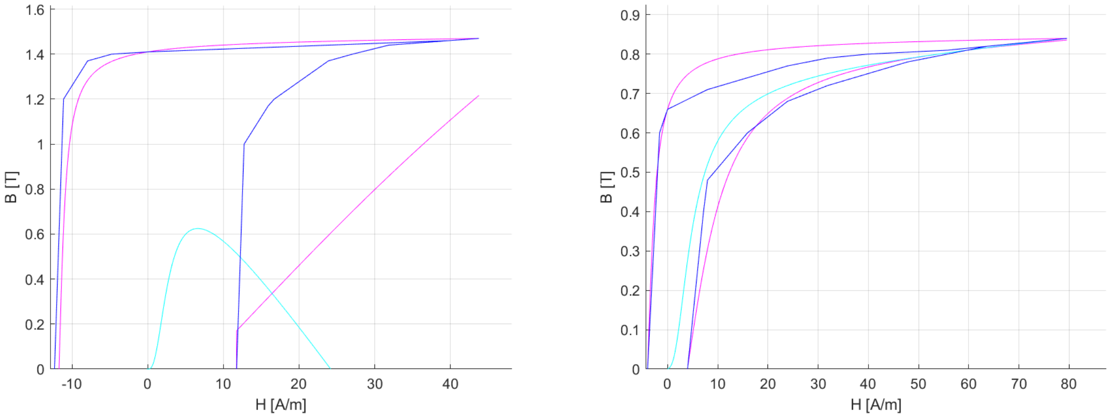

(c) Hysteresis curve verification for Hipernik

(d) Hysteresis curve verification for 78 Permalloy

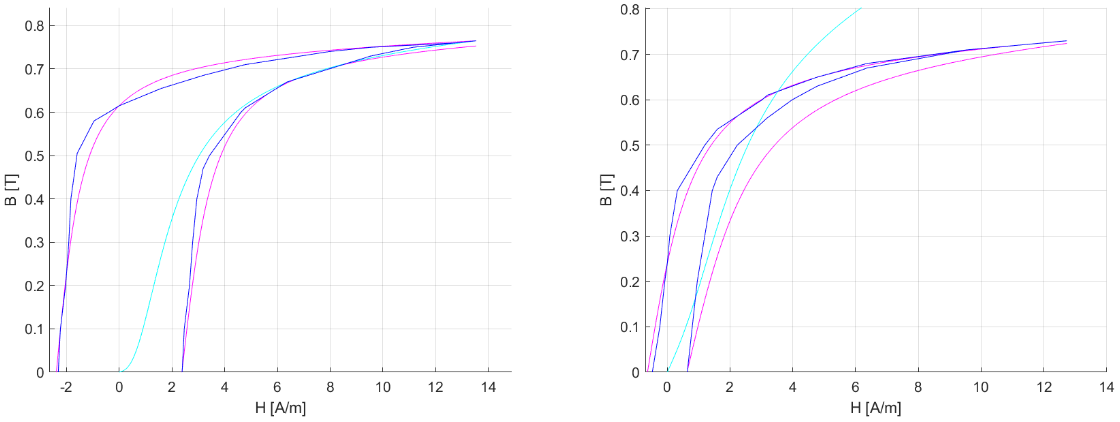

(e) Hysteresis curve verification for 4-79 Mo-Permalloy

(f) Hysteresis curve verification for Supermalloy

Figure 3.11: Hysteresis curve verification. The magenta curve is from the model, the cyan curve is the initial magnetization curve, and the blue curve is the reference curve.

3.3.4. Second Iteration on Hysteresis Model

This second iteration of the hysteresis model is done after the reference curves were found. With these curves, the model described in the paper (Milovanovic and Koprivica, 2015) can be followed better than done previously.

For the major hysteresis curve the value for B_{rf} can be found by shifting the reference curve horizontally to the point $(H_c, 0)$, like described earlier in section 3.3.1. In figure 3.12, the major loop (and initial curve) are shown for the model from the paper. To check if the result is the same as in the paper, the area within the major curve can be compared. According to the paper the area between the dotted blue lines has to be 194.46 and between the solid magenta lines 230.41 (Milovanovic and Koprivica, 2015). This is true for this figure, so this proves that the major loop model produces the same results as in the paper.

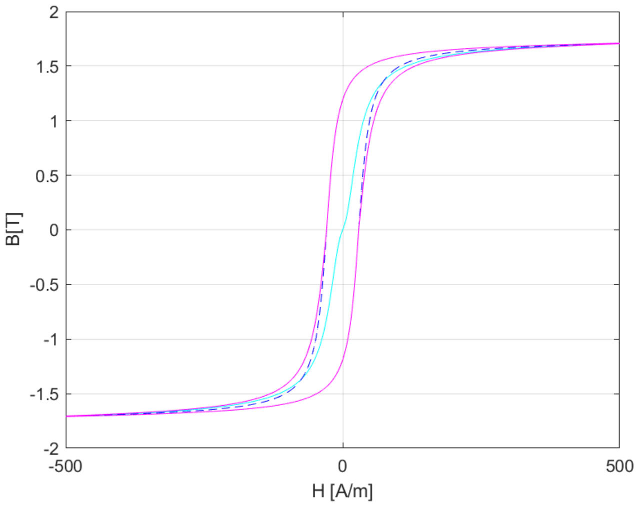

Figure 3.12: Hysteresis curve for the model from Milovanovic and Koprivica (2015)

For the initial magnetization curve the value for k_{max} can be taken as in equation (3.20), instead of equation (3.21). According to the paper the value for k is between $0.3k_{max}$ and $0.7k_{max}$, but this together with the other parameters (a_2, b_2, c_2) did not work for most materials. To solve this, some criteria were set such that the initial curve will always within the major curve and ends at the saturation values (H_s, B_s). This was formulated into a minimization problem where the error in the endpoint will be minimized, and is outlined as follows:

$$\begin{aligned}
&\min_{a_2,b_2,c_2,f,f_k} \; e_{end}\left(a_2, b_2, c_2, f_k\right)\\
&\text{Subject to: } B_a - B_d \leq 0\\
&\qquad B_a - B_{init} \leq 0\\
&\qquad B_{init} - B_d \leq 0\\
&\qquad (B_{init}/H)_{@0.002T}/(1.3\mu_i) - 1 \leq 0\\
&\qquad (0.7\mu_i)/(B_{init}/H)_{@0.002T} - 1 \leq 0\\
&\qquad 0.8a \leq a_2 \leq 1.1a\\
&\qquad 0.2\frac{b}{2} \leq b_2 \leq 2\frac{b}{2}\\
&\qquad 0.5 \cdot 2c \leq c_2 \leq 10 \cdot 2c\\
&\qquad 0.3 \leq f_k \leq 1.0
\end{aligned}$$

With initial conditions: $a_2 = a$, $b_2 = \frac{b}{2}$, $c_2 = 2c$, $f_k = 0.7$.

In figure 3.13, the new hysteresis curves are shown together with the reference curves. For 78 Permalloy the fit was not good, so the parameters were tweaked by hand to make a better fit. The parameters a, b, c, a_1, b_1, and c_1 were tweaked, since they define the shape of the hysteresis curve. The new values can be found in table 3.2. The result of tweaking the parameters is shown in figure 3.14. This shows that with this method a good first approximation of the hysteresis curve can be formed and that with some tweaking a better fitting curve can be created.

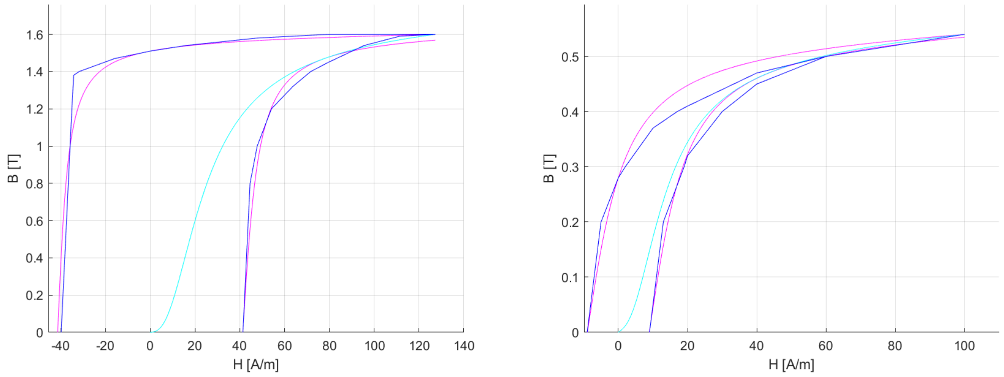

(a) New hysteresis curve verification for Silicon Iron

(b) New hysteresis curve verification for 45 Permalloy

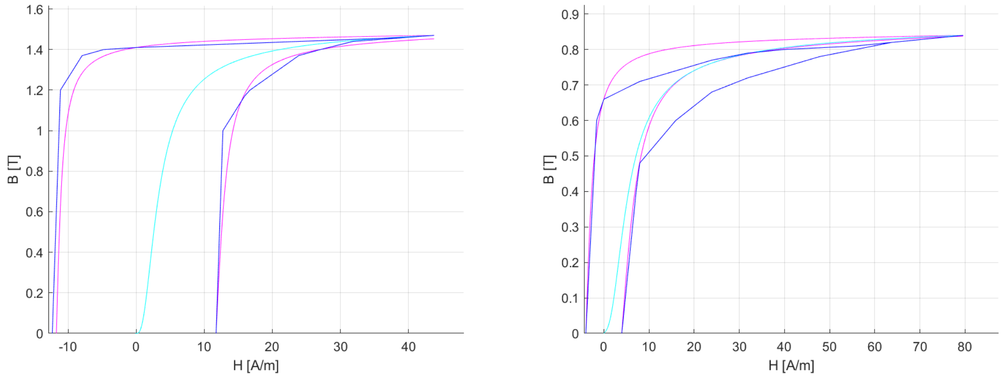

(c) New hysteresis curve verification for Hipernik

(d) New hysteresis curve verification for 78 Permalloy

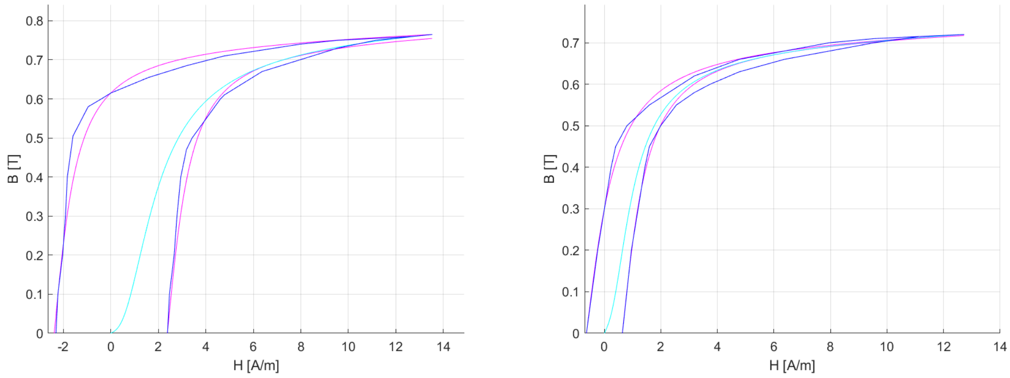

(e) New hysteresis curve verification for 4-79 Mo-Permalloy

(f) New hysteresis curve verification for Supermalloy

Figure 3.13: New hysteresis curve verification

Table 3.2: Tweaked parameters for 78 Permalloy

$a = 0.9a$	$a_1 = 0.8a_1$
$b = 1.1b$	$b_1 = 1.2b_1$
$c = 11.3c$	$c_1 = 10.8c_1$

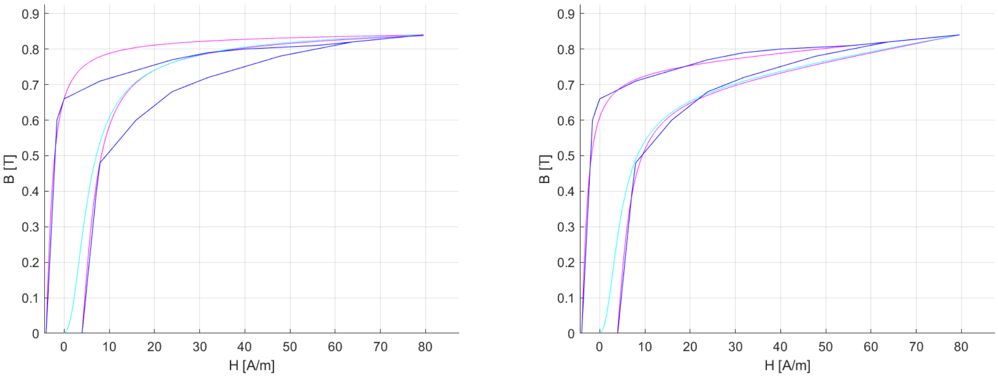

(a) New hysteresis curve verification for 78 Permalloy

(b) Tweaked new hysteresis curve verification for 78 Permalloy

Figure 3.14: Comparison of the initial new hysteresis curve for 78 Permalloy with one where the parameters were tweaked such that the curve would fit the reference curve better.

4

Magnetorquer Design

In this chapter the final magnetorquer design will be presented. The magnetorquer will be optimized to have minimum mass, be within the dimension limits, and still produce the required magnetic dipole moment. After this optimization, a sensitivity analysis will be performed to see what the influence is from the different design parameters on the mass, volume, magnetic dipole moment, and power.

First, an uncertainty budget for the magnetorquer is made in section 4.1. Then the power calculations are shown in section 4.2. The optimization of the magnetorquer with the different core materials will be done in section 4.3 and the sensitivity analysis in section 4.4. Finally, the final magnetorquer will be discussed in section 4.5.

4.1. Uncertainty Budget

The uncertainties in the magnetorquer design and its surrounding are of importance for the performance of the magnetorquer and whether it can meet up with the requirements or not. Therefore, an uncertainty budget is made to have an overview of all the uncertainties that have to be taken into account for the final magnetorquer model.

4.1.1. Dimension

There are always uncertainties in the manufacturing. The wire and insulation can be a bit thicker or thinner. For the (bare) wire, the tolerance increases with thickness. These tolerances can be found in table 4.1.

Table 4.1: Tolerances on the bare wire (Elektrisola, 2015)

Nominal bare wire diameter	Tolerance
mm	mm
0.071 - 0.224	± 0.003
0.236 - 0.355	± 0.004
0.400 - 0.500	± 0.005

The enamel coating around the wire (as insulation) also has tolerances. In table 4.2 a short overview of some wire thicknesses is shown, a full table is available from (Elektrisola, 2015).

4.1.2. Material Properties

The material properties of both the wire and the core have uncertainties. Starting with the thermal coefficient of resistance for the copper wire in table 4.3.

The core material properties, as shown earlier in table 3.1, can be found in books and papers, but are un-

Table 4.2: Minimum and maximum thickness summary on grade 1 enamelled copper wire (Elektrisola, 2015)

Nominal bare wire diameter	Minimum diameter	Maximum diameter
mm	mm	mm
0.071	0.078	0.084
0.095	0.103	0.111
0.118	0.128	0.136
0.140	0.151	0.160
0.190	0.204	0.216
0.250	0.267	0.281
0.335	0.255	0.372
0.450	0.472	0.491
0.500	0.524	0.544

Table 4.3: Temperature coefficient of resistance for a copper wire

Temperature coefficient in 10^{-3} per °C		
Minimum	Nominal	Maximum
3.900	3.930	4.300

fortunately not always the same everywhere. For some values it has shown that they can differ up to 6 times, but most of the time is 30% or less. These big differences mainly happen in the permeability, in for example the coercivity the uncertainty is usually around 5% or less, and the density is usually within 0.3%. These uncertainties have been taken into account already in the hysteresis curve correction in section 3.3.1.

4.1.3. Environment

The environment in which the magnetorquers have to function, is important for their performance. The temperature of the environment is the main factor here. Generic electronics have a typical operating temperature range between -20 and +70 °C (Parolis and Pinter-Krainer, 1996), so this range will be used in the coming sensitivity analysis.

4.2. Power Calculations

The magnetorquer is allowed to use a maximum amount of power, which is given in the requirements. There are two components that will contribute to the power consumption, the solenoid and the core. The solenoid will contribute directly by drawing current from the system and has resistance in the wire, and the core contributes by having hysteresis loss.

Solenoid

The solenoid is basically a wire turned into a coil, so it can be treated as a wire with a certain length and diameter. The power can be calculated by equation (4.1).

$$\begin{aligned} P &= I^2 R \\ I &= \frac{V}{R} \\ R &= \frac{\rho l}{A} \end{aligned} \tag{4.1}$$

Where P is the power in W, I is the current in A, V is the voltage in V, R is the resistance in Ω, ρ is the resistivity of the wire material in Ω/m, l is the length of the wire in m, and A is the cross-sectional area of the wire in m^2. When using a copper wire the resistivity is $1.71 \cdot 10^{-8}$ Ω/m (Elektrisola, 2015).

The resistance of the wire is temperature sensitive, and can be determined by equation (4.2). The thermal coefficient, α_T, is specified in table 4.3, R is the resistance as specified in equation (4.1), T is the wire temperature, and T_a is the ambient temperature.

$$R_T = R(1 + \alpha_T (T - Ta)) \tag{4.2}$$

With this, the power from the wire becomes:

$$P_{wire} = I^2 R_T \tag{4.3}$$

Core

The hysteresis loss of the core is the enclosed area of the hysteresis loop. This can be determined by the integral in equation (4.4), but will be evaluated numerically in Matlab.

$$P_h = \int H dB \tag{4.4}$$

Total Power

The total power of the magnetorquer is determined by equation (4.5).

$$P_{total} = P_{wire} + P_h \tag{4.5}$$

4.3. Optimization

In this section, the magnetorquer will be optimized for the SHAPE mission such that it will meet the requirements. The most important requirements for optimizing the size of the magnetorquer are the magnetic dipole moment and maximum dimensions. The optimization will minimize the mass of the magnetorquer. There are two iterations since the second iteration on the hysteresis curve added optional materials and changed the curves slightly.

4.3.1. First Iteration

For the optimization a constraint minimization will be performed. The design parameters are on the length, wire diameter, core diameter, current, and number of layers of wire. The constraints are on the current, power, magnetic dipole moment, magnetic field, and dimensions. The minimization is as follows:

$$
\begin{aligned}
\min_{l,d_{wire},d_i,I_{in},nN} \quad & Mass(l, d_{wire}, d_i, I_{in}, nN) \\
\text{Subject to:} \quad & I_{in}/I_{max_{wire}} - 1 \leq 0 \\
& P_{use}/P_{req} - 1 \leq 0 \\
& m_{req}/m_{use} - 1 \leq 0 \\
& H_{use}/H_{allowed} - 1 \leq 0 \\
& 10 \cdot 10^{-3} \leq l \leq 100 \cdot 10^{-3} \\
& 0.07874 \cdot 10^{-3} \leq d_{wire} \leq 0.5 \cdot 10^{-3} \\
& 5 \cdot 10^{-3} \leq d_i \leq 50 \cdot 10^{-3} \\
& 1 \cdot 10^{-5} \leq I_{in} \leq 0.1 \\
& 1 \leq nN \leq 2
\end{aligned}
$$

Where $Mass$ is the total mass of the magnetorquer, l is the length of the magnetorquer, d_{wire} is the wire diameter, d_i is the inner diameter (core diameter) of the magnetorquer, nN is the number of layers of wire. The wire diameter determines the maximum current, $I_{max_{wire}}$, that can be used for a certain wire diameter. The current, I_{in}, is a design parameter. P_{use} is the power when I_{in} is used, P_{req} is the maximum power defined by the requirements. m_{req} is the peak dipole moment from the requirements, m_{use} is the dipole moment that is generated by the design parameters. H_{use} is the magnetic field that is generated with the design parameters, $H_{allowed}$ is the maximum magnetic field allowed to stay in a good region in the hysteresis curve.

The optimization is done by the MATLAB function *fmincon*. The algorithm was set to 'active-set', the optimization results can be found in table 4.5, with the initial guess given in table 4.4. All the results are local minimums, so there are other solutions possible.

Table 4.4: Initial guess of the magnetorquer size to start the optimization

Design parameter	l [m]	d_{wire} [m]	d_i [m]	I_{in} [A]	nN [-]	Mass [kg]
Value	0.074	$8 \cdot 10^{-5}$	0.0057	0.001	1	0.0161

Table 4.5: Optimized magnetorquer size for one layer of wire

Material	l [mm]	d_{wire} [mm]	d_i [mm]	I_{in} [mA]	nN [-]	Mass [g]	Volume [cm^3]
45 Permalloy	18.7	0.07874	9.59	2.44	1	11.3	1.397
78 Permalloy	13.7	0.1018	11.2	2.29	1	12.0	1.408
4-79 Mo-Permalloy	42.9	0.07874	6.4	0.7	1	12.5	1.460

4.3.2. Second Iteration

After the second iteration on the hysteresis curve, a new size optimization is required since the curves are available for more materials now and some of the curves changed slightly. With this, the process described above for the size optimization stays the about the same. The boundary for the maximum length of the magnetorquer was changed from 100 mm to 80 mm. The dimensions of the CubeSat are 100 x 100 x 300 mm so the maximum length of the magnetorquer has to be less than 100 mm to fit in the CubeSat. Further, some crucial mistakes in the MATLAB code have been solved, which explained the slightly unrealistic sizes from the first iteration. One other note, the results from the optimization are in ideal circumstances, like a solenoid with windings perfectly tight next to each other.

Knowing this, only the results of the new size optimizations are shown in table 4.6. The column with $nN[-]$ has been left out, since this was 1 for all the materials, and a column with the power is added. As can be seen in table 4.6 the power of all magnetorquers is extremely low compared to magnetorquers that are available right now. A magnetorquer from Hyperion that generates a nominal dipole moment of 0.5 Am^2 has a power consumption of 270 mW (*MTQ400*, 2018). This is a much higher number than the designed magnetorquers, so the power consumption results are unreliable. Considering the values might be wrong, the consumption relative to each other will most likely not change.

Table 4.6: Optimized magnetorquer size for one layer of wire using the second iteration hysteresis curves

Material	l [mm]	d_{wire} [mm]	d_i [mm]	I_{in} [mA]	Mass [g]	Volume [cm^3]	Power [mW]
4% Silicon Iron	48.1	0.0788	5.0	8.1	7.6	1.00883	2.9
45 Permalloy	30.2	0.0862	11.1	4.3	24.5	3.0186	0.7819
Hipernik	50.1	0.2382	32.5	0.38	350	42.723	0.0012735
78 Permalloy	15.5	0.1787	12.3	3.8	16.5	1.9545	0.048469
4-79 Mo-Permalloy	14.2	0.4631	12.9	4.0	18.1	2.1642	0.0102166
Supermalloy	11.0	0.1276	15.7	0.60	19.1	2.1982	0.0038175

4.4. Sensitivity Analysis

In this section, a sensitivity analysis will be done on the final magnetorquer model. This analysis will show what the influence is from the design parameters on the generated dipole moment, power, mass, and volume. For this analysis, the optimized models for the different materials will be used and the design parameters varied one by one by a certain percentage. The percentages will be -10%, -5%, 0%, +5%, +10%. Next, there will be a thermal analysis for the operating temperature range found in section 4.1.3.

The first design parameter to be varied is the magnetorquer length, then the wire diameter, followed by the core diameter, and the current. The number of layers of wire will not be varied since this will always be a round number. In section 4.4.1 the result of the first iteration materials are shown, and in section 4.4.2 the second iteration results. A short general analysis follows below.

Sensitivity with Magnetorquer Length

If the magnetorquer length increases then the mass, volume, magnetic dipole moment, and power increase as well. For mass and volume, there is a direct relation between them. For the magnetic dipole moment, an increase in length means a longer wire that generates a higher magnetic field and thus a higher magnetic dipole moment; however, this also means a higher volume, which results in a higher magnetic dipole moment, as well. For the power, an increase in length means a longer wire which means an increase in resistance, and an increase in power.

Sensitivity with Wire Diameter

An increase in wire diameter means a increase mass and volume, and a decrease in the magnetic dipole moment and power. For the magnetic dipole moment, an increase of the wire diameter means a decrease in the number of loops in the solenoid, which will generate a lower magnetic field and thus a lower dipole moment. For the power, an increase in wire diameter means a lower resistance, so a decrease in power, since the power is proportional to $\frac{1}{r^2}$.

Sensitivity with Core Diameter

If the core diameter is increased, then the mass, volume, magnetic dipole moment, and power will increase. For mass and volume the relation is clear. For the magnetic dipole moment, and increase in core diameter means a larger solenoid which will generate a higher magnetic field, and a larger volume, which both will increase the magnetic dipole moment. For the power an increase in core diameter means a longer wire, which means a higher resistance and thus an increase in power.

Sensitivity with Current

The change in current does not influence the mass and volume of the magnetorquer. An increase in current means an increase in magnetic dipole moment and power. For the magnetic dipole moment, an increase in current means a higher magnetic field is generated by the solenoid, so the magnetic dipole moment will increase. For the power, an increase in current obviously increases the power, since the power is proportional to I^2.

4.4.1. First Iteration

In figures 4.1 to 4.4 the sensitivity of the design parameters on the mass, volume, magnetic dipole moment, and power is shown for the first iteration materials.

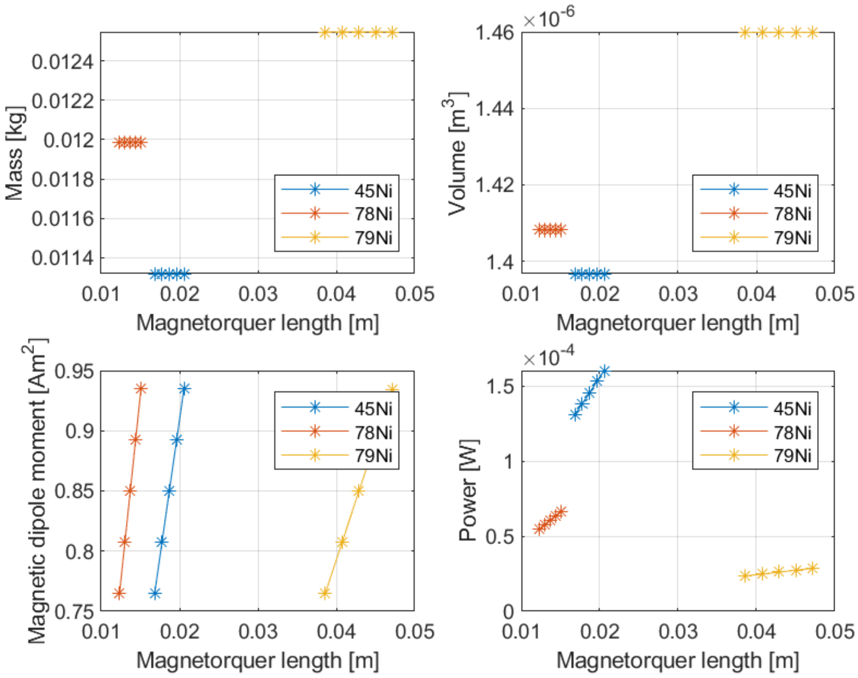

Figure 4.1: Sensitivity with the magnetorquer length

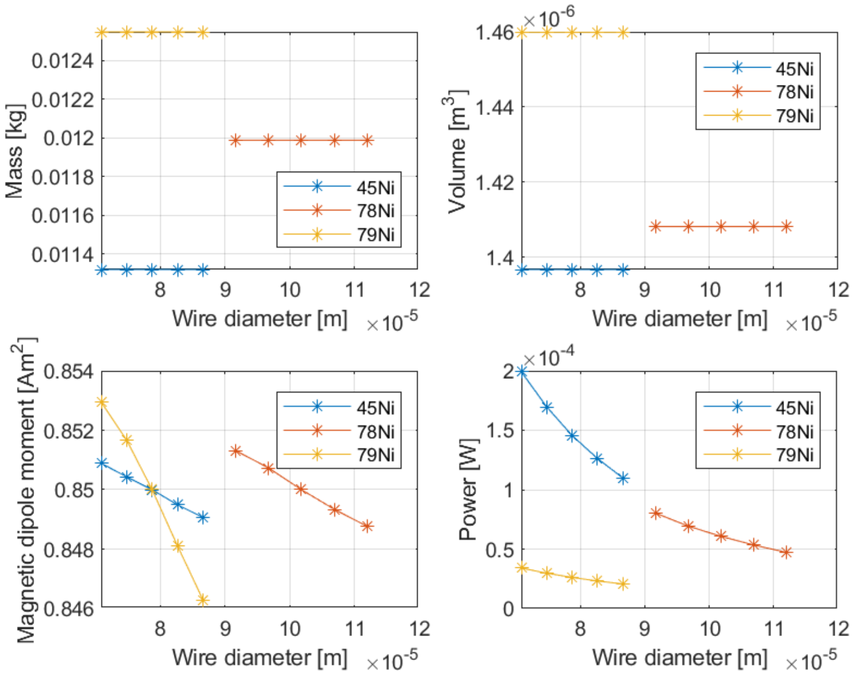

Figure 4.2: Sensitivity with the wire diameter

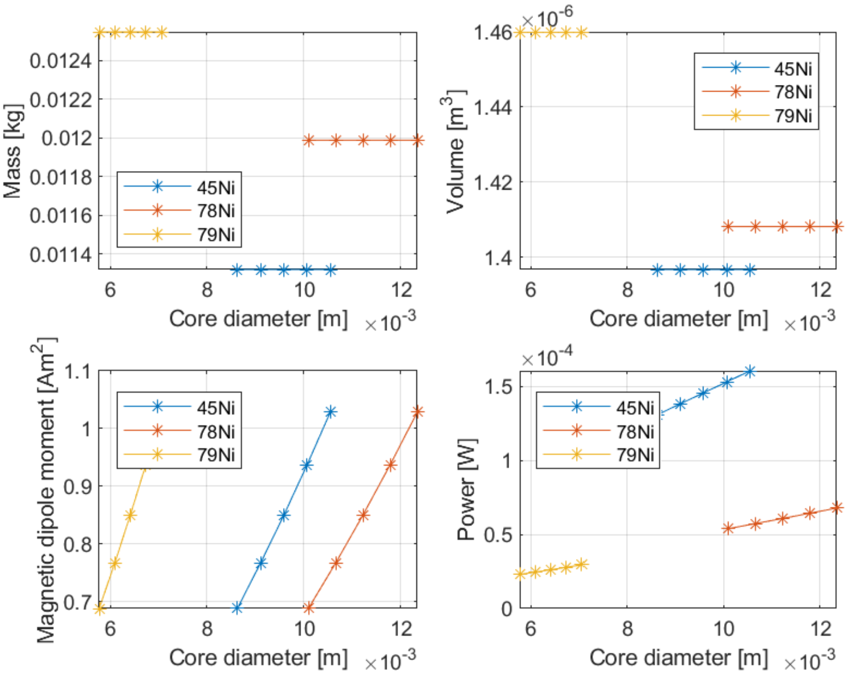

Figure 4.3: Sensitivity with the core diameter

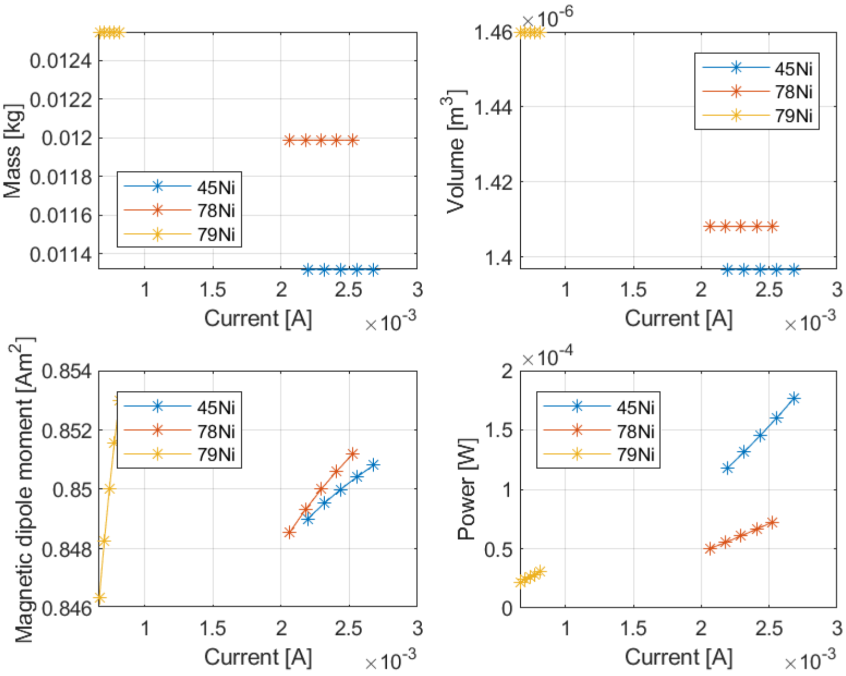

Figure 4.4: Sensitivity with the current

Thermal sensitivity

The thermal sensitivity of the magnetorquer is mainly due to the resistance of the wire that changes with temperature. So, this means the power used by the magnetorquer and the maximum allowed current through the wire varies with temperature. In figure 4.5, the sensitivity of the magnetorquer with temperature is shown, and both the power and maximum allowed current through the wire are plotted. As can be seen, in a lower operating temperature the power used will be less, for the same used current and generated magnetic dipole moment. Also, if the initial power usage is lower, it seems less sensitive to temperature than higher amounts of power. In the plot with the current, the solid line represents the maximum allowed current through the wire, and the dashed lines represent the current needed from the optimization. The needed current never exceeds the maximum allowed current through the wire, as can be seen in the figure.

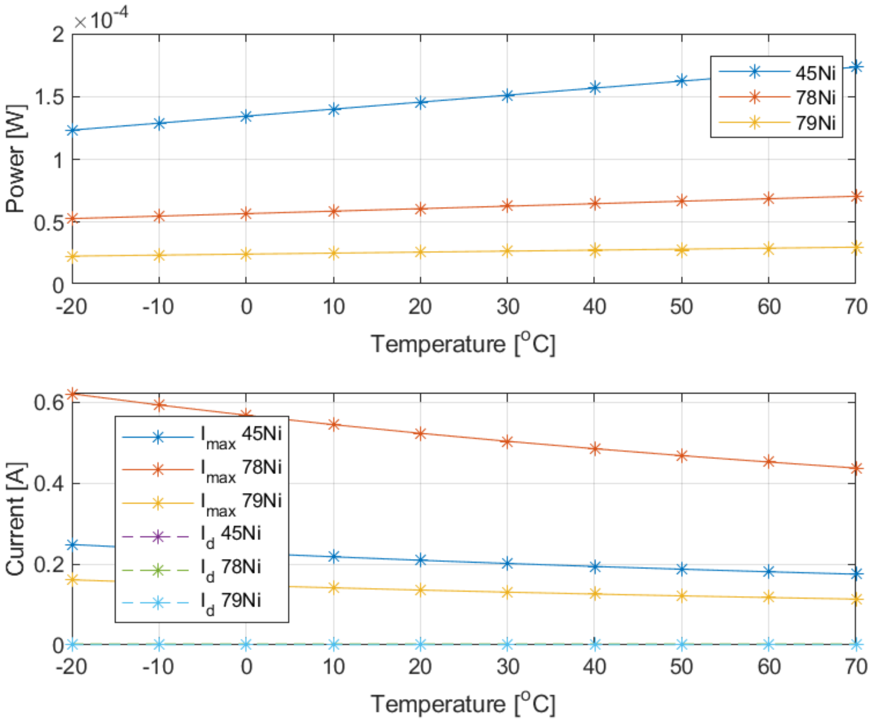

Figure 4.5: Sensitivity of power and current with temperature. In current plot, solid line is maximum allowed current through wire, and dashed line is the current needed from the optimization.

The thermal coefficient of the wire has some uncertainties as well, see table 4.3. The previous analyses were done with the nominal value, the following analysis will be done to show the sensitivity to a different thermal coefficient. In figure 4.6 the sensitivity of the thermal coefficient is shown for the temperature range, since the effect of the thermal coefficient is related to the temperature difference between the temperature of the wire and the ambient temperature (see equation (4.2)). As can be seen in the figures, the differences between the minimum and maximum value of the thermal coefficient over the temperature range are very small. The maximum difference in figure 4.6 is 1.6% for 45 Permalloy. This means that a slightly different value for the thermal coefficient will not significantly affect the magnetorquer performances.

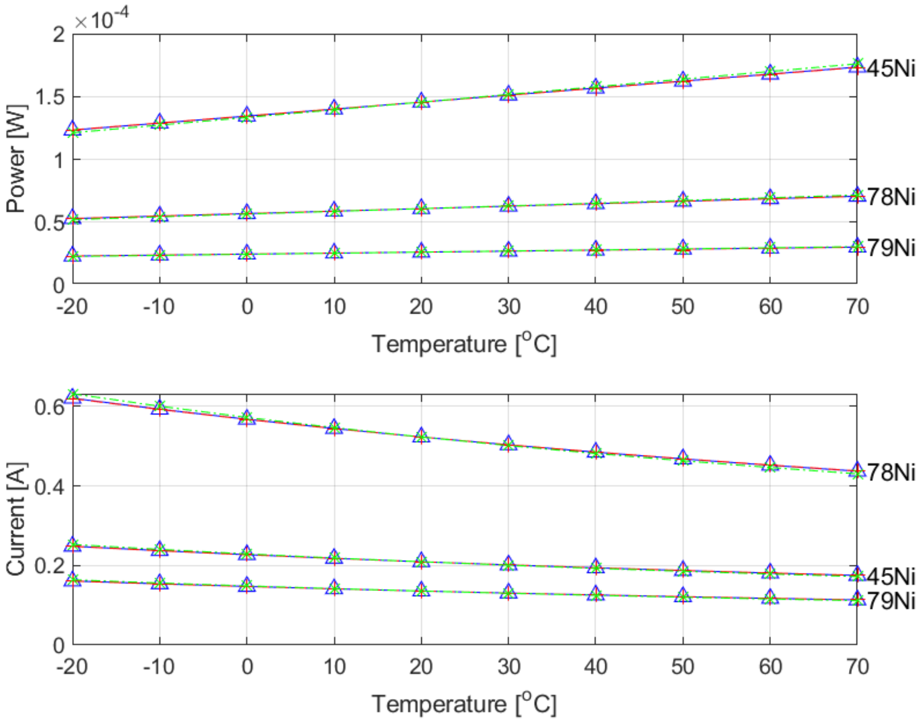

Figure 4.6: Sensitivity of power and current with temperature and thermal coefficient. The blue solid line with triangles is the nominal value, the red dashed line with pluses is the minimum value, and the green dash-dot line with crosses is the maximum value for the thermal coefficient.

4.4.2. Second Iteration

After the second iteration on the hysteresis curve, a new size optimization has been performed, so a second iteration of the sensitivity analysis is done. This is done the same way as before, but with all the materials from the second iteration. The results are shown in figures 4.8 to 4.10 and 4.12.

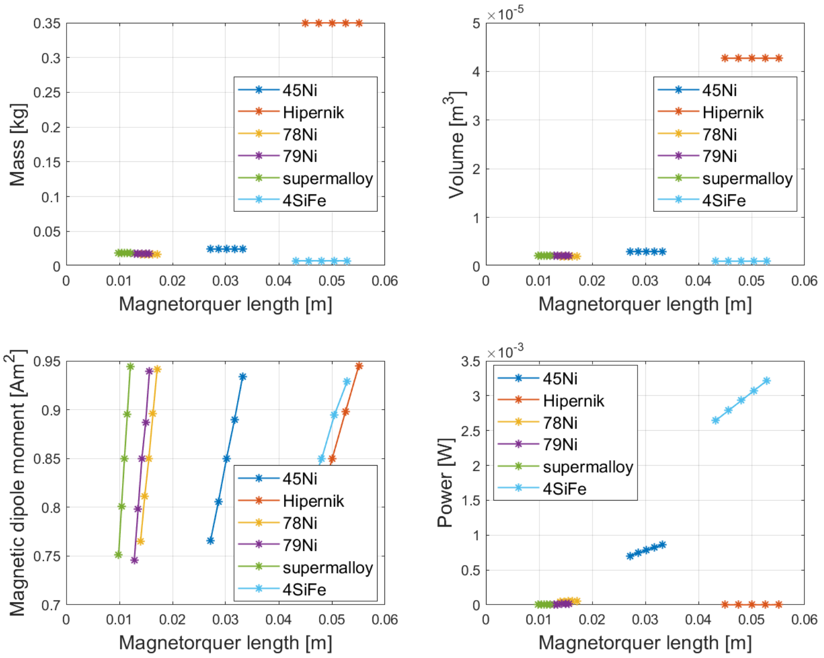

Figure 4.7: Sensitivity with the magnetorquer length

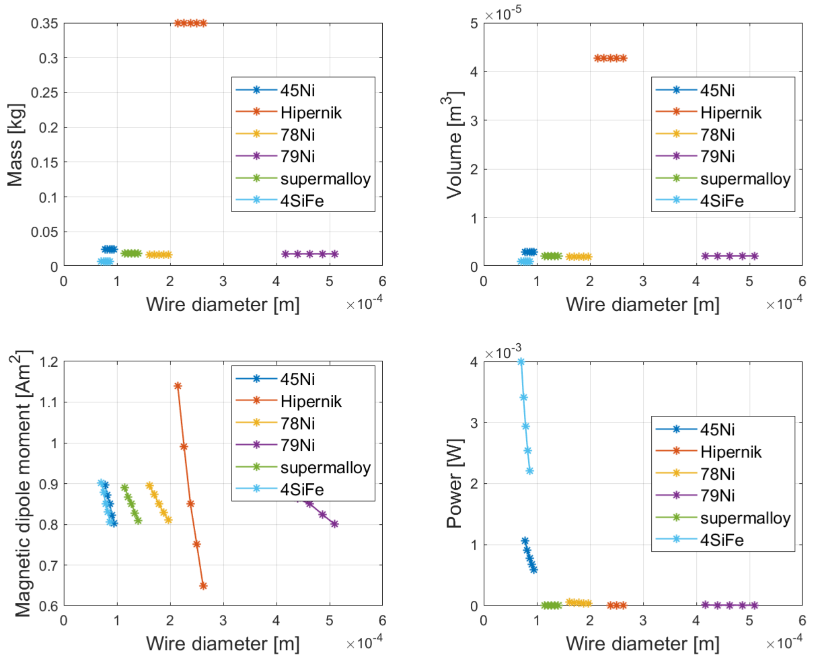

Figure 4.8: Sensitivity with the wire diameter

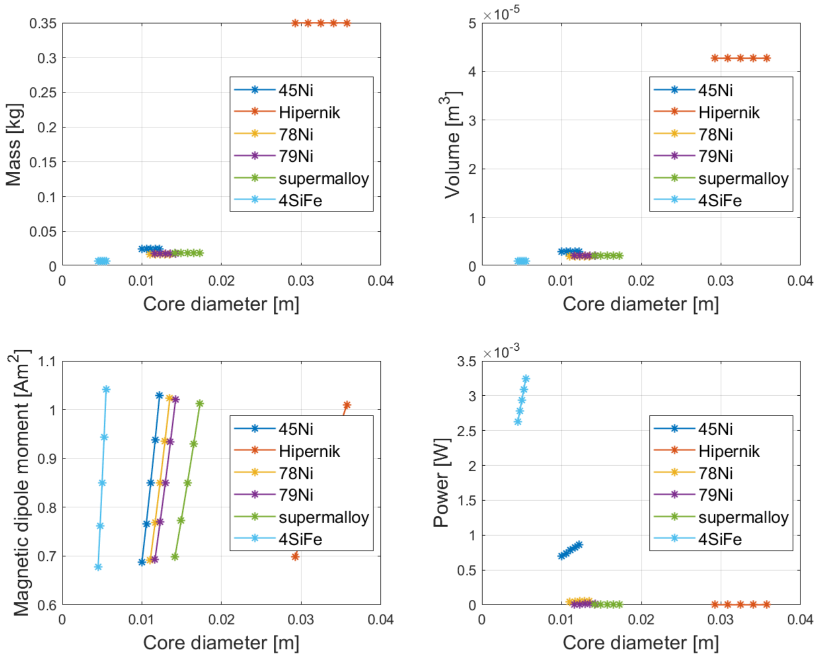

Figure 4.9: Sensitivity with the core diameter

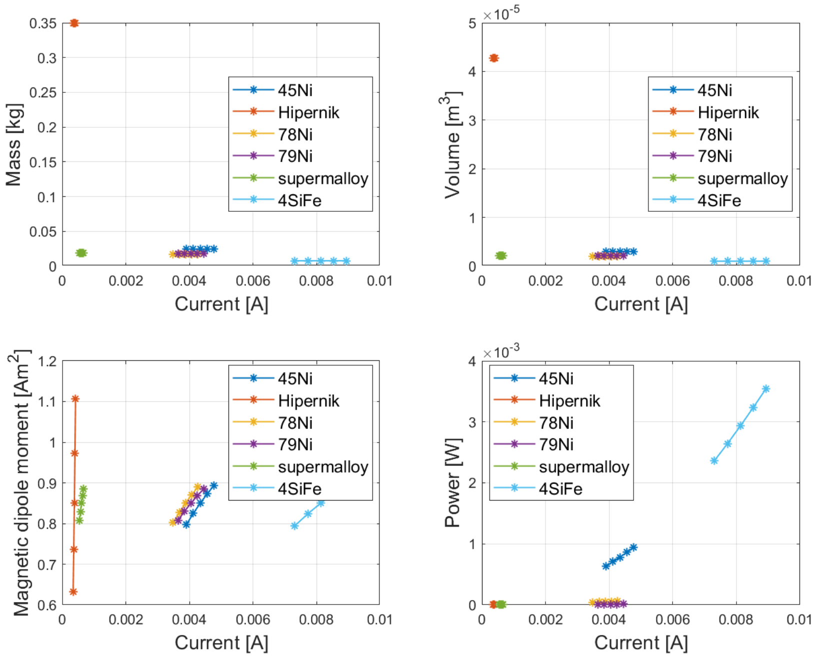

Figure 4.10: Sensitivity with the current

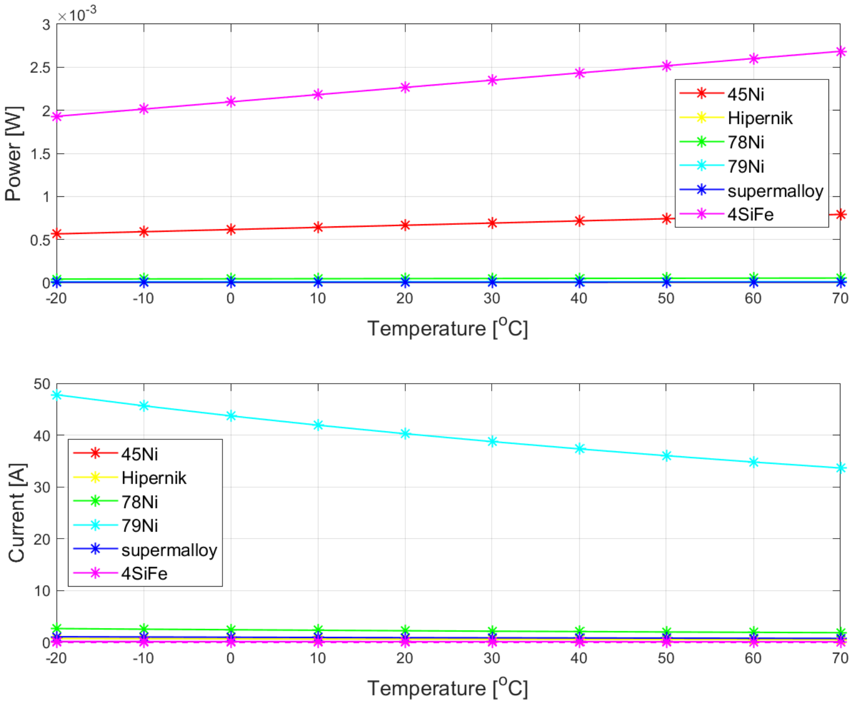

Figure 4.11: Sensitivity of power and current with temperature. In current plot, solid line is maximum allowed current through wire, and dashed line is the current needed from the optimization.

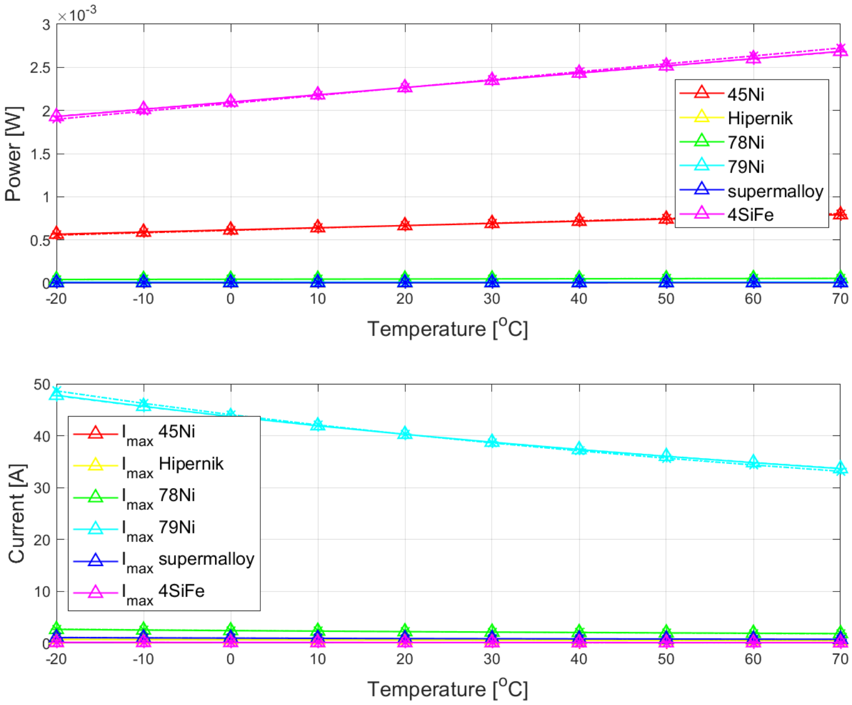

Figure 4.12: Sensitivity of power and current with temperature and thermal coefficient. The solid line with triangles is the nominal value, the dashed line with pluses is the minimum value, and the dash-dot line with crosses is the maximum value for the thermal coefficient.

4.5. Final Magnetorquer

The final magnetorquer will be chosen from the results presented in the optimization and sensitivity analysis. Table 4.5 and table 4.6 and the graphs of the sensitivity analysis show which magnetorquer is the lightest, smallest, and uses the least amount of power, for both the first iteration and second iteration. The final magnetorquer will be chosen from the second iteration.

4.5.1. First Iteration

The lightest magnetorquer has a core made of 45 Permalloy, this has the smallest volume as well. The least power is used by the magnetorquer with a core of 4-79 Mo-Permalloy.

Figure 4.13 show the different materials when plotted mass against power and volume against power. The values are normalized to the lightest material (45 Permalloy) such that a good comparison can be made. From these figures, the optimal material would be 4-79 Mo-Permalloy (79Ni in the figures) since this one has the shortest distance to the origin, so the balance between mass/volume and power is the best.

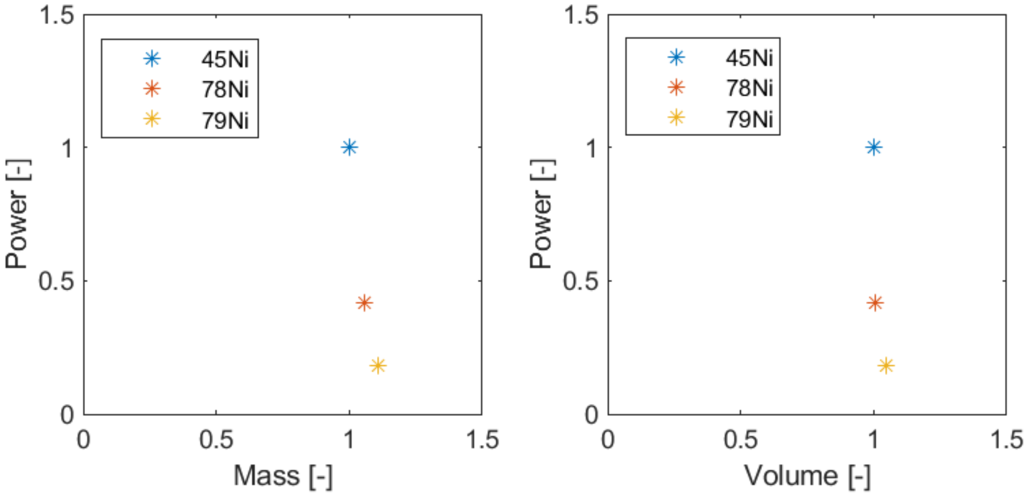

Figure 4.13: Mass against power and volume against power, normalized to 45 Permalloy, to find the best core material

So, if the lightest and smallest magnetorquer is preferred, than a magnetorquer with a 45 Permalloy (45Ni) core is the best. If power is the driving requirement then 4-79 Mo-Permalloy (79Ni) is the best option. If both have to be minimized, 4-79 Mo-Permalloy is the best option. All options meet the requirements, but 4-79 Mo-Permalloy is chosen as the best core material for this application.

4.5.2. Second Iteration

More materials were available after the second iteration of the hysteresis curve. The results from the second iteration of the size optimization gave different results, and with these extra materials, an other material might be better than the one found previously. In figure 4.14 on the left, the materials are plotted with their mass against their power. According to this figure, the best balanced materials are 78 Permalloy (78Ni), 4-79 Mo-Permalloy (79Ni), and Supermalloy. Zooming in on these materials give the figure on the right. Here, it shows that 4-79 Mo-Permalloy (79Ni) is the best balanced material. If the lightest material is required, the best choice is 4% Silicon Iron (4SiFe). If the least power consuming material is needed, the best choice would be Hipernik. Although, Hipernik has a very high mass, so a better choice for low power is Supermalloy. The recommended material is 4-79 Mo-Permalloy, which is the same as in the first iteration even after all alterations. The final magnetorquer with a 4-79 Mo-Permalloy core will have the following dimensions: 14.2 mm in length and 12.9 mm in diameter, and will have a mass of 18.1 g.

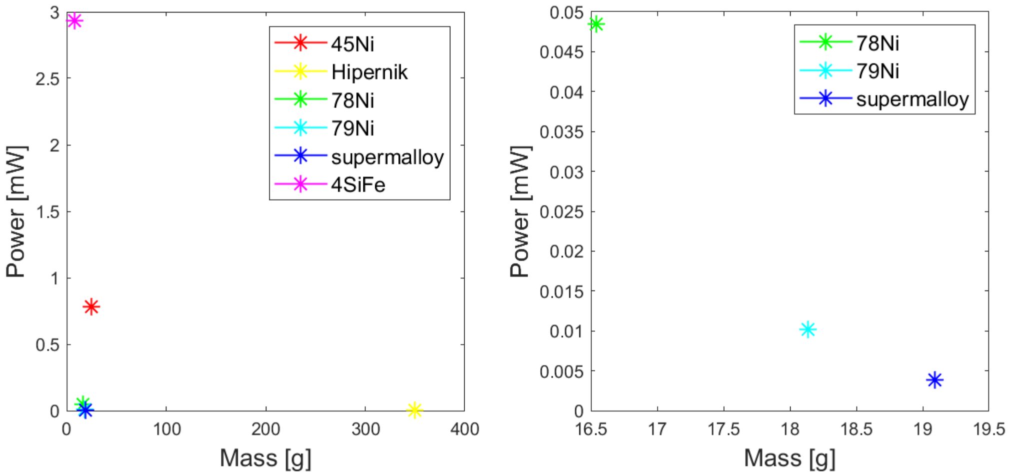

Figure 4.14: Mass against power to find the best core material for the second iteration. On the left, all materials. On right, zoomed in on the best balanced materials.

5

Orbital Details

In this chapter, the orbital details for the SHAPE mission will be discussed. First, the orbit and orbital position of the spacecraft has to be know. Once the orbital position is know, the geomagnetic field vector for the position can be found, which will be used later in the control loop. There are multiple reference frames used in this chapter so these will be explained first in section 5.1. The orbital model will be described in section 5.2, and the geomagnetic field in section 5.3.

5.1. Reference Frames

Calculations for spacecraft often use different reference frames. Here the reference frames that will be used in this thesis will be briefly explained.

ECI Earth-Centered Inertial Reference Frame; The origin is at the center of mass of the Earth, the XY-plane is the equatorial plane. The positive X-axis is pointed to the vernal equinox, Υ, the positive Z-axis is pointed the north pole, and the Y-axis completes the right-handed system.

ECEF Earth-Centered, Earth-Fixed Reference Frame; The origin is at the geographic center of the Earth, the XY-plane is the the equatorial. The X-axis is pointed to the crossing of the equator and the prime meridian in Greenwich. Here the 0° latitude and 0° longitude are defined. The Z-axis is pointed in the direction of 90° latitude and 0° longitude, and the Y-axis completes the right-handed system.

LLA Latitude, Longitude, and Altitude geodetic coordinates, are a special case in the ECEF reference frame. Instead of x, y, and z, here the coordinates are expressed in latitude, longitude, and altitude.

LVLH Local Vertical Local Horizontal, an orbital reference frame with the origin in the center of mass of the spacecraft. The x-axis points in the direction of flight, the z-axis in the nadir direction (towards Earth), and the y-axis completes the right-handed system, perpendicular to the orbital plane.

Body Reference frame of the spacecraft, with the origin in the center of mass of the spacecraft, and the axis are aligned with the principal axes of the spacecraft.

Table 5.1: Conversion function in MATLAB between Reference Frames

Reference Frames	MATLAB function
ECI → ECEF	$dcm = dcmeci2ecef('IAU-2000/2006', [year, month, day, hour, minutes, seconds])$, $xyz_{ECEF} = dcm \cdot xyz_{ECI}$
ECI → LLA	$lla = eci2lla([x, y, z], [year, month, day, hour, minutes, seconds])$

5.2. Orbital Model

The orbital position of the spacecraft is important for the simulation of the attitude control with magnetorquers, since the magnetorquers interact with the geomagnetic field to generate the actuation torque. The geomagnetic field is different on any orbital position, so it is important to simulate the orbit of the spacecraft and find the magnetic field vectors on each position. The disturbances that are experienced in the orbit are of importance for the attitude control of the spacecraft, since these will disturb the desired attitude.

5.2.1. Basic Orbital Model

A first basic orbit simulation is made in the Earth-Centered Inertial Reference Frame (ECI). The x, y, and z position of the spacecraft can be determined by equation (5.1) (Montenbruck and Gill, 2001).

$$\begin{pmatrix} x \\ y \\ z \end{pmatrix} = r \begin{pmatrix} \cos u \cos \Omega - \sin u \cos i \sin \Omega \\ \cos u \sin \Omega + \sin u \cos i \cos \Omega \\ \sin u \sin i \end{pmatrix} \tag{5.1}$$

With $u = \omega + v$ the argument of latitude, ω is the argument of perigee, v is the true anomaly, r is the radial distance, Ω is the right ascension of ascending node (RAAN), and i is the inclination of the orbit.

The orbit of SHAPE is a noon-midnight SSO, with a start altitude of 380km. The orbit is assumed to be circular. The radial distance, r, in the equations above will therefore be the semi-major axis, a, of the orbit, which is the altitude plus the mean radius of the Earth. The inclination of the orbit is about 97°, and the RAAN is dependent on the start date and time.

To propagate the initial position in time, the mean anomaly will be propagated in time with equation (5.2) (Montenbruck and Gill, 2001). Where the initial value is denoted as M_0, n is the mean motion, μ is the gravitational parameter of Earth, and t is the propagation time. The mean anomaly will be assumed to be the same as the true anomaly for use in equation (5.1).

$$M = M_0 + n \cdot t \qquad\qquad n = \sqrt{\frac{\mu}{a^3}} \tag{5.2}$$

5.2.2. Atmospheric Drag

Due to the low orbit, the atmospheric drag is the largest contributor to orbital decay. The density of the atmosphere however is effected greatly by the solar activity. The density can be estimated by using the 2001 United States Naval Research Laboratory Mass Spectrometer and Incoherent Scatter Radar Exosphere (NRLMSISE00) model (Picone et al., 2002). MATLAB has a function that uses this model, called *atmosnrlmsise00*, which will be used to determine the total mass density for the orbit model. This function requires to input the 10.7cm solar radio flux data and the magnetic activity index, which are available at the National Centers for Environmental Information (NCEI) for Environmental Information (n.d.). The code that will be used for retrieving this data and computing the averages is written by Ju (2017). This code will retrieve data from the archive that runs from 1932 till 2017. For data from 2017 till 2030, predicted data is available, which can be retrieved from the NCEI. This data is predicted per month. To have it per day, the data will be interpolated with a spline interpolation, like Ju (2017) did. The predicted data is available in three percentile levels, 5%, 50%, and 95%.

The 95% percentile will be used for the calculation, since this will represent the worst case. Once the density is found the change in semi-major axis can be determined by using equation (5.3) (Larson and Wertz, 1999), which is the change per revolution, and where C_D is the drag coefficient, which is assumed to be $C_D = 2.2$ (Larson and Wertz, 1999), A is the cross-sectional area, ρ is the total mass density of the atmosphere, a is the semi-major axis, and m is the total mass of the spacecraft.

$$\Delta a_{rev} = \frac{-2\pi C_D A \rho a^2}{m} \tag{5.3}$$

5.2.3. J2 Effect

The Earth is not a perfect sphere, but slightly flattened with a bulge at the equator. This flattening has an effect on the orbit, namely on the RAAN and argument of perigee. Since a circular orbit is assumed, the argument of perigee is assumed to be constant as well. The change in the RAAN will be determined by equation (5.4) (Larson and Wertz, 1999), where J_2 is the J2 effect parameter, $J_2 = 0.00108263$, and R_e is the equatorial radius of Earth, $R_e = 6378.137$km.

$$\dot{\Omega} = -1.5nJ_2\left(\frac{R_e}{a}\right)^2 \cos i\left(1-e^2\right)^{-2} = -1.5nJ_2\left(\frac{Re}{a}\right)^2 \cos i,\ \text{since}\ e=0 \tag{5.4}$$

5.2.4. Final Orbit Model

The final orbit model consists of the basic model plus the atmospheric drag and J2 effect, since these are the main disturbances on the very low Earth orbit. This model can predict the orbit from 1932 until 2030, given any start date and time in this period of time. It will propagate until the spacecraft is below an altitude of 230km and give the time it will take to reach that from the original altitude, in this case 380km. Or, if preferred, it can propagate for a certain time or number of orbits.

5.3. Geomagnetic Field

The geomagnetic field is the magnetic field generated by the Earth. This field will be used to orientate the spacecraft with the magnetorquers. The magnetorquers will "push off" of this field to generate the torque to re-orientate the spacecraft. For simulations, the value of the geomagnetic field can be found via a MATLAB function. This will be further discussed in section 5.3.1. The values of the geomagnetic field are dependent on the orbit of the spacecraft, so in section 5.3.2, a short analysis is done to see how much it will change if one of the orbital parameters changes slightly.

5.3.1. MATLAB function *igrfmagm*

The geomagnetic field at each orbital position can be determined by the MATLAB function *igrfmagm*. This function uses the International Geomagnetic Reference Field (IGRF) 12th generation model from International Association of Geomagnetism and Aeronomy (IAGA) (Thébault et al., 2015; NOAA, 2010) and asks for the location and time stamp as inputs. The location has to be entered in latitude, longitude, and altitude. The time has to be entered in decimal year. The output is a the magnetic field vector, with an overall uncertainty in the geomagnetic field of about 10 nT rms (NOAA, 2010).

The determination of the geomagnetic field will work together with the orbit model presented in section 5.2. Figure 5.1 shows two orbits with the geomagnetic field vectors on some orbital positions with the starting point on the equator at the first of January 2018, at 11:00:00.

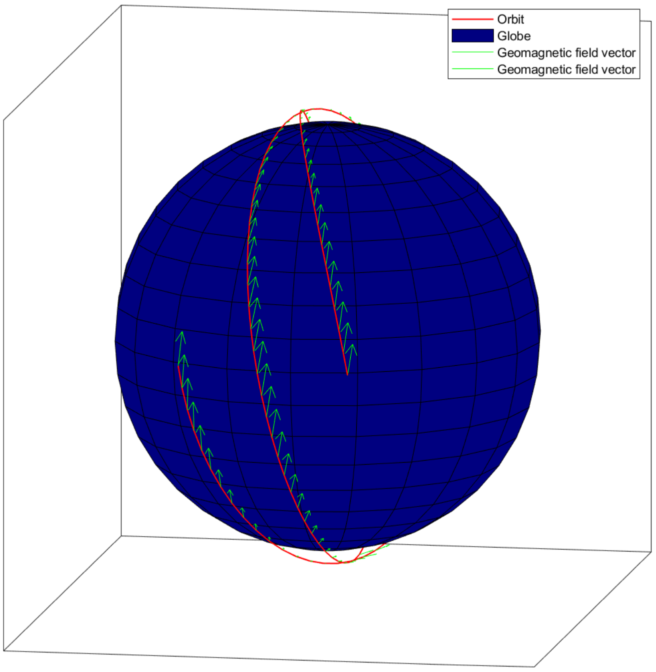

Figure 5.1: Two orbits with geomagnetic field vectors, starting on the equator at the first of January 2018, at 11:00:00.00.

5.3.2. Sensitivity of the Geomagnetic Field with Changes in Orbital Parameters

The initial orbital parameters are mentioned earlier in section 5.2, but an overview is given in table 5.2. These parameters can be slightly altered to find out how much the geomagnetic field will change over the course of a few orbits (two in this case).

Table 5.2: Initial Orbital Parameters for SHAPE. h is altitude, i is inclination, e is eccentricity, ω is argument of perigee, ν is true anomaly, and Ω is right ascension of ascending node.

h [km]	i [°]	e [-]	ω [°]	ν [°]	Ω [°]
380	97	0	0	0.0209	100.8

The altitude will be changed by 10 km, the inclination, argument of perigee, and RAAN by 1°, both positive and negative. The true anomaly was left out of this analysis since the argument of perigee and the true anomaly are added to form the argument of latitude used in equation (5.1), and contribute equally, so they will produce the exact same results.

For every change, the maximum absolute difference over two orbits is given in table 5.3 for the x, y, and z components of the geomagnetic field, together with what percentage that is from the original magnetic field on that position. A few figures (figures 5.3 and 5.4 are included that show how the orbit changes with a change in one orbital parameter.

Table 5.3: Maximum absolute differences in the x, y, and z components of the geomagnetic field, between the original orbit and the altered one.

Parameter	x [nT]	y [nT]	z [nT]	x [%]	y [%]	z [%]
$h + 10\text{km}$	148.1	73.86	242.7	0.5246	0.5880	0.4575
$h - 10\text{km}$	149.2	74.43	244.2	0.5284	0.5925	0.4604
$i + 1°$	$1.165 \cdot 10^3$	645.5	416.6	50.16	15.21	0.8452
$i - 1°$	$1.295 \cdot 10^3$	820.3	401.6	57.03	19.33	0.8147
$\omega + 1°$	$1.690 \cdot 10^3$	$1.078 \cdot 10^3$	$1.243 \cdot 10^3$	35.67	25.41	17.58
$\omega - 1°$	$1.704 \cdot 10^3$	$1.043 \cdot 10^3$	$1.240 \cdot 10^3$	35.97	9.651	17.54
$\Omega + 1°$	210.6	197.1	245.8	4.446	4.642	1.640
$\Omega - 1°$	211.4	196.0	252.2	4.462	4.618	1.683

In table 5.3, the largest absolute differences appear in the argument of perigee. These largest differences are around the south pole. But the z-component has some big differences around the equator, as shown in figure 5.2a.

The largest percentage difference appears in the inclination. For the inclination the largest difference is at the south pole, as well, as can be seen in figure 5.2b. This is the place where the orbit deviates the most from the original orbit, so a larger deviation in geomagnetic field is expected. A larger difference is expected at the north pole as well, but the difference here is smaller than at the south pole.

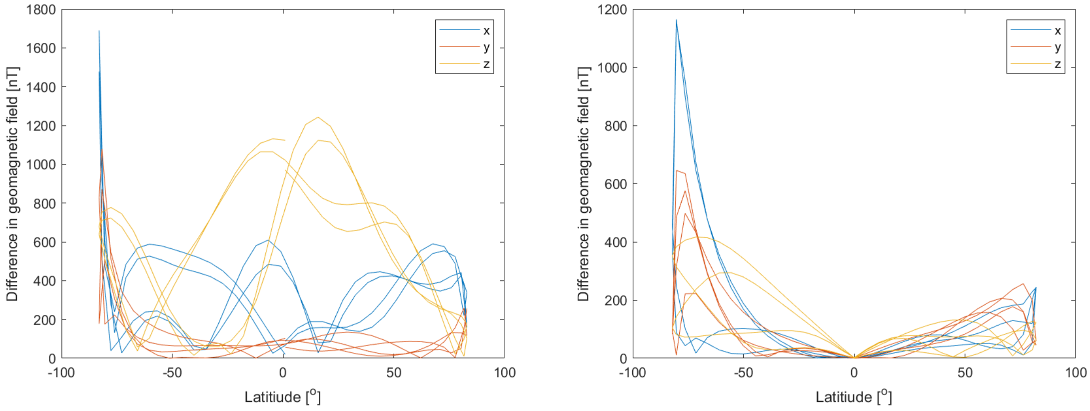

(a) Difference in geomagnetic field for an increased argument of perigee.

(b) Difference in geomagnetic field for an increased inclination.

Figure 5.2: Difference in geomagnetic field over two orbits for increased inclination and increased argument of perigee, both by 1°.

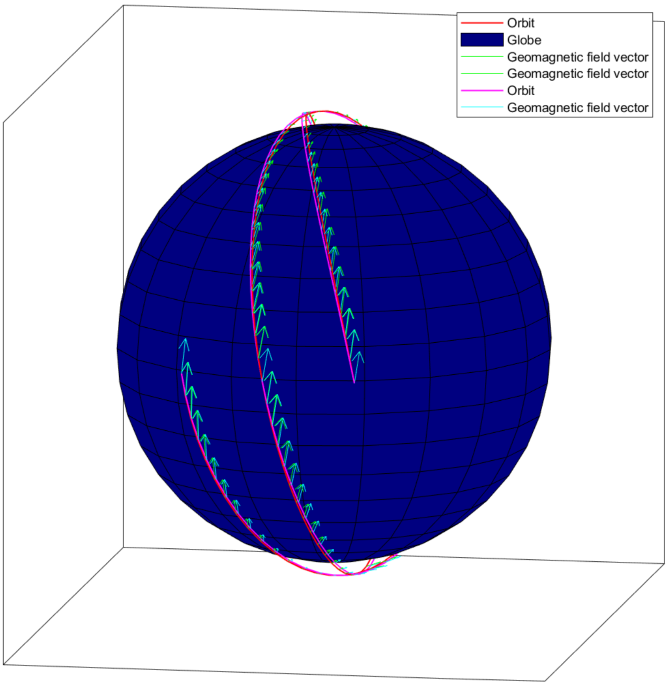

Figure 5.3: Two orbits with geomagnetic field vectors. The red line with green arrows is the original, the magenta line with cyan arrows is altered by increasing the inclination by 1°. With as start date the first of January 2018, at 11:00:00.

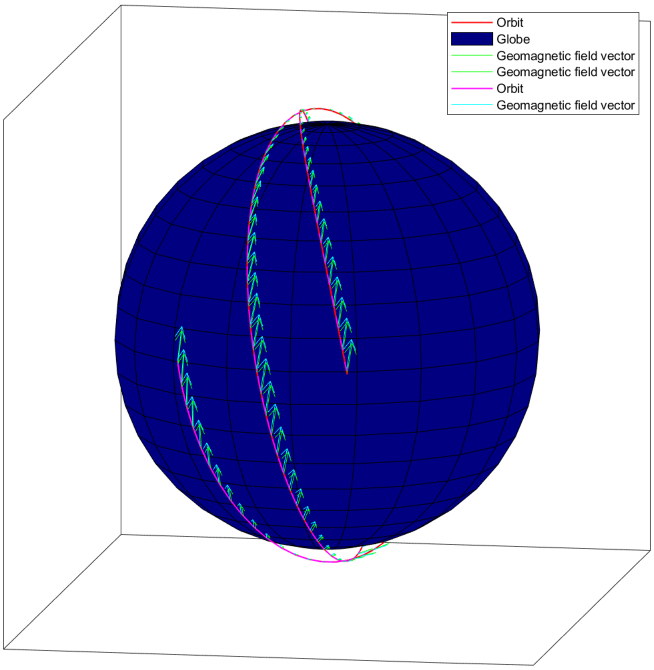

Figure 5.4: Two orbits with geomagnetic field vectors. The red line with green arrows is the original, the magenta line with cyan arrows is altered by decreasing the argument of perigee by 1°. With as start date the first of January 2018, at 11:00:00.

5.3.3. Polar Substorms

At higher latitudes the geomagnetic field becomes more unstable. This is due to the connection of the upper polar atmosphere and the outer magnetosphere by the geomagnetic field lines. There appears to be an almost continuous acceleration of charged particles near the boundary of the inner and outer magnetosphere (Akasofu, 1968). Some of these particles are able to penetrate deep into the polar upper atmosphere and interact with the atoms and molecules. This interaction can cause various phenomena.

Magentospheric storms and substorms can be caused by intense solar flares. During a solar flare, a solar plasma cloud is ejected and generates a shock wave in interplanetary plasma. When the shock wave and plasma cloud interact with the magnetosphere, it begins a magnetospheric storm. This storm is marked by the sudden compression of the magnetosphere by the shock wave and high pressure region behind the shock, which is followed by successive occurrences of explosive processes within the magnetosphere. The individual explosive processes typically last for one to three hours, and are called magnetospheric substorms (Akasofu, 1968). If multiple substorms happen shortly after each other, they enforce the disturbances and it can be called a magnetospheric storm.

The geomagnetic field is disturbed by motions of the energetic particles that appear during the substorms. The main type of energetic particles are protons. The motions of these protons can generate electric currents, resulting in magnetic disturbances. The magnetosphere communicates to the ionosphere and creates electric currents there, which results in ionospheric substorms. Especially, a concentrated electric current, called an auroral electrojet, can cause intense geomagnetic disturbances (Akasofu, 1968).

These phenomena happen in the auroral oval, which spreads over latitudes from approximately 60° to 80°, depending on the time of the day. In figure 5.5 the auroral oval is shown. This oval is the zone with the highest activity, and thus disturbances. With this knowledge, the use of magnetorquers in this highly-disturbed region would not be recommended.

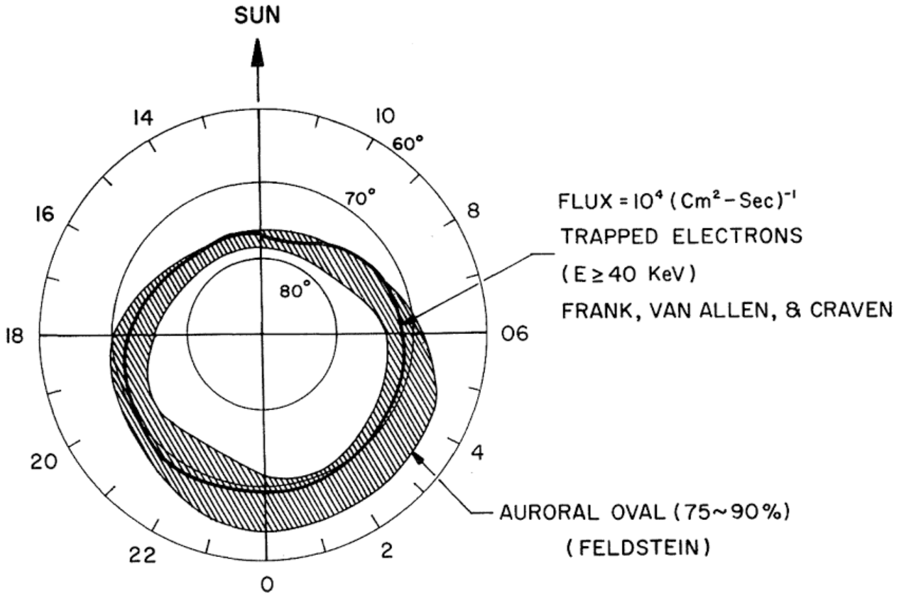

Figure 5.5: Auroral oval determined by Feldstein and the outer boundary of the trapping region (Akasofu, 1968).

6

Attitude Control Loop Model

In this chapter, the attitude control loop model with only magnetorquers next to the big momentum wheel will be discussed. First, the attitude control system will be shortly introduced in section 6.1. Then, a short literature study will be performed on existing attitude control algorithms, which use only magnetorquers, in section 6.2. Finally, the chosen control algorithm will be presented in section 6.4, including initial results with this model.

6.1. Attitude Control System

The attitude system of SHAPE consists of the huge momentum wheel and three magnetorquers. The momentum wheel will provide gyroscopic stability for two of the three axis, namely the roll and yaw axis. For the third axis (the pitch axis) the magnetorquers will be used to keep it stable. The magnetorquers are not only their for the pitch stability, but they will also be used to de-tumble the spacecraft before spinning up the momentum wheel.

6.2. Existing Magnetic Attitude Control Algorithms

Magnetic attitude control is studied since the beginning of spaceflight, but only recently more extensive research is done. Magnetic control has some challenges, since it is non-linear, time-varying, and under-actuated. Especially the under-actuation gives problems in most algorithms used for 3-axis attitude control. Several control algorithms are developed for magnetic control namely, Linear Quadratic Regulator (LQR) (Psiaki, 2001; Lovera et al., 2002; Silani and Lovera, 2005; Ju, 2017), H_2 and H_∞ (Wiśniewski and Stoustrup, 2001, 2004; Silani and Lovera, 2005), predictive control (Silani and Lovera, 2005), feedback controller (Silani and Lovera, 2005; Lovera and Astolfi, 2004; Luo and Zhou, 2017), Proportional-Derivative (PD) controller (Silani and Lovera, 2005; Torczynski et al., 2010; Sugimura et al., 2016; Xia et al., 2016), projection based (Pulecchi et al., 2010), guidance control (Miranda, 2012), nonlinear quaternion feedback law (Reyhanoglu et al., 2009), and some more. The PD controller is a commonly-used controller for 3-axis attitude control, since it is one of the least computationally-intensive control approaches, so there are PD-based controllers developed for magnetic control as well. The LQR has multiple approaches, like constant gain, infinite horizon and finite horizon, asymptotic periodic, and periodic optimal control.

In a previous thesis on the momentum wheel of SHAPE, an infinite horizon LQR approach was used for analysis (Ju, 2017). This however, due to the momentum wheel and stability requirements for the algorithm, uses several different reference frames, which require a lot of transformations that have to kept track of very carefully to make sure everything is calculated in the right reference frame. For this reason, it was decided to not use the LQR. The PD controllers found in the papers above were not reaching the 1° accuracy, so these are discarded as well. The nonlinear quaternion feedback law has shown that it can converge to values within the range of the requirements for both accuracy and stability. Others mentioned above did not provide enough information about the accuracy and stability that can be reached to consider them as a suitable algorithm. This lead to the choice of using the nonlinear quaternion feedback law as starting point for the magnetic attitude control loop.

6.3. Kinematic and Dynamic Equations

The kinematic and dynamic equation of the spacecraft are crucial for the development of a control loop. For SHAPE, these equations will be derived here, starting with the kinematic equations in section 6.3.1, followed by the dynamic equations in section 6.3.2.

6.3.1. Kinematic Differential Equation

The kinematic differential equation gives the time-dependent relative orientation of one reference frame with respect to another reference frame. The kinematic equation when using Euler angles can be found in equation (6.1), with quaternions in equation (6.2).

$$\begin{bmatrix} \dot{\theta}_1 \\ \dot{\theta}_2 \\ \dot{\theta}_3 \end{bmatrix} = \frac{1}{\cos\theta_2} \begin{bmatrix} \cos\theta_2 & \sin\theta_1 \sin\theta_2 & \cos\theta_1 \sin\theta_2 \\ 0 & \cos\theta_1 \cos\theta_2 & -\sin\theta_1 \cos\theta_2 \\ 0 & \sin\theta_1 & \cos\theta_1 \end{bmatrix} \begin{bmatrix} \omega_1 \\ \omega_2 \\ \omega_3 \end{bmatrix} \tag{6.1}$$

Where $\theta_i,\ i = 1,2,3$ are the angles between the same axes of the different reference frames, and $\omega_i,\ i = 1,2,3$ the different angular rates.

$$\dot{\mathbf{q}} = \frac{1}{2} Q_v \left(\mathbf{q}\right) \omega_r \tag{6.2}$$

with

$$\begin{aligned} \mathbf{q} &= \begin{bmatrix} q_1 & q_2 & q_3 & q_4 \end{bmatrix}^T = \begin{bmatrix} \mathbf{q}_v^T & q_4 \end{bmatrix}^T \\ \omega_r &= \omega + C\omega_o = \omega + n\mathbf{c}_y \\ Q_v &= \begin{bmatrix} q_4 \cdot I + \tilde{q}_v \\ -\mathbf{q}_v^T \end{bmatrix} \end{aligned}$$

Where q_i are the different quaternions representing the differences between the reference frames. The rotation matrix C is defined in equation (6.3).

$$C = \left(q_4^2 - \mathbf{q}_v^T \mathbf{q}_v\right) I + 2\mathbf{q}_v \mathbf{q}_v^T - 2q_4 \tilde{q}_v \tag{6.3}$$

If p is any parameter, then the skew-symmetric matrix $\tilde{p}$ is in equation (6.4).

$$\tilde{p} = \begin{bmatrix} 0 & -p_3 & p_2 \\ p_3 & 0 & -p_1 \\ -p_2 & p_1 & 0 \end{bmatrix} \tag{6.4}$$

6.3.2. Dynamic Equation

The dynamic equation is usually as in equation (6.5), but to include the gyroscopic term from the momentum wheel it becomes equation (6.6).

$$J\dot{\omega} = -\omega \times J\omega + \tau + \mathbf{T}_d \tag{6.5}$$

$$J\dot{\omega} = -\omega \times \left[J\omega + J_w v\right] + \tau + \mathbf{T}_d \tag{6.6}$$

Where J is a 3×3 matrix with the moments of inertia of the whole spacecraft, J_w is a 3×3 matrix with the moments of inertia of the momentum wheel, v is the angular velocity of the momentum wheel, τ is the control torque generated by the magnetorquers, and $\mathbf{T}_d$ contains all the disturbance torques; gravity gradient-, aerodynamic-, and residual magnetic field torque.

Moments of Inertia

The moments of inertia for both the whole spacecraft and just the momentum wheel have to be determined. The moments of inertia can be calculated as follow in equation (6.7).

$$J_x = \frac{m}{12}\left(y^2 + z^2\right) + md_x^2, \qquad J_y = \frac{m}{12}\left(x^2 + z^2\right) + md_y^2, \qquad J_z = \frac{m}{12}\left(x^2 + y^2\right) + md_z^2 \tag{6.7}$$

Where $J_i,\ i = x, y, z$ are the principal moments of inertia, m is the mass, x, y, z are the dimensions along those axes, $d_i,\ i = x, y, z$ is the perpendicular distance from the center of element to the mentioned axis.

SHAPE consists of two 3Us and the momentum wheel. The units are 30 × 10 × 10cm, the wheel has a diameter of 16cm and a thickness of 1cm, and there is 5cm between a 3U and the wheel. The total mass of the spacecraft is 8kg and the mass of the wheel is 570g (Ju, 2017). This gives the following moments of inertia matrices, shown in equation (6.8).

$$J = \begin{bmatrix} 0.095 & 0 & 0 \\ 0 & 0.064 & 0 \\ 0 & 0 & 0.145 \end{bmatrix} [\text{kg m}^2], \qquad J_w = \begin{bmatrix} 0.0012 & 0 & 0 \\ 0 & 0.0024 & 0 \\ 0 & 0 & 0.0012 \end{bmatrix} [\text{kg m}^2] \tag{6.8}$$

The principal moments of inertia in equation (6.8), are used for the development of the control loop, but for a more realistic analysis, the products of inertia should be included. The products of inertia will account for spin axis offset, the misalignment, and unequal mass distribution. It will be assumed that they are approximately 10% of the principal inertia, which will yield equation (6.9).

$$J = \begin{bmatrix} 0.095 & 0.010 & 0.006 \\ 0.010 & 0.064 & 0.015 \\ 0.006 & 0.015 & 0.145 \end{bmatrix} \tag{6.9}$$

Disturbance Torques

The three largest contributors of disturbance torques in VLEO will be taken into account; gravity gradient torque ($\mathbf{T}_{gg}$), aerodynamic torque ($\mathbf{T}_a$), and residual magnetic field torque ($\mathbf{T}_m$). In equations (6.10) to (6.12) the equations for the disturbance torques are given (Larson and Wertz, 1999).

$$\mathbf{T}_{gg} = 3n^2 \mathbf{c}_z \times J\mathbf{c}_z \tag{6.10}$$

$$\mathbf{T}_a = \frac{1}{2}\rho C_D A \mathbf{V}^2 \left(\mathbf{u}_v \times \mathbf{s}_{cp}\right) \tag{6.11}$$

$$\mathbf{T}_m = \mathbf{M}_{res} \times \mathbf{B} \tag{6.12}$$

Where $\mathbf{c}_z$ is the z column from the rotation matrix C, $\mathbf{u}_v$ is the unit vector in velocity direction, $\mathbf{s}_{cp}$ is the vector distance from center of mass to center of pressure with $\max \mathbf{s}_{cp} = 7\text{cm}$, $\mathbf{m}_{res} = 0.002\text{A m}^2$ is the residual magnetic moment present in the spacecraft, and $\mathbf{B}$ is the geomagnetic field vector at the orbital position of the spacecraft.

Control Torque

The control torque will be provided by the magnetorquers, that have to generate a magnetic moment of $\mathbf{M}$. This will interact with the geomagnetic field, $\mathbf{B}$, to generate a control torque, τ, in equation (6.13).

$$\tau_c = \mathbf{M} \times \mathbf{B} \tag{6.13}$$

6.4. Control Algorithm

The chosen algorithm is an averaging-based feedback control law, with two cases of nonlinear quaternion feedback laws. The first one is a full-state feedback, that uses both attitude and angular velocity measurements. The second one is a passivity-based feedback that does not require angular velocity measurements (Reyhanoglu et al., 2009). Here, it will be presented in more detail and the first results will be briefly discussed. The method presented is based on the one from Reyhanoglu et al. (2009). For the initial design of the control law, some simplifications were made. The geomagnetic field will be modeled with a basic dipole model, and the disturbance torques T_d will be taken constant as $\left[0\ 10^{-7}\ 10^{-7}\right]^T$, but the gravity gradient disturbance torque will be in the dynamic equation already.

6.4.1. Control Law

The control torque is defined as in equation (6.13). **B** is the geomagnetic field in the body frame, and is defined in equation (6.14). With $\mathbf{B}_o$ being the geomagnetic field in the orbit frame (LHLV).

$$\mathbf{B} = C\mathbf{B}_o \qquad \text{with} \qquad \mathbb{B}_o = \frac{\mu_m^2}{a^6}\begin{bmatrix} \cos nt \sin i_m \\ -\cos i_m \\ 2\sin nt \sin i_m \end{bmatrix} \tag{6.14}$$

Now the magnetic moment **M** can be defined as equation (6.15) and the control torque τ for this feedback law can be defined as equation (6.16), $\tilde{\mathbf{B}}$ is the skew-symmetric matrix of **B**.

$$\mathbf{M} = \tilde{\mathbf{B}}\mathbf{u} \tag{6.15}$$

$$\tau = G(t)\,\mathbf{u} \qquad \text{with} \qquad G(t) = \tilde{\mathbf{B}}\tilde{\mathbf{B}}^T \tag{6.16}$$

Full-State Feedback

For the full-state feedback, both attitude and angular velocity measurements are used. Here **u** becomes equation (6.17).

$$\mathbf{u} = -\left[\epsilon^2 k_1 \mathbf{q}_v + \epsilon k_2 \omega_r\right] \tag{6.17}$$

Where ϵ is a sufficiently small positive parameter, and k_1 and k_2 are positive gains. Further, equation (6.18) has to hold to so there exists an $\epsilon > 0$ such that the control law achieves asymptotic attitude regulation.

$$k_2 > 1.5 J n \frac{a^6}{\mu_m^2} \tag{6.18}$$

Passivity-Based Feedback

In the passivity-based feedback only attitude measurements are used, and no angular velocity measurements are needed. Here **u** becomes equation (6.19).

$$\mathbf{u} = -\left[\epsilon^2 k_1 \mathbf{q}_v + \epsilon k_2 \left(q_4 \mathbf{y}_v - y_4 \mathbf{q}_v - \tilde{\mathbf{q}}_v \mathbf{y}_v\right)\right] \tag{6.19}$$

$$\begin{aligned} \text{with} \qquad \dot{\alpha} &= -\alpha + \mathbf{q} \qquad \alpha = \begin{bmatrix}\alpha_v^T & \alpha_4\end{bmatrix}^T \in \Re^4 \\ \mathbf{y} &= -\alpha + \mathbf{q} \qquad \mathbf{y} = \begin{bmatrix}\mathbf{y}_v^T & y_4\end{bmatrix}^T \in \Re^4 \end{aligned}$$

Where α is the filter state and **y** is the output vector, and ϵ, k_1, and k_2 are the same as in the full-state feedback.

Gain Selection

The gains k_1 and k_2 can be set the same value, so $k_1 = k_2$. In this case k_1 has to satisfy equation (6.18), as well. This causes $k_1, k_2 > 3.77 \cdot 10^5$. The parameter ϵ acts as a sort of damping coefficient, and is given a value of $\epsilon = 0.3$. For the gains, an equation is made inspired by an equation used for the gains in a PD controller. It is formulated in equation (6.20), where θ_s is the steady-state required angle, and T_d is the worst case disturbance torque. The value found is in agreement with equation (6.18).

$$k_1, k_2 = \frac{2}{\epsilon}\frac{\theta_s}{T_d} = \frac{2}{0.3}\frac{1\frac{\pi}{180}}{1.0 \cdot 10^{-7}} = 1.16 \cdot 10^6 \tag{6.20}$$

6.4.2. Initial Results

With the selected gains, both feedback laws stabilize the spacecraft within half an orbit, if only the pitch axis has to be stabilized. If any of the other axis has an deviation, it will oscillate with that deviation and only reduced very slowly. Since this control law is designed for nominal mode, so after de-tumbling and spin-up of the momentum wheel, it is assumed that there will not be any large deviations other than in the pitch axis.

To show that the system can be stabilized, a parameter $\dot{V}$ will be determined by equation (6.21) (Reyhanoglu et al., 2009). This parameter has to be smaller than or equal to zero and has to converge towards zero. In figures 6.1a and 6.1b it is shown that for the chosen gains, $\dot{V}$ converges towards zero, this means that the system can be stabilized for both feedback laws.

$$\dot{V} = -\epsilon\eta_2^T\left(k_2 + 1.5Jn\frac{R^6}{\mu_m^2}\mathbf{c}_z\mathbf{c}_x^T\right)\eta_2 \leq 0 \qquad \text{with} \qquad \eta_2 = \frac{\omega + n\mathbf{c}_y}{\epsilon} = \frac{\omega_r}{\epsilon} \tag{6.21}$$

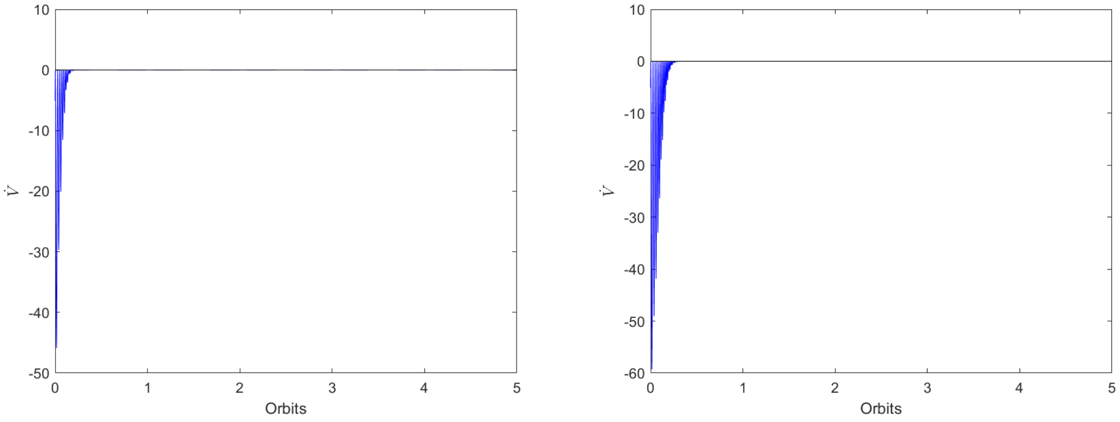

(a) $\dot{V}$ for the full-state feedback

(b) $\dot{V}$ for the passivity-based feedback

Figure 6.1: $\dot{V}$ for both feedback laws, showing that the spacecraft can be stabilized

In figures 6.2a and 6.2b the roll, pitch, and yaw angles are shown and how they behave over time from a certain initial condition. In this case, the initial condition is 1° for roll, 10° for pitch, and 1° for yaw. It can be seen that the spacecraft is stabilized within 0.2 orbit.

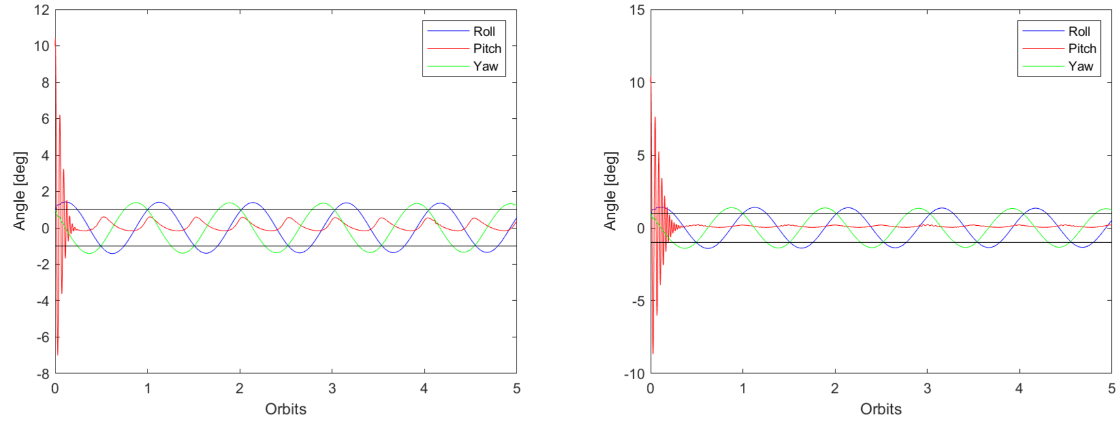

(a) Angles for the full-state feedback

(b) Angles for the passivity-based feedback

Figure 6.2: Angles (roll, pitch, and yaw) for both feedback laws. The solid black horizontal lines are the 1° marks of the requirements. Both figures are showing that the spacecraft will meet the requirements within 0.2 orbits for the pitch axis. The other two axis are not converging towards zero.

The angular velocity is shown in figures 6.3a and 6.3b, the different axis are shown in their own graph (x-axis in the top figure, z-axis in the bottom figure). The angular velocity of the pitch axis is stabilized within 0.1 orbit, the angular velocities for the other axes do not exceed the required values at all.

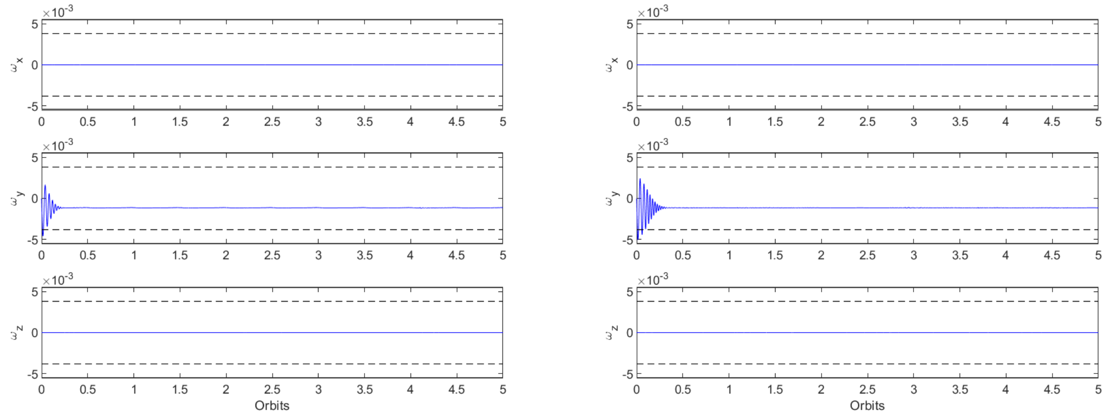

(a) Angular velocities for the full-state feedback

(b) Angular velocities for the passivity-based feedback

Figure 6.3: Angular velocities for both feedback laws. The axis are sized for the main requirement of 5.5 mrad/s, the dashed lines represent the desired value of 3.8 mrad/s. Both figures are showing that the spacecraft will meet the requirements within 0.1 orbits for all axis.

The magnetic moments needed to stabilize the spacecraft are shown in figures 6.4a and 6.4b. The maximum values do not exceed the 0.5 Am^2, for which the magnetorquers are designed. A duty cycle of 90% is used, so 9 seconds of actuation, 1 second off for magnetic field measurements.

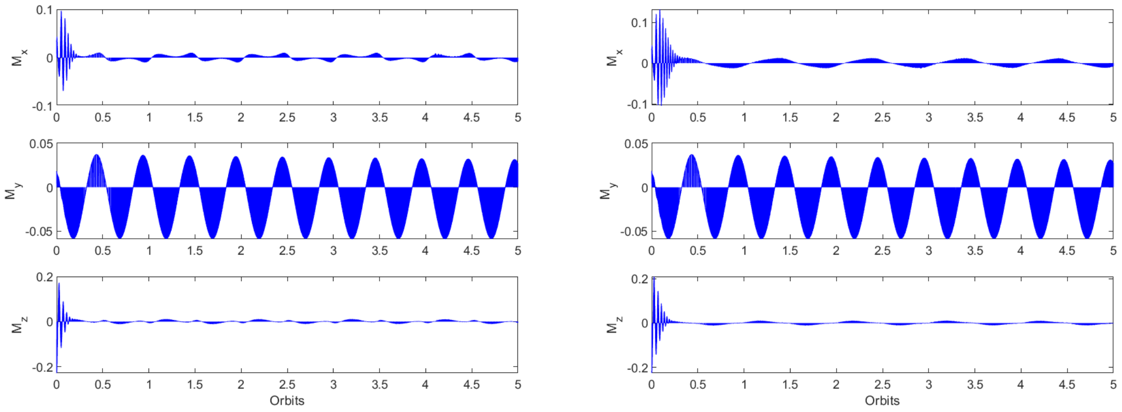

(a) Magnetic moments for the full-state feedback

(b) Magnetic moments for the passivity-based feedback

Figure 6.4: Magnetic moments for both feedback laws, showing that the spacecraft will meet the requirements of a maximum magnetic moment of 0.5 Am^2

The variations shown in figures 6.2a and 6.2b can be explained by looking at the disturbance torques. Since in this model we have a constant torque and the gravity gradient torques, only the latter one can contribute to these variation or nutations. In figures 6.5a and 6.5b, both the angles and the gravity gradient torques are shown. It can be seen that the gravity gradient torques are clearly causing the variations in the angles.

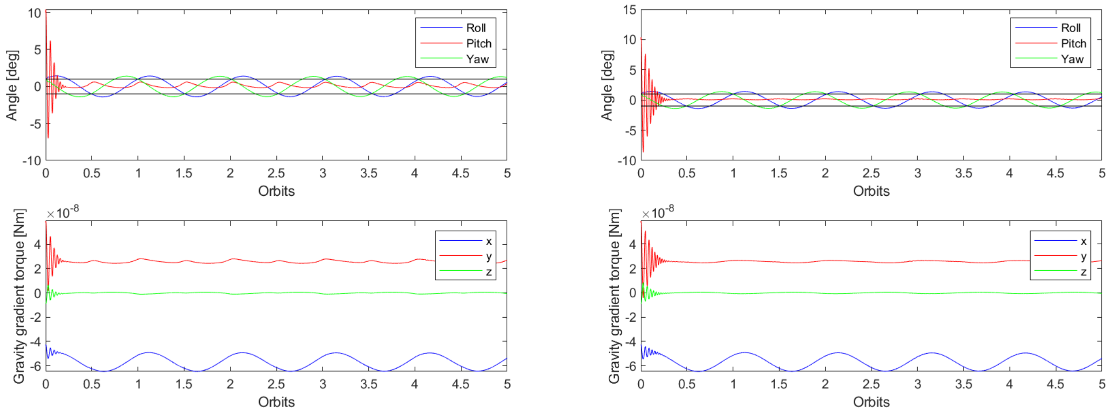

(a) Angles and gravity gradient torques for the full-state feedback

(b) Angles and gravity gradient torques for the passivity-based feedback

Figure 6.5: Angles and gravity gradient torques for both feedback laws. The top figure is the same as before, the bottom figure shows the gravity gradient torques per axis.

7

Attitude Control Loop Design

The final attitude control loop includes the control law presented earlier in section 6.4, with the orbital model, the geomagnetic field, and the disturbance torques. This final control loop is designed for the nominal mode of SHAPE. The first results after these adaptations will be shown in section 7.1 and compared to the results of the initial design in section 6.4.2. Then, in section 7.2, nutation dampers will be discussed and implemented to further damp the angular motion. Finally, in section 7.3 the control loop will be tested in end of life conditions and compared to the beginning of life results.

7.1. Adapted Attitude Control Loop

The more realistic attitude control loop for SHAPE includes the control law presented in section 6.4, with the orbital model of section 5.2, the geomagnetic field of section 5.3, and the disturbance torques as in section 6.3.2. One other change has been made: the geomagnetic field in the torque and magnetic moment calculations are not the same. The field used for the magnetic moment determination will be the measured geomagnetic field, which will be updated every ten seconds. The geomagnetic field in the torque calculation is the local field that will be there at that moment. So, equations (6.15) and (6.16) will change into equations (7.1) and (7.2), where $\tilde{\mathbf{B}}_{meas}$ is the measured geomagnetic field and $\tilde{\mathbf{B}}_{real}$ the local field at that moment.

$$\mathbf{M} = \tilde{\mathbf{B}}_{meas}\mathbf{u} \tag{7.1}$$

$$\tau = G(t)\,\mathbf{u} \qquad \text{with} \qquad G(t) = \tilde{\mathbf{B}}_{real}\tilde{\mathbf{B}}_{meas} \tag{7.2}$$

To be able to compare the results of the initial and final control loop, the same initial conditions are applied. In the following figures, the $\dot{V}$ (figures 7.1a and 7.1b), angles (figures 7.2a and 7.2b), angular velocities (figures 7.3a and 7.3b), and magnetic moments (figures 7.4a and 7.4b) are shown.

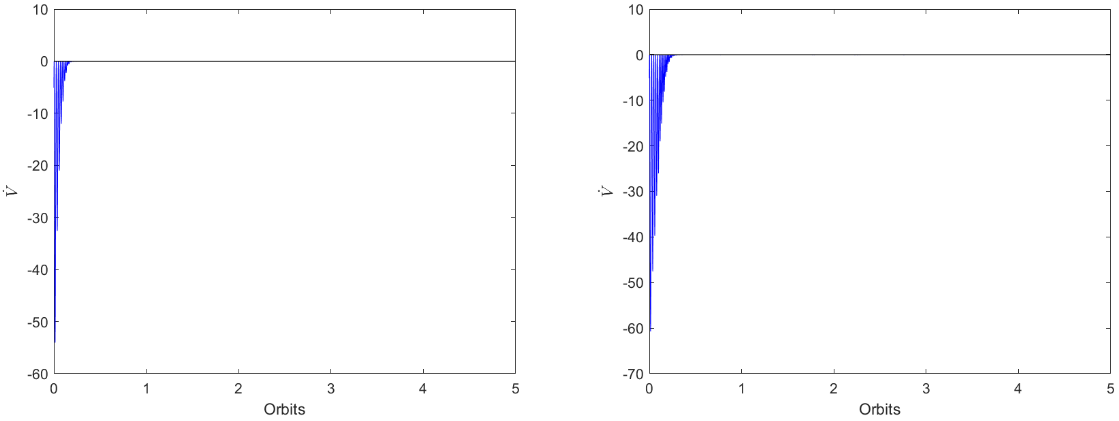

(a) $\dot{V}$ for the full-state feedback

(b) $\dot{V}$ for the passivity-based feedback

Figure 7.1: $\dot{V}$ for both feedback laws, showing that the spacecraft can be stabilized

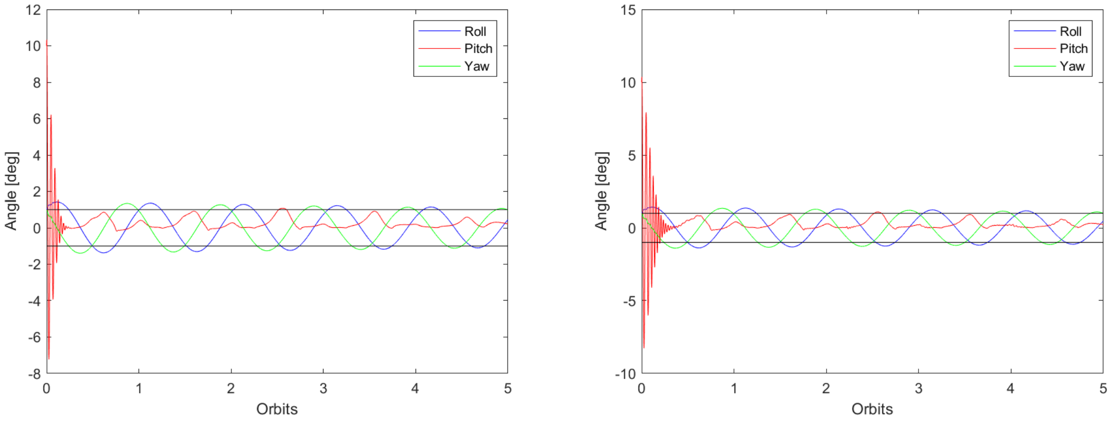

(a) Angles for the full-state feedback

(b) Angles for the passivity-based feedback

Figure 7.2: Angles (roll, pitch, and yaw) for both feedback laws, showing that the spacecraft will meet the requirements within 0.2 orbits

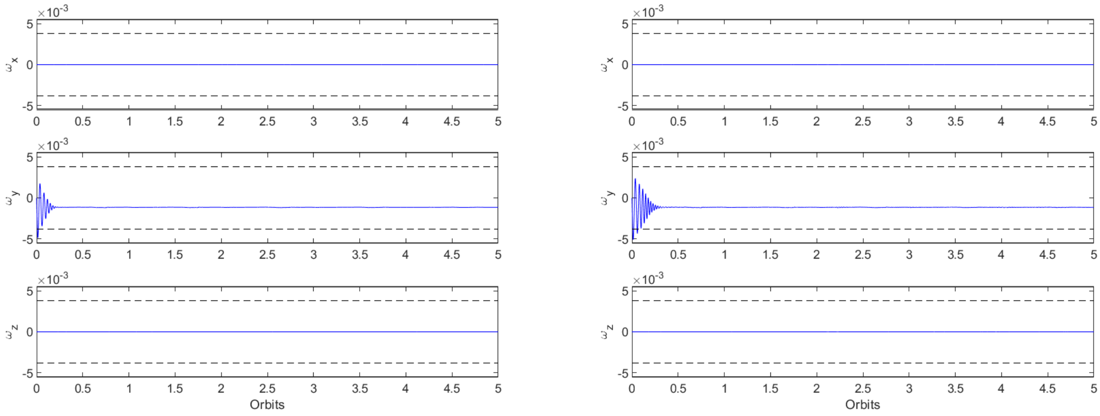

(a) Angular velocities for the full-state feedback

(b) Angular velocities for the passivity-based feedback

Figure 7.3: Angular velocities for both feedback laws, showing that the spacecraft will meet the requirements within 0.1 orbits

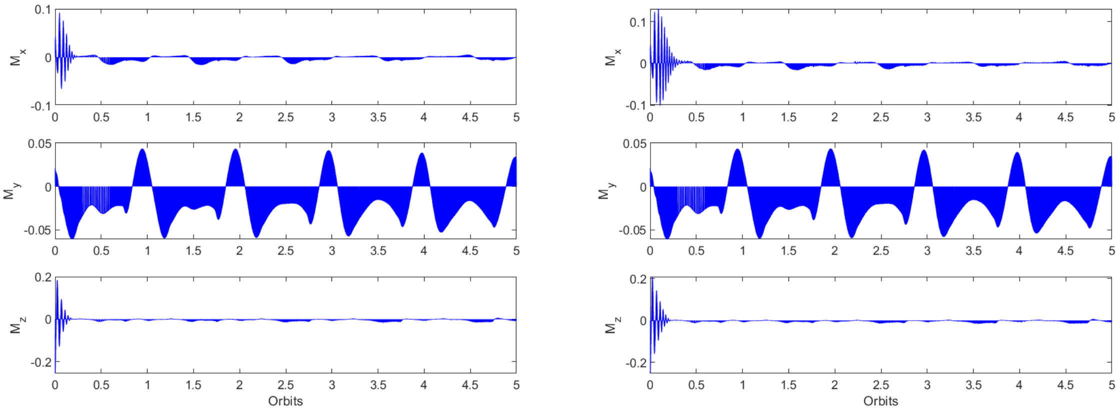

(a) Magnetic moments for the full-state feedback

(b) Magnetic moments for the passivity-based feedback

Figure 7.4: Magnetic moments for both feedback laws, showing that the spacecraft will meet the requirements of a maximum magnetic moment of 0.5 Am^2

In the figures it is shown that the spacecraft can be stabilized. The pitch axis is converged within half an orbit, just like the initial design. The other axes are stable as well, but only slowly converge towards zero or keep the same oscillation. But, if assumed that the nominal mode is entered when the roll and yaw angles are as desired, this will mean that there will be only a very small oscillation around these axis well below the 1°. For the pitch axis it can be seen that it does stay within the required 1°, but it still has quite some variations. It would be beneficial to the mission if the pitch axis can be damped further, so nutation dampers will be considered for this extra damping and will be discussed next in section 7.2.

7.2. Nutation Dampers

Nutation dampers are used to further damp the angular motion in the pitch axis. The ball-in-tube nutation damper can be modeled by a spring dashpot damper, and can be modeled into the control law with the following equations (Hughes, 2004)

$$d\dot{p} = -\bar{\omega} p + T_d \tag{7.3}$$

$$d\dot{H} = -\bar{\omega} H - \bar{V} p + \tau \tag{7.4}$$

$$d\dot{p}_n = m_d \omega^T \bar{n} (V - \bar{r_d} \omega) - c_d \dot{\xi} - k_d \xi \tag{7.5}$$

with

$$r_d = b + \xi n \tag{7.6}$$

$$p = mV - \bar{c}\omega + m_d \dot{\xi} n \tag{7.7}$$

$$H = \bar{c}V + J\omega + m_d \dot{\xi} \bar{b} n + H_s \tag{7.8}$$

$$p_n = m_d \left(n^T V - n^T \bar{b} \omega + \dot{\xi} \right) \tag{7.9}$$

$$Ha = J_w a^T \omega + H_s \tag{7.10}$$

Where $\dot{\xi}$ can be derived from the equation for p_n and is done by Ju (2017), so the result is shown here:

$$\dot{\xi} = \frac{\frac{p_n}{m_d} + n^T \bar{b} K^{-1} (H - H_a a)}{1 - n^T n \frac{m_d}{m} + n^T \bar{b} K^{-1} m_d \bar{b} n} \tag{7.11}$$

with

$$K = \frac{\bar{c}\bar{c}}{m} + J - J_w a^T a \tag{7.12}$$

Here, p is the linear momentum vector, m_d is the damper mass, n is the direction of the damper mass in the body frame, c_d is the dashpot coefficient, k_d is the spring coefficient, r_d is the distance of the damper mass to the origin of the body frame, ξ is the displacement of the damper mass in the direction of n, m is the spacecraft mass, $c = m_d \xi n$, V is the absolute velocity of the spacecraft, H_s is the angular momentum of the momentum wheel, b is the position vector of the damper in neutral position from the origin of the body frame, and a is the direction of the momentum wheel spin axis in the body frame. The values for the damper properties can be found in table 7.1.

Table 7.1: Nutation damper properties (Ju, 2017)

Parameter	Value
m_d	10 g
b	0.15 m
k_d	0.71 kg/m
c_d	0.01 kg·s/m
$\lvert\xi\rvert_{max}$	15 mm

To compare the results, the same initial conditions were taken as for the adapted control loop in section 7.1. The results for the control loop with nutation damper are shown in figures 7.5 to 7.8.

In figure 7.6a it is clearly visible that the nutation damper works, compared to figure 7.2a, for the pitch axis. For the other axis it does not seem to do anything.

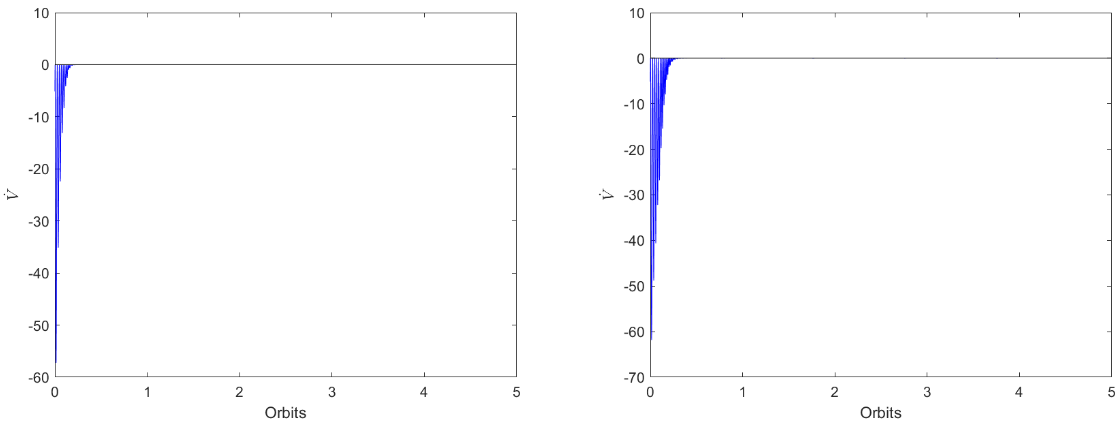

(a) $\dot{V}$ for the full-state feedback

(b) $\dot{V}$ for the passivity-based feedback

Figure 7.5: $\dot{V}$ for both feedback laws, showing that the spacecraft can be stabilized

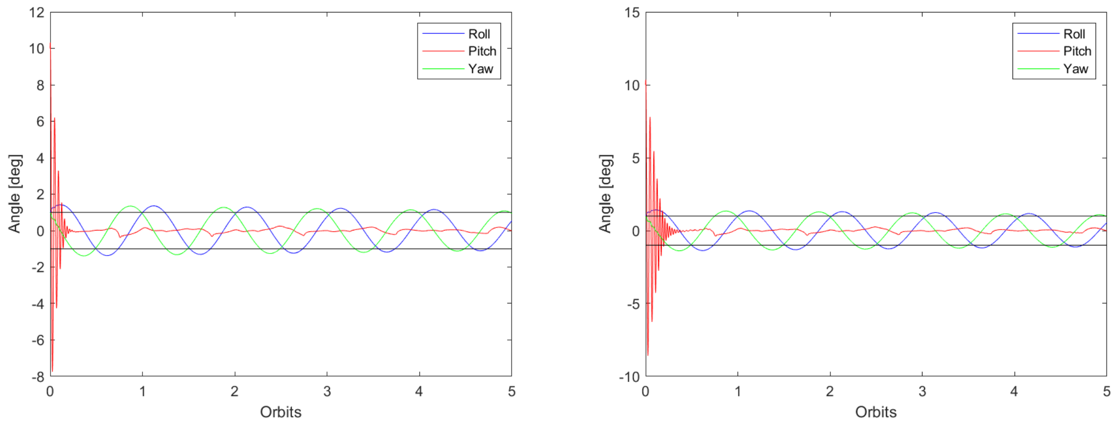

(a) Angles for the full-state feedback

(b) Angles for the passivity-based feedback

Figure 7.6: Angles (roll, pitch, and yaw) for both feedback laws, showing that the spacecraft will meet the requirements within 0.2 orbits

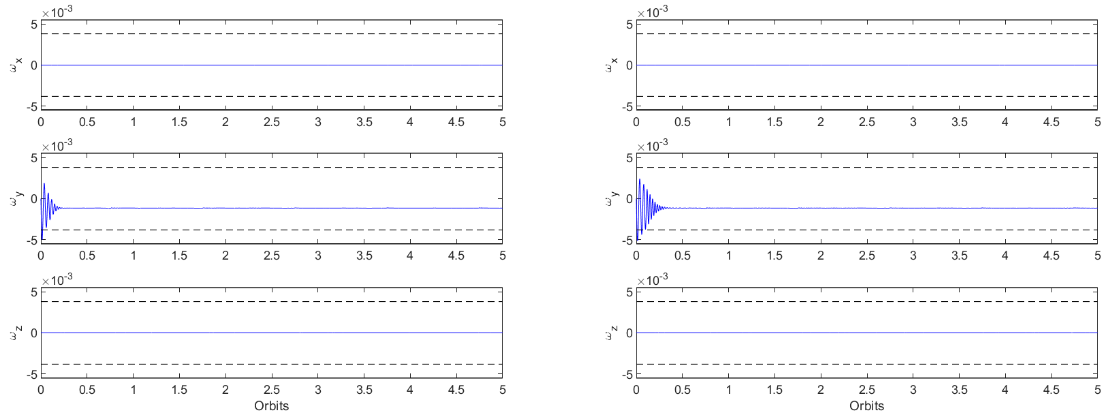

(a) Angular velocities for the full-state feedback

(b) Angular velocities for the passivity-based feedback

Figure 7.7: Angular velocities for both feedback laws, showing that the spacecraft will meet the requirements within 0.1 orbits

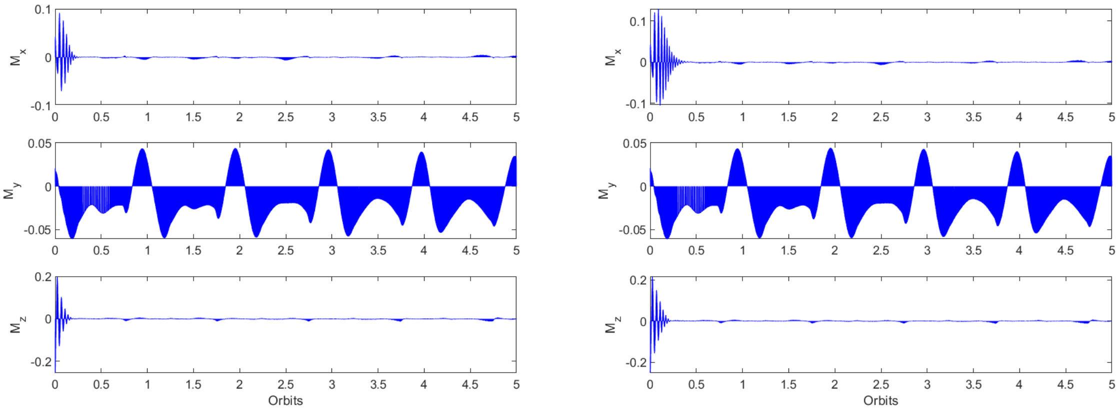

(a) Magnetic moments for the full-state feedback

(b) Magnetic moments for the passivity-based feedback

Figure 7.8: Magnetic moments for both feedback laws, showing that the spacecraft will meet the requirements of a maximum magnetic moment of 0.5 Am^2

7.3. End-of-Life Conditions

The end-of-life conditions mainly mean a much lower altitude than at the beginning of the mission. This will cause higher disturbances, so it is crucial to check if the control loop will work well under these conditions, as well.

To perform more realistic simulations the initial conditions were taken as they would be at the beginning of the nominal phase, so after de-tumbling and spinning up the momentum wheel. According to Ju (2017), it is possible to start the nominal mode with an angular deviation of about 0.02°, so this value will be used for all axis.

With these initial conditions the control loop was tested for both beginning-of-life and end-of-life conditions, so at an altitude of 380 km and 230 km, respectively, and without and with nutation damper. All results are shown below in figures 7.9 to 7.16. It is clearly visible that the control loop is not stable at the end of life without a nutation damper. With a nutation damper, the spacecraft is stable for the entire lifespan, well within the set requirements. This means it is crucial to the mission to add a nutation damper.

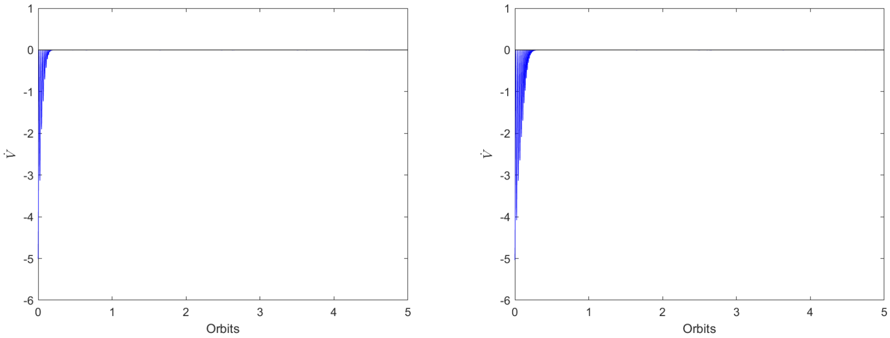

(a) $\dot{V}$ for the full-state feedback

(b) $\dot{V}$ for the passivity-based feedback

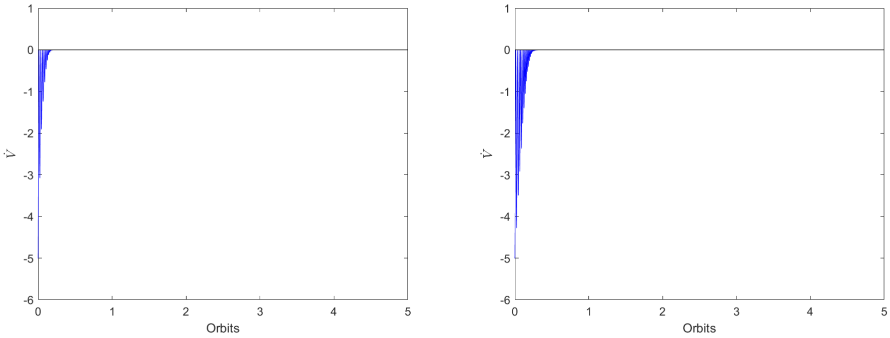

(c) $\dot{V}$ for the full-state feedback with nutation damper

(d) $\dot{V}$ for the passivity-based feedback with nutation damper

Figure 7.9: $\dot{V}$ for both feedback laws at the **beginning** of life.

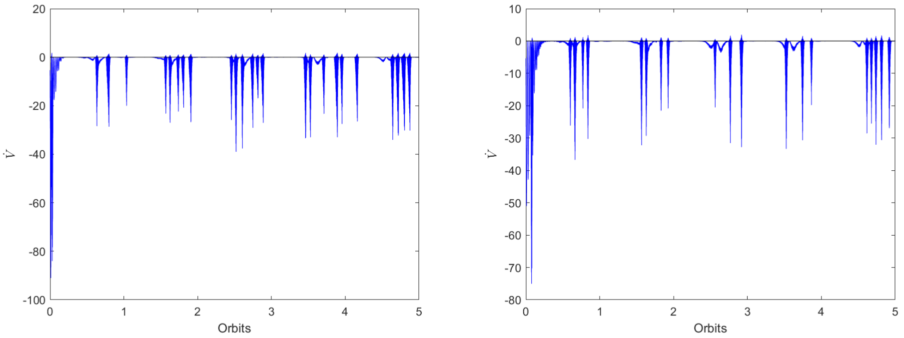

(a) $\dot{V}$ for the full-state feedback (b) $\dot{V}$ for the passivity-based feedback

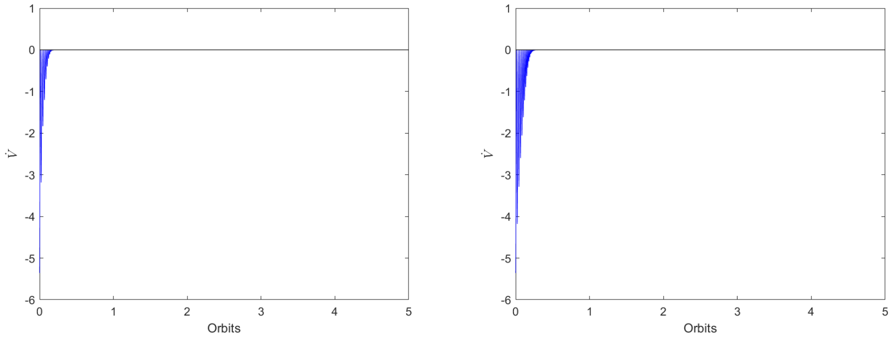

(c) $\dot{V}$ for the full-state feedback with nutation damper (d) $\dot{V}$ for the passivity-based feedback with nutation damper

Figure 7.10: $\dot{V}$ for both feedback laws at the **end** of life.

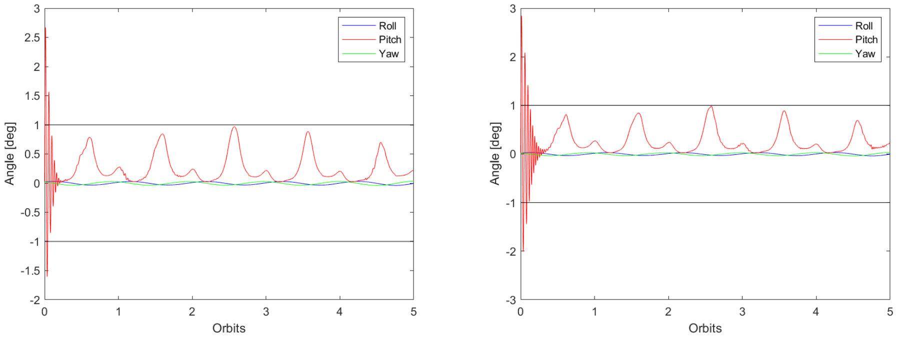

(a) Angles for the full-state feedback (b) Angles for the passivity-based feedback

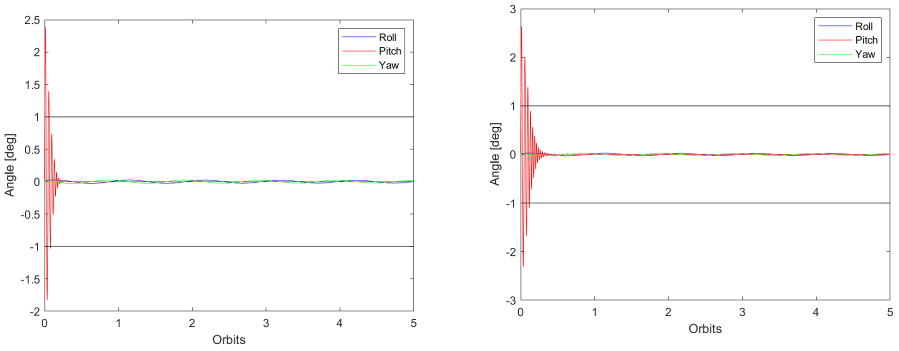

(c) Angles for the full-state feedback with nutation damper (d) Angles for the passivity-based feedback with nutation damper

Figure 7.11: Angles (roll, pitch, and yaw) for both feedback laws at the **beginning** of life.

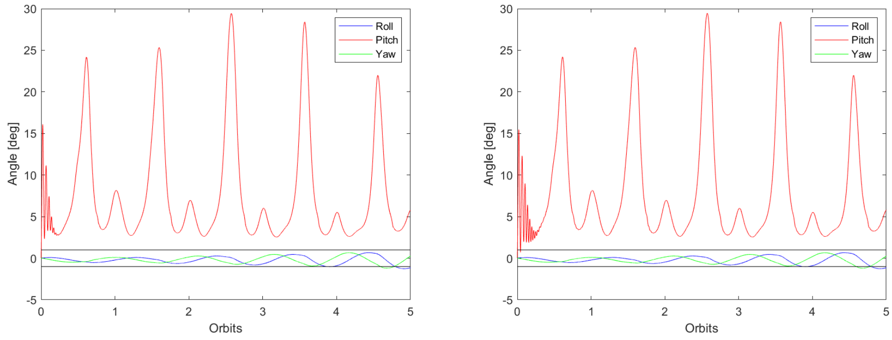

(a) Angles for the full-state feedback

(b) Angles for the passivity-based feedback

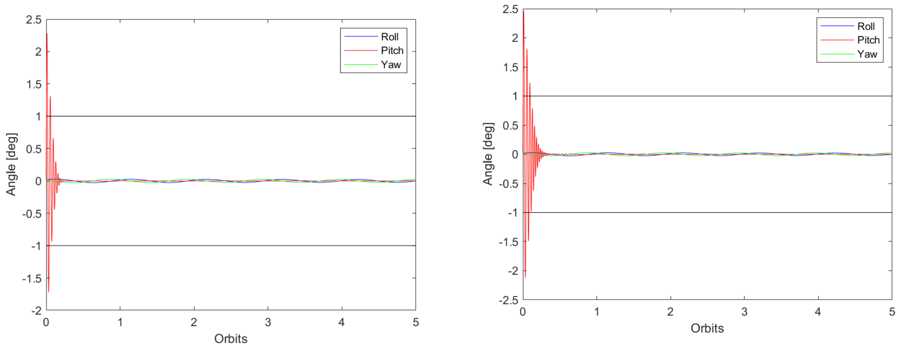

(c) Angles for the full-state feedback with nutation damper

(d) Angles for the passivity-based feedback with nutation damper

Figure 7.12: Angles (roll, pitch, and yaw) for both feedback laws at the **end** of life.

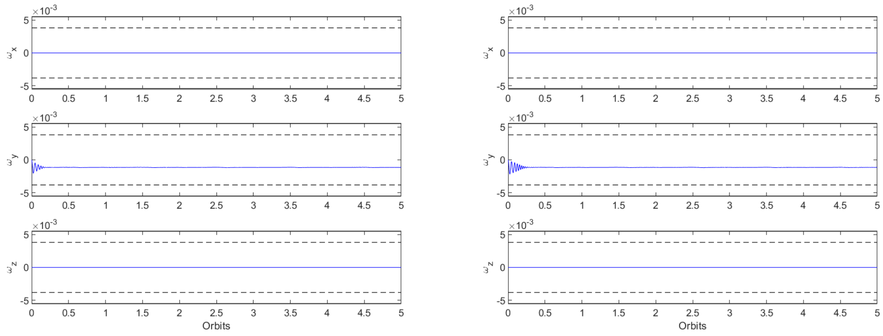

(a) Angular velocities for the full-state feedback

(b) Angular velocities for the passivity-based feedback

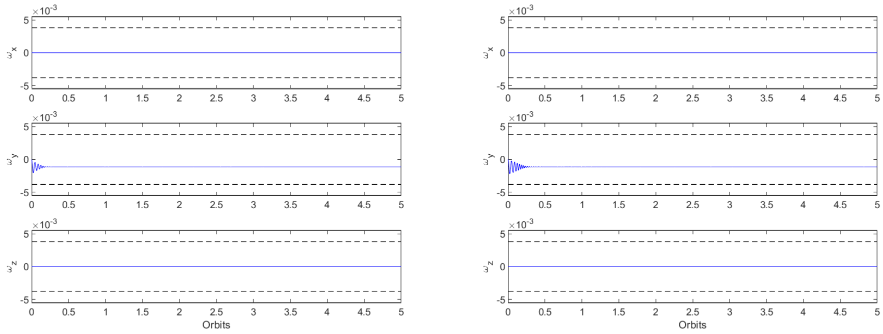

(c) Angular velocities for the full-state feedback with nutation damper

(d) Angular velocities for the passivity-based feedback with nutation damper

Figure 7.13: Angular velocities for both feedback laws at the **beginning** of life.

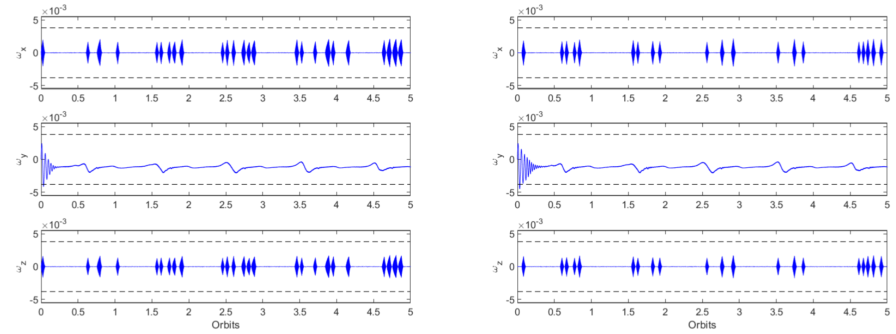

(a) Angular velocities for the full-state feedback

(b) Angular velocities for the passivity-based feedback

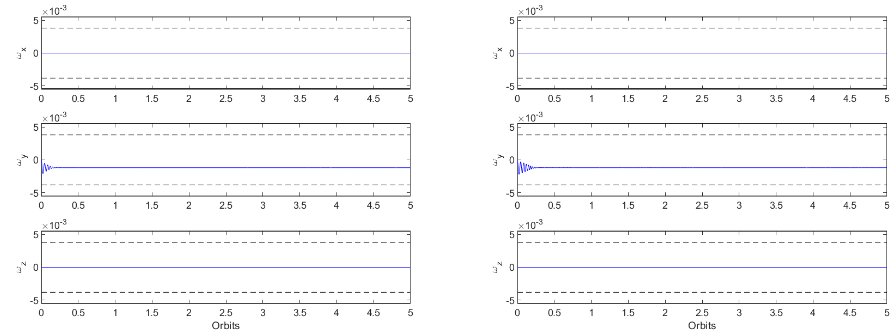

(c) Angular velocities for the full-state feedback with nutation damper

(d) Angular velocities for the passivity-based feedback with nutation damper

Figure 7.14: Angular velocities for both feedback laws at the **end** of life.

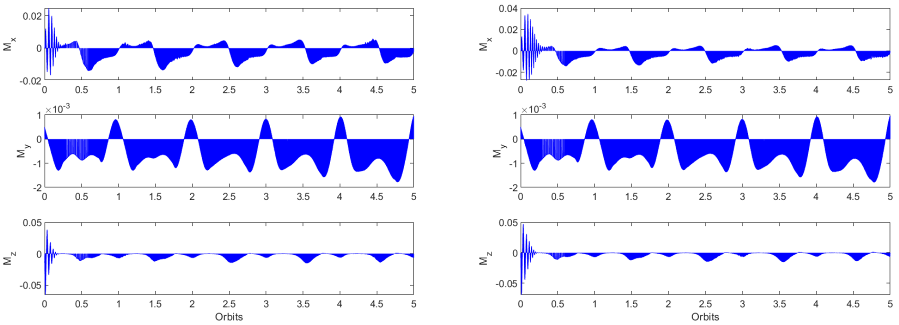

(a) Magnetic moments for the full-state feedback

(b) Magnetic moments for the passivity-based feedback

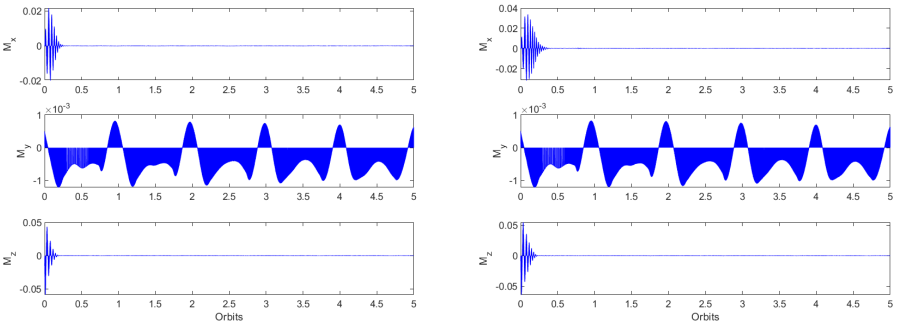

(c) Magnetic moments for the full-state feedback with nutation damper

(d) Magnetic moments for the passivity-based feedback with nutation damper

Figure 7.15: Magnetic moments for both feedback laws at the **beginning** of life.

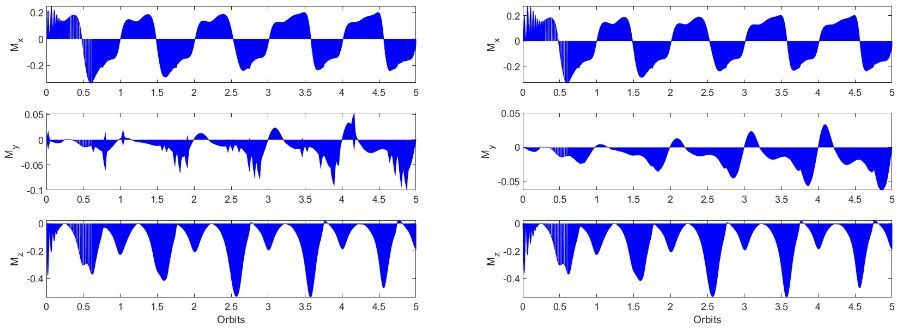

(a) Magnetic moments for the full-state feedback

(b) Magnetic moments for the passivity-based feedback

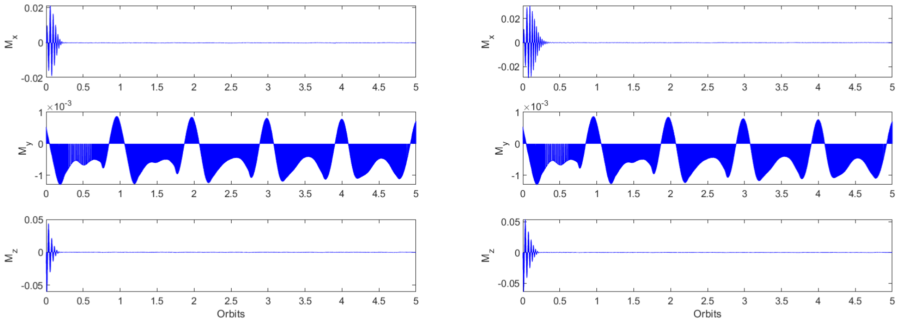

(c) Magnetic moments for the full-state feedback with nutation damper

(d) Magnetic moments for the passivity-based feedback with nutation damper

Figure 7.16: Magnetic moments for both feedback laws at the **end** of life.

7.4. Latitude Limitations

In section 5.3.3 it is concluded that higher latitudes have a lot of unpredictable disturbances in the geomagnetic field. Due to these disturbances it is recommended to not use the magnetorquers at these higher latitudes. This will have a big impact on the control loop, so simulations have to show if it is still possible to stabilize the spacecraft within an acceptable time.

The higher latitudes are from approximately 60°, so it was decided to have no actuation at latitudes lower than −60° and higher than +60°. The results for the control loop with nutation damper while having these latitude limitations are shown in figures 7.17 to 7.20 for the beginning of life. The figures show that the spacecraft can be stabilized with both the full-state and passivity-based feedback within approximately one orbit.

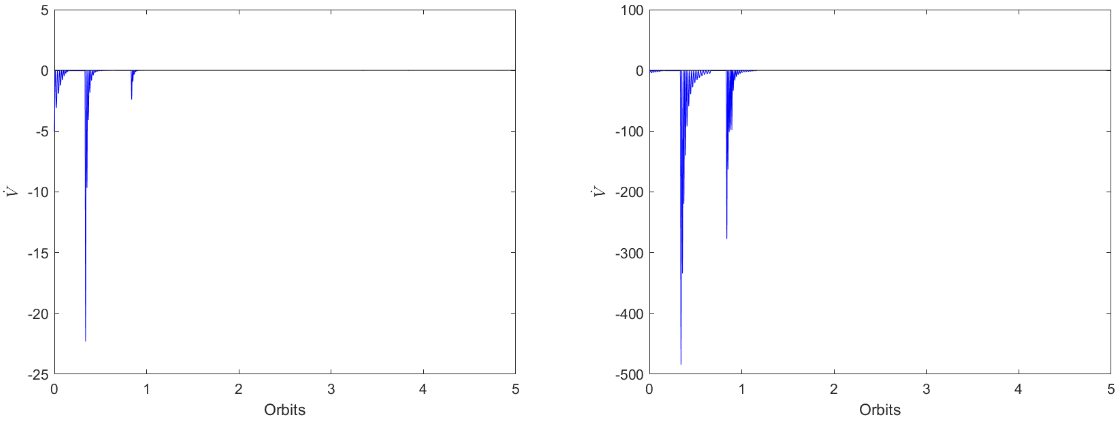

(a) $\dot{V}$ for the full-state feedback

(b) $\dot{V}$ for the passivity-based feedback

Figure 7.17: $\dot{V}$ for both feedback laws, showing that the spacecraft can be stabilized while having latitude limitations.

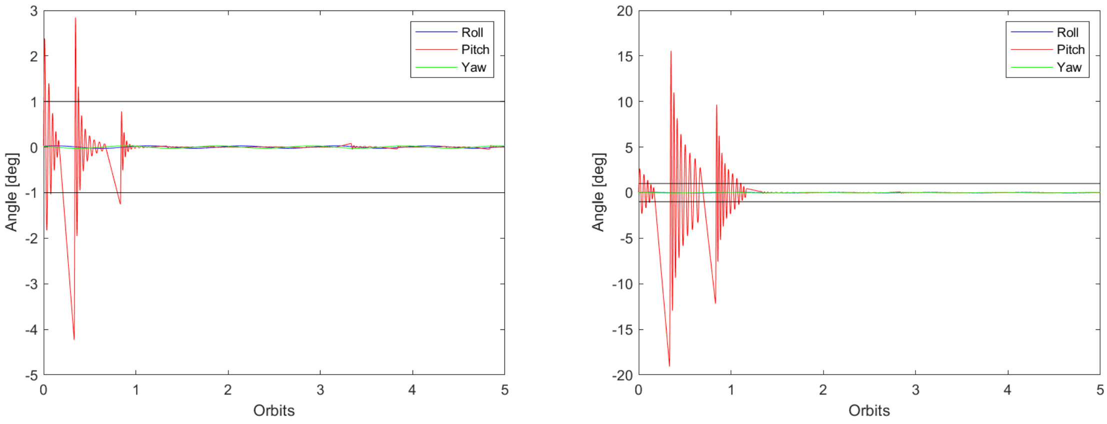

(a) Angles for the full-state feedback

(b) Angles for the passivity-based feedback

Figure 7.18: Angles (roll, pitch, and yaw) for both feedback laws, showing that the spacecraft will meet the requirements within approximately 1 orbits while having latitude limitations.

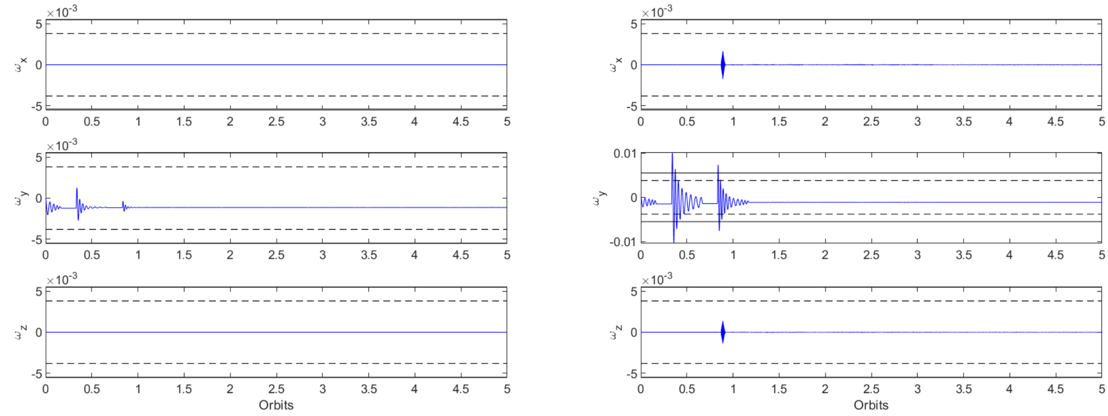

(a) Angular velocities for the full-state feedback

(b) Angular velocities for the passivity-based feedback

Figure 7.19: Angular velocities for both feedback laws, showing that the spacecraft will stay within the requirements for the full-state feedback, and for the passivity-based feedback it meets the requirements within 1 orbit while having latitude limitations.

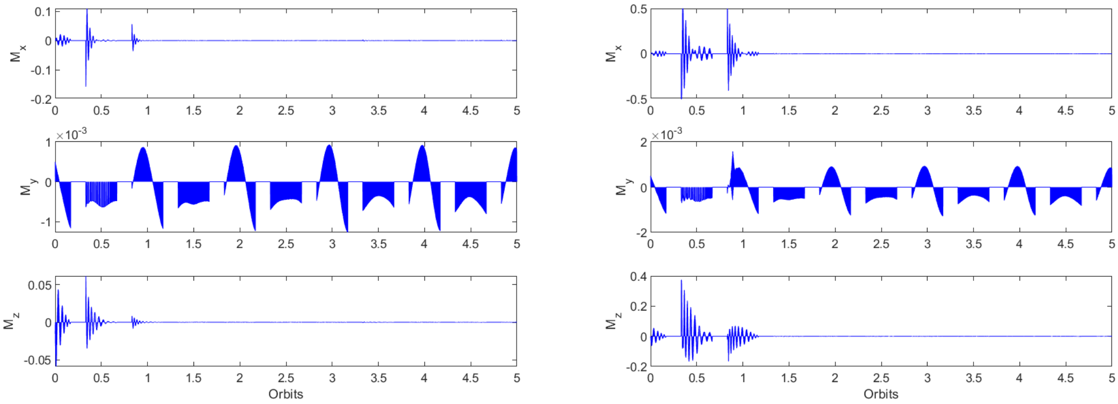

(a) Magnetic moments for the full-state feedback

(b) Magnetic moments for the passivity-based feedback

Figure 7.20: Magnetic moments for both feedback laws, showing that the spacecraft will meet the requirements of a maximum magnetic moment of 0.5 Am^2 while having latitude limitations.

For the end of life, the results from limiting the active latitudes are shown in figures 7.21 to 7.24. In these figures it is shown that the passivity-based feedback stabilizes very slowly and needs 5 orbits to come within requirements. The full-state feedback stabilizes within approximately half an orbit.

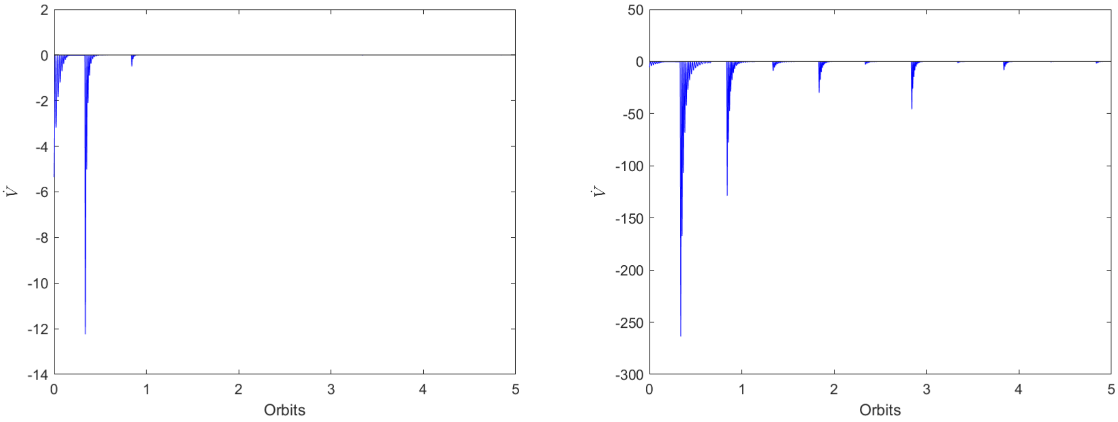

(a) $\dot{V}$ for the full-state feedback

(b) $\dot{V}$ for the passivity-based feedback

Figure 7.21: $\dot{V}$ for both feedback laws, showing that the spacecraft can be stabilized while having latitude limitations at the end of life.

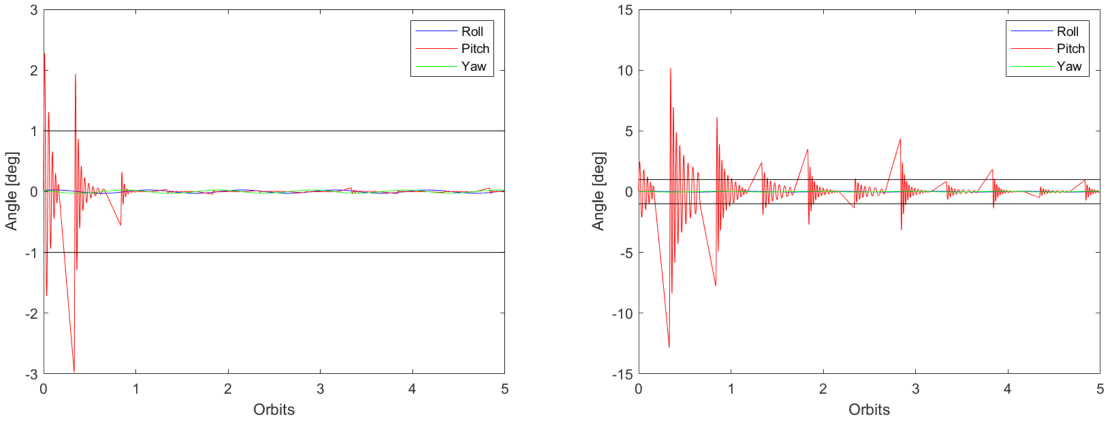

(a) Angles for the full-state feedback

(b) Angles for the passivity-based feedback

Figure 7.22: Angles (roll, pitch, and yaw) for both feedback laws, showing that the spacecraft will meet the requirements within approximately half an orbit for the full-state feedback while having latitude limitations at the end of life. The passivity-based feedback comes within requirements after 5 orbits while having latitude limitations at the end of life.

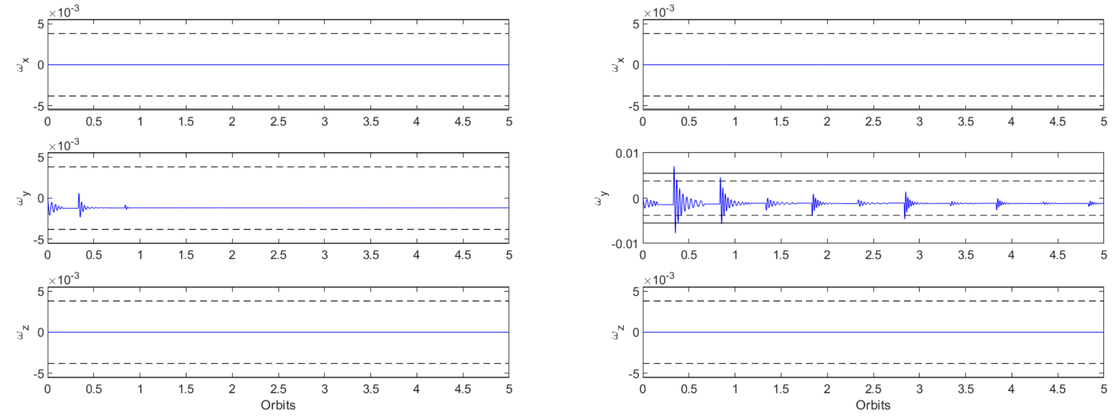

(a) Angular velocities for the full-state feedback

(b) Angular velocities for the passivity-based feedback

Figure 7.23: Angular velocities for both feedback laws, showing that the spacecraft will stay within the requirements for the full-state feedback, and for the passivity-based feedback it meets the requirements within 1 orbit while having latitude limitations at the end of life.

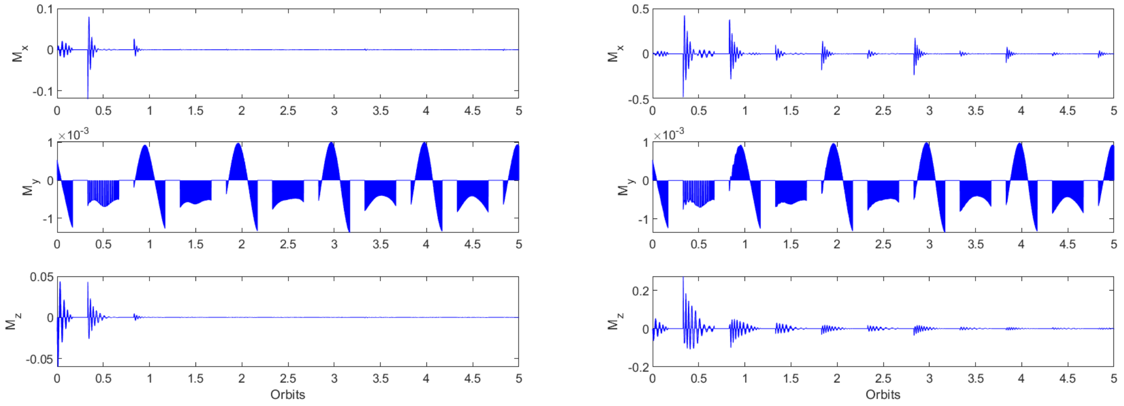

(a) Magnetic moments for the full-state feedback

(b) Magnetic moments for the passivity-based feedback

Figure 7.24: Magnetic moments for both feedback laws, showing that the spacecraft will meet the requirements of a maximum magnetic moment of 0.5 Am^2 while having latitude limitations at the end of life.

7.5. Uncertainty Budget for the Magnetic Control Loop

Within the control of the spacecraft some factors will add uncertainties to the output. In this case, the largest uncertainties come from the geomagnetic field and the uncertainties in the magnetorquers. To see how the the control loop output will react on a constant lower or higher geomagnetic field, and to a constant lower or higher output of the magnetorquers, a small analysis is done.

The analysis is done for both full-state feedback and passivity-based feedback, both with a nutation damper while having latitude limitations at the beginning of life. In figure 7.25 the results for the attitude angles is shown for a variation of 10 nT in geomagnetic field, and in figure 7.26 for a variation of 10% in magnetic moment that will be generated by the magnetorquers for the full-state feedback. In figure 7.27 the results for the passivity-based feedback is shown. As can be seen in the figures, the results for the full-state feedback will not deviate far from the original and still stabilize the spacecraft well within the requirements. For the passivity-based, the uncertainties become larger over time and the spacecraft cannot be called stable after 5 orbits. With these results, the recommended control loop will have the full-state feedback.

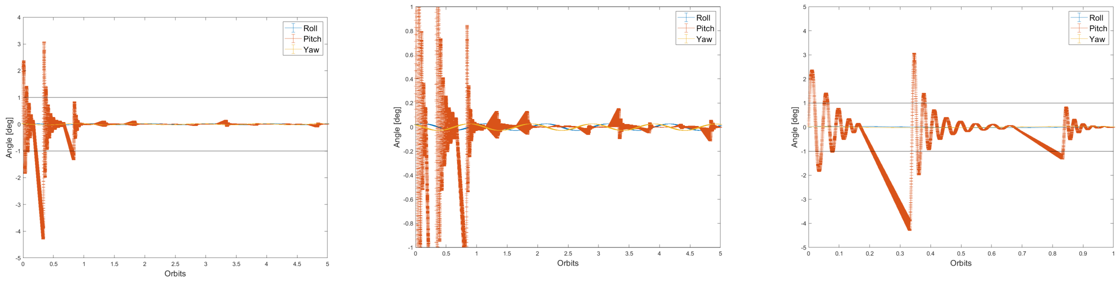

(a) Attitude angles for full-state feedback

(b) Attitude angles for full-state feedback, zoomed in on y-axis

(c) Attitude angles for full-state feedback, zoomed in on x-axis

Figure 7.25: Attitude angles for full-state feedback with uncertainties for a variation of 10 nT in the geomagnetic field.

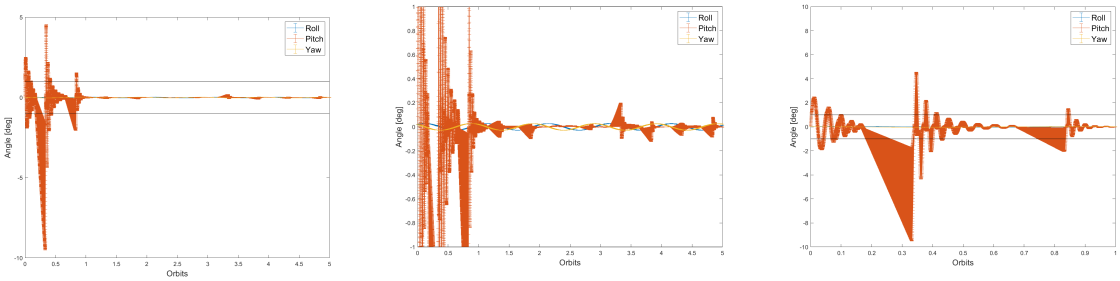

(a) Attitude angles for full-state feedback

(b) Attitude angles for full-state feedback, zoomed in on y-axis

(c) Attitude angles for full-state feedback, zoomed in on x-axis

Figure 7.26: Attitude angles for full-state feedback with uncertainties for a variation of 10% in the magnetic moment generated by the magnetorquers.

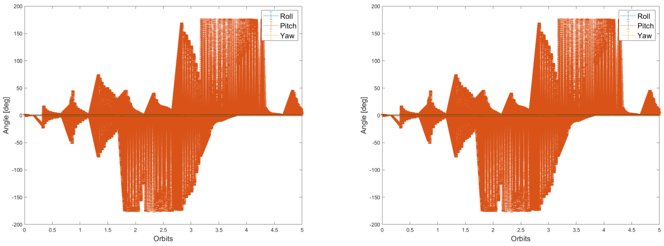

(a) Attitude angles for passivity-based feedback with uncertainties for a variation of 10 nT in the geomagnetic field.

(b) Attitude angles for passivity-based feedback with uncertainties for a variation of 10% in the magnetic moment.

Figure 7.27: Attitude angles for passivity-based feedback with the different uncertainties.

8

Conclusions and Recommendations

In this chapter, the conclusions and recommendation will be presented. In section 8.1, the conclusions will be given and the research questions will be answered. Then, in section 8.2, some recommendations will be given.

8.1. Conclusions

In the beginning of this report (chapter 2) the research objective and question for this thesis were formed and requirements were given. Here, it will be concluded if the research objective and requirements have been met, and the answer on the research question will be given.

The research objective was formulated as follows:

To come to a feasible magnetorquer control system for SHAPE, by designing a magnetorquer with a dipole moment of at least 0.5 Am^2 and an attitude control loop that achieves a pointing accuracy of at least 1° ***and attitude stability of 5.5 mrad/s or better.***

This objective has been met, since a magnetorquer with a dipole moment of at least 0.5 Am^2 has been designed and an attitude control loop has been developed that has a pointing accuracy better than 1° and attitude stability better than 5.5 mrad/s.

The final magnetorquer is designed to generate the peak dipole moment of 0.85 Am^2 without saturating the magnetic material. The recommended magnetorquer will contain 4-79 Mo-Permalloy as core material. It has a length of 14.2 mm and diameter of 12.9 mm, and a mass of 18.1 g.

The requirements given in table 2.1 for the attitude system requirements are met. The system has a better pointing accuracy and attitude stability and the total maximum mass is 54.3 g for three magnetorquers. The magnetorquer requirements from table 2.2 are met or need some further research. The magnetorquer is able to provide a nominal dipole moment of at least 0.5 Am^2 and a peak dipole moment of 0.85 Am^2. The resolution is not considered in this thesis, so this has to be resolved with some further research. The residual magnetic moment lower than 2 mAm^2 is not possible without actively bringing it down. If the magnetorquer is used on maximum strength the hysteresis of any of the materials will cause the residual moment to be higher than this requirement. Further research in de-magnetization has to show if it is possible to reduce the residual moment within the requirements.

The main research question was formulated as follows:

Is it feasible to design a magnetorquer control system for SHAPE?

The answer on this question is: yes. It is feasible to design a magetorquer control system for SHAPE. There was chosen for a nonlinear quaternion feedback law, with two cases the full-state feedback and the passivity-based feedback. They both use attitude measurements, but the full-state feedback also needs angular velocity measurements. The full-state feedback is recommended, because it stabilizes the spacecraft faster in any situation and deals better with uncertainties. The simulations show that SHAPE can stabilize well within the requirements with only magnetorquers as active actuators next to the momentum wheel with the full-state feedback control loop. This configuration will only work when a nutation damper and an angular rate sensor are added to the attitude system.

8.2. Recommendations

There are some recommendations for further research on the topic. First, some recommendations are done on the magnetorquer, then some on the control loop.

8.2.1. Magnetorquer Recommendations

For the magnetorquer, it is necessary to research the de-magnetization process. This is needed for the requirement on the residual dipole moment. It has to be researched whether the material itself de-magnetizes fast by itself, or that an active de-magnetization is required to reduce the residual moment to within the requirements.

The minimum resolution of the magnetorquer has to be considered in further research, since this is important for the control loop. The more accurate the magnetorquer can be controlled, the more accurate the spacecraft attitude can be control.

The power calculation do not seem to be right. Available magnetorquers with the same dipole moment have a power consumption a lot higher than the results presented here. Thus, the power equations and calculations have to be revised to come to a reasonable end design of the magnetorquers.

8.2.2. Control Loop Recommendations

The resolution of the magnetorquer, as mentioned before in the magnetorquer recommendations, is of importance for the control loop. With further research it can be found what the minimum resolution of the magnetorquer has to be for the control loop to still be able to function well and within the requirements.

The control loop as designed in this thesis does not explicitly use any sensors and did not take into account noise from such sensors. It is recommended to include sensors in the loop, with their noises, to see if the performances will stay within the requirements. The following sensors are needed: magnetometers, attitude sensors, and an angular rate sensor.

The momentum wheel will be spinning in magnetic bearings, these can have an effect on the control and the geomagnetic field measurements. This effect should be researched such that it can be taken into account within the control loop.

To be able to use the control loop on the spacecraft, the control loop has to be evaluated on how computational expensive it is and if it is possible to write the software for it such that it can operate on the spacecraft. This is work for someone with more knowledge of software.

Bibliography

Akasofu, S.-I. (1968), *Polar and Magnetospheric Substroms*, D. Reidel Publishing Company.

Brown, G. V. and Flax, L. (1964), 'Superposition of semi-infinite ssolenoid for calculating magnetic fields of thick solenoids', *Journal for Applied Physics* **35**(6), 1764–1767.

ElectricalEngineering123 (2016), 'Explanation of hysteresis loss & eddy current losses in transformers'. Visited on August 24, 2017.
`http://www.electricalengineering123.com/explanation-of-hysteresis-loss-eddy-current-losses-in-transf`

Elektrisola (2015), 'Technical data for enamelled copper wire, based on iec 60317'. Downloaded on January 25, 2018.
`http://www.elektrisola.com/fileadmin/webdata/english/Downloads/ELEKTRISOLA_EnCuWire_IEC_Datasheet_eng.pdf`

for Environmental Information, N. C. (n.d.). Visited on November 20, 2018.

Hughes, P. C. (2004), *Spacecraft Attitude Dynamics*.

Ju, D. (2017), Attitude control subsystem design of the stable and highly accurate pointing earth-imager, Master's thesis, Delft University of Technology.

Kuiper, J. and Dolkens, D. (2016), 'Advanced earth observation systems with high spatial resolution', *The 4S Symposium* .

Larson, W. J. and Wertz, J. R., eds (1999), *Space Mission Analysis and Design*, Kluwer Academic Publishers.

Lovera, M. and Astolfi, A. (2004), 'Spacecraft attitude control using magnetic actuators', *Automatica* **40**, 1405–1414.

Lovera, M., Marchi, E. D. and Bittanti, S. (2002), 'Periodic attitude control techniques for small satellites with magnetic actuators', *IEEE Transactions on Control Systems Technology* **10**(1), 90–95.

Luo, W. and Zhou, B. (2017), 'Magnetic attitude control of bias momentum spacecraft by bounded linear feedback', *Aerospace Science and Technology* **70**, 419–427.

McLyman, C. W. T. (2004), *Transormer and Inductor Design Handbook*, third edn, Marcel Dekker, Inc.

Milovanovic, A. M. and Koprivica, B. M. (2015), 'Mathematical model of major hysteresis loop and transient magnetizations', *Electromagnetics* **35**, 155–166.

Miranda, F. (2012), 'Guidance stabilization of satellites using the geomagnetic field', *International Journal of Aerospace Engineering* .

Montenbruck, O. and Gill, E. (2001), *Satellite Orbits - Models, Methods, and Applications*, Springer.

Montgomery, D. B. (1969), *Solenoid Magnet Design*, WILEY-INTERSCIENCE. SBN 471 61420 3.

MTQ400 (2018).
`http://hyperiontechnologies.nl/products/mtq400/`

NOAA (2010), 'The international geomagnetic reference field: A "health" warning'. Visited on July 26, 2016.
`http://www.ngdc.noaa.gov/IAGA/vmod/igrfhw.html`

Parolis, M. D. and Pinter-Krainer, W. (1996), 'Current and future techniques for spacecraft thermal control 1. design drivers and current technologies', *ESA Bulletin* **87**(87).
`http://www.esa.int/esapub/bulletin/bullet87/paroli87.htm`

Permalloy materials (YFN-45) (2007).
`http://www.metanix.co.jp/metanix/english/product/permally/index.html`

Picone, J., Hedin, A., Drob, D. and Aikin, A. (2002), 'Nrlmsise-00 emperical model of the atmosphere: Statistical comparisons and scientific issues', *Journal of Geophysical research* **107**(A12).

Psiaki, M. L. (2001), 'Magnetic torquer attitude control via asymptotic periodic linear quadratic regulation', *Journal of Guidance, Control, and Dynamics* **24**(2), 386–394.

Pulecchi, T., Lovera, M. and Varga, A. (2010), 'Optimal discrete-time design of three-axis magnetic attitude control laws', *IEEE Transactions on Control Systems Technology* **18**(3), 714–722.

Reyhanoglu, M., Ton, C. and Drakunov, S. (2009), 'Attitude stabilization of a nadir-pointing small satellite using only magnetic actuators', *IFAC Proceedings Volumes* **42**(19), 292–297. 2nd IFAC Conference on Intelligent Control Systems and Signal Processing.
`http://www.sciencedirect.com/science/article/pii/S1474667015308491`

Silani, E. and Lovera, M. (2005), 'Magnetic spacecraft attitude control: a survey and some new results', *Control Engineering Practice* **13**(3), 357–371.

Sugimura, N., Kuwahara, T. and Yoshida, K. (2016), Attitude determination and control system for nadir pointing using magnetorquer and magnetometer, *in* '2016 IEEE Aerospace Conference'.

Thébault, E., Finlay, C. C., Beggan, C. D., Alken, P., Aubert, J., Barrois, O., Bertrand, F., Bondar, T., Boness, A., Brocco, L., Canet, E., Chambodut, A., Chulliat, A., Coïsson, P., Civet, F., Du, A., Fournier, A., Fratter, I., Gillet, N., Hamilton, B., Hamoudi, M., Hulot, G., Jager, T., Korte, M., Kuang, W., Lalanne, X., Langlais, B., Léger, J.-M., Lesur, V., Lowes, F. J., Macmillan, S., Mandea, M., Manoj, C., Maus, S., Olsen, N., Petrov, V., Ridley, V., Rother, M., Sabaka, T. J., Saturnino, D., Schachtschneider, R., Sirol, O., Tangborn, A., Thomson, A., Tøffner-Clausen, L., Vigneron, P., Wardinski, I. and Zvereva, T. (2015), 'International geomagnetic reference field: the 12th generation', *Earth, Planets and Space* **67**(1), 79.
`https://doi.org/10.1186/s40623-015-0228-9`

Torczynski, D. M., Amini, R. and Massioni, P. (2010), Magnetorquer based attitude control for a nonosatellite testplatform, *in* 'AIAA Infotech @ Aerospace 2010'.

Wang, P. and Shtessel, Y. B. (1998), 'Satellite attitude control using only magnetorquers', *Proceedings of the American Control Conference* pp. 222–226.

Wertz, J. (1978), *Spacecraft attitude determination and control*, D. Reidel Publishing Company.

Wiśniewski, R. and Stoustrup, J. (2001), 'Periodic h2 synthesis for spacecraft attitude determination and control with a vector magnetometer and magnetorquers', *IFAC Proceedings Volumes* **34**(12), 119 – 124. IFAC Workshop on Periodic Control Systems 2001, Cernobbio-Como, Italy, 27-28 August 2001.

Wiśniewski, R. and Stoustrup, J. (2004), 'Periodic h2 synthesis for spacecraft attitude control with magnetorquers', *Jounal of Guidance, Control, and Dynamics* **27**(5), 874–881.

Wisniewski, R. and Blanke, M. (1996), 'Three-axis satellite attitude contol based on magnetic torquing', *13th IFAC World Congress* pp. 1–36.

Xia, X., Wu, S., Sun, G., Wang, T., Wu, Z., Bai, Y., Chen, W. and Mu, Z. (2016), Magnetic-based attitude control scheme for cubesat, *in* 'Proceedings of 2016 IEEE Chinese Guidance, Navigation and Control Conference', pp. 133–139.